Noise Attenuation and Energy Harvesting Using Helmholtz Resonator Connected to Rectangular Cavity

by

Farbod Ghanouni

A thesis presented to Lakehead University

in fulfilment of the

thesis requirement for the degree of

Master of Applied Science

In

Mechanical and Mechatronics Engineering

Thunder Bay, Ontario, Canada, 2025

I hereby declare that I am the sole author of this thesis.

I authorize Lakehead University to lend this thesis to other institutions or individuals for the purpose of scholarly research.

I further authorize Lakehead University to reproduce this thesis by photocopying or by other means, in total or in part, at the request of other institutions or individuals for the purpose of scholarly research.

Lakehead University requires the signatures of all persons using or photocopying this thesis.

Please sign below and give address and date.

Abstract

This thesis investigates the dual functionality of a Helmholtz Resonator (HR) coupled with a rectangular cavity for noise attenuation and small-scale energy harvesting. The study explores the integration of a piezoelectric energy harvester within the HR system, leveraging its resonant behavior to convert acoustical energy into electrical power. The research employs both experimental measurements and numerical simulations using ANSYS® to analyze the acoustic response of the HR and cavity under various excitations. The experimental results validate the numerical models, demonstrating the system's capability to attenuate low-frequency noise while simultaneously generating electrical energy. Optimization techniques are explored to enhance energy harvesting efficiency, considering geometric and material variations. The findings contribute to the development of multifunctional acoustic solutions for potential architectural applications and energy-efficient systems.

Acknowledgements

I am deeply grateful to Dr. K. Liu for laying the foundation of this research, guiding the literature review.

I also extend my sincere appreciation to my thesis supervisor Dr. M. Liu, whose unwavering support, expertise, and guidance were crucial in the final stages of my research. Her encouragement and rigorous reviews enabled me to complete this thesis and my master's program at Lakehead University.

To Mohammad Reza and Azam

I dedicate this thesis to my parents, whose unwavering support made it possible for me to pursue my master's program at Lakehead University. Their encouragement, sacrifices, and belief in me have been the foundation of my academic journey. At every step of the way, they provided the support I needed to continue my education, and for that, I am forever grateful.

Contents

List of Figures

List of Tables

List of Equations

Chapter 1 - Introduction

In Chapter 1, the motivation behind the research is outlined. The principal focus of this research includes the investigation of the potential for noise attenuation and small-scale acoustical energy harvesting using piezoelectric harvesters from acoustical energy within a rectangular cuboid enclosure (commonly referred to as rectangular cavity). A brief introduction to the working principles and common uses of Helmholtz resonators (HRs), which serve as the primary mechanism for noise attenuation and acoustical energy harvesting is also provided. A thorough review of recent literature employing similar approaches to the proposed system is presented, comparing systems that utilize the same subsystems: a HR, a rectangular enclosure, and a cantilever piezoelectric harvesting subsystem responsible for small-scale energy harvesting. An outline of the thesis structure concludes this chapter.

1.1 Motivation for Research

Harnessing energy from the environment has been a topic of research and development for many years. For centuries, scientists and enthusiasts have explored methods to leverage the energy available in our surroundings. Recent developments have motivated scientists and researchers to focus not only on intensive energy resources such as internal combustion engines, electric power, and nuclear energy but also on small-scale energy resources [1]. The concept of small-scale energy harvesting aligns with the trend of technological devices becoming smaller, while the demand for environmentally harvested energy increases. Piezoelectric Energy Harvesters (PEHs) provide an option for harnessing small-scale energy from

the environment [2-5]. PEHs offer the advantages of miniature energy systems, such as environmental friendliness, sustainability, portability, and flexibility, which traditional battery-based systems fail to provide [5,6]. These miniature energy harvesters are predominantly designed to take advantage of available mechanical vibration energy and acoustical energy. PEH systems facilitate the harnessing of energy from these two primary sources via an energy conversion mechanism and may include an energy storage component for the harvested energy [7-11]. However, the above-mentioned energy sources may also become a source of annoyance and disturbance. For example, in a recent study, a group of musicians commented on their perception of low-frequency resonance within a small room, and it was subsequently found that the presence of localized low frequencies negatively affected the overall perceived sound quality, including loudness and clarity [12]. The amplification of low-frequency noise also negatively affected humans working within a small room, such as a studio, as the low-frequency noise is associated with annoyance and impedes work requiring deep focus [13]. Therefore, PEHs that harvest acoustical energy while reducing noise are more desirable compared to those that only harvest acoustical energy. To fulfill this purpose, a PEH device which attenuates unwanted low-frequency tones within a small enclosure while harvesting acoustical energy is proposed.

1.2 Motivation for Research

Helmholtz resonators (HRs), as shown in Figure 1.1, consist of a hollow, air-filled cavity, typically of spherical or cylindrical shape, connected to a narrow tube commonly referred to as the neck [14].

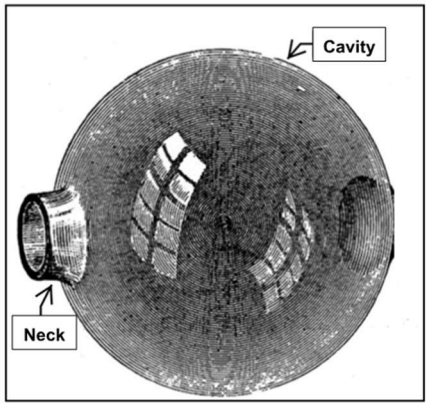

Figure 1.1. A schematic showing a classical HR [H. von Helmholtz. On the sensations of tone as a physiological basis for the theory of music. New York: Cambridge University Press; 2011].

The primary utility of HRs is in acoustical wave manipulation [15]. The air filling the neck acts as an incompressible fluid, moving like a mass block when excited by an external sound wave. This moving mass compresses the air within the cavity. The moving mass has kinetic energy, and the compressible air-filled cavity has potential energy. Consequently, the transfer of energy between these kinetic and potential energies within HR results in a vibrating system. HRs can be represented as a one-dimensional mass-spring-damper vibration system, as shown in Figure 1.2. The principal advantage of this acoustical network is its ability to create low-frequency resonance using dimensions much smaller than the long wavelength of an incident external low frequency sound wave. However, the operating frequency range is narrow [16].

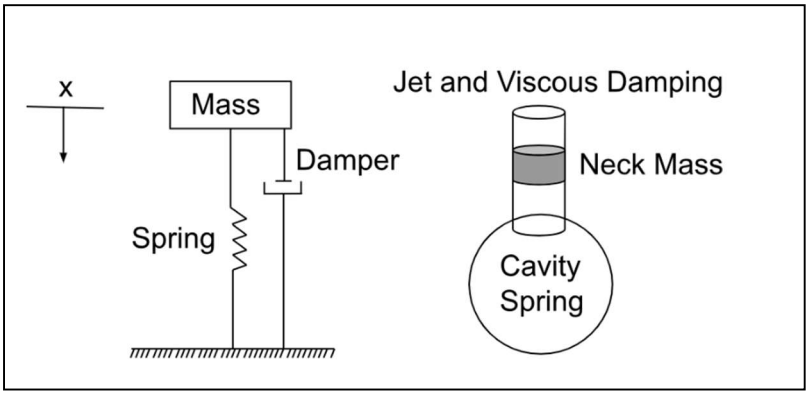

Figure 1.2. A schematic showing a single degree of freedom spring-mass-damper system representing classical HR.

Applications of HRs: The two main categories and common examples of the use of HRs may be as depicted in Figure 1.3:

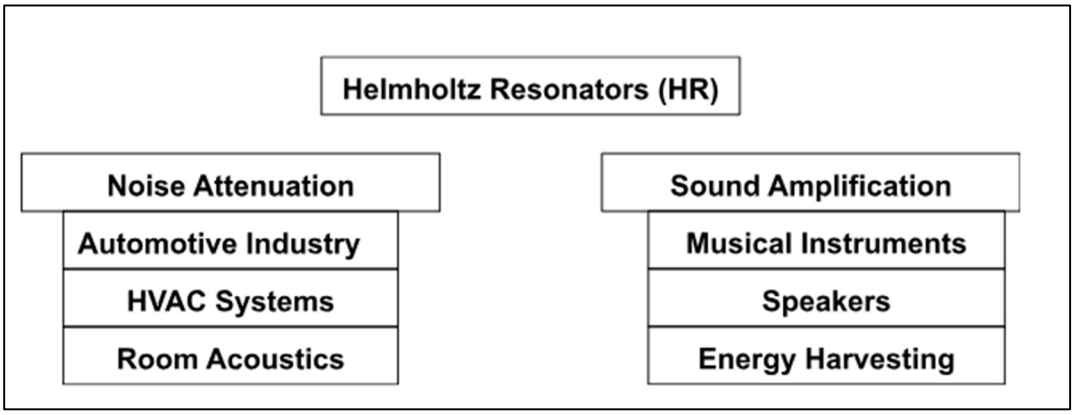

Figure 1.3. Diagram showing the two major categories which use HRs and most common examples.

HRs are extensively used in everyday systems for noise attenuation. Examples may include the chambers in reactive combustion engine mufflers, silencers, suppressors, and absorptive panels [17-20]. For sound amplification, common examples include cavities of

musical instruments, speakers, and energy harvesting [21-25]. Figure 1.4 shows HRs being used in everyday items.

Figure 1.4. Examples of the utility of HRs in everyday items such as mufflers and musical instrument [Stock Images, Royalty-Free Images, Illustrations, Vectors and Videos - iStock (istockphoto.com)**]**

HRs are also extensively used in scientific research. Typically, HRs can be used as stand-alone systems or coupled with another system. The setup includes noise sources (such as speakers, or environmental noise) which produce external sound energy through a sound propagating medium such as air, sometimes water and so on. One or more noise receivers (say, microphones) are used in experimental setups inside or outside the HR setup to measure and compare the resultant sound pressure levels [16]. Figure 1.5 provides a conceptual illustration of a typical experimental setup used in research involving HRs.

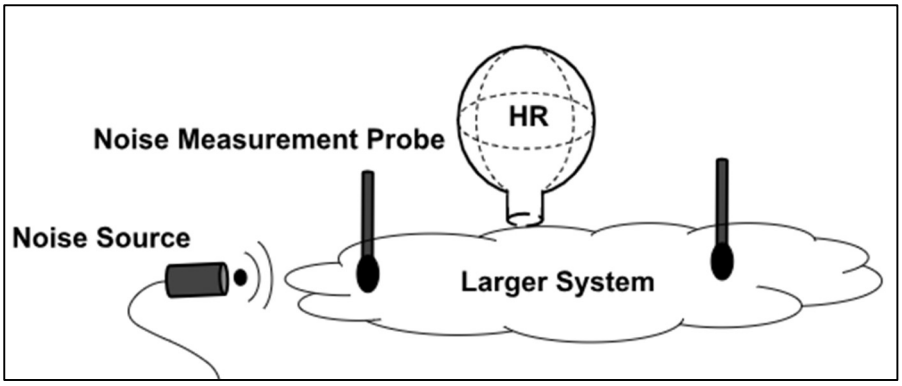

Figure 1.5. A typical layout of HR used in research.

Finally, HRs may also occur in nature. For example, gastropod seashells, as shown in Figure 1.6, which can sometimes be found near a beach, may amplify the noise emanating from the nearby sea [26, 27].

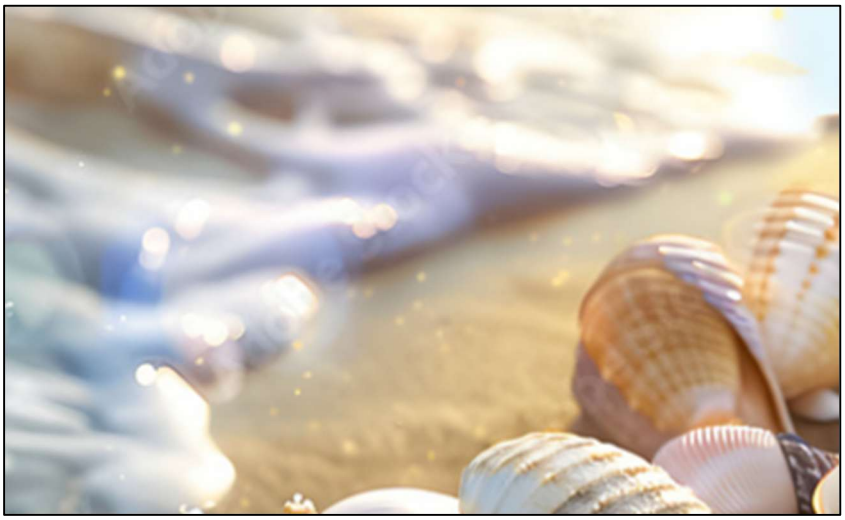

Figure 1.6. An example of naturally occurring HR. [Stock Images, Royalty-Free Images, Illustrations, Vectors and Videos - iStock (istockphoto.com)]

1.3 Literature Review

1.3.1 The Use of HRs for Noise Reduction

Noise reduction in HRs is attributed to the phenomenon of destructive standing wave interference, at resonance [28]. When HRs are used within a larger system where noise propagates, an incident acoustical wave enters the HR through the neck. The air within the neck acts as a block of mass which gains kinetic energy. It then compresses the air within the HR cavity which has potential energy. Consequently, the incident sound wave is reflected into the larger system, forming a standing wave. While maintaining the same frequency (because at resonance the wavelength of the low frequency incident waves is much larger than the dimensions of the neck or the cavity) as the incident wave, the reflected wave has traveled an additional half wavelength at resonance, introducing a phase delay and ultimately causing destructive interference in the larger system. It is important to note that HRs provide this phase delay at resonance due to the transfer of kinetic and potential energies between the neck (mass) and cavity (spring). Noise reduction by HRs can only be realized if they form a closed-end system when used in a larger system.

HRs can be used in lining materials to provide noise attenuation [29-32]. Typically, multiple HRs are used within the back-plated lining material in various configurations, for example, honeycomb and checkerboard patterns. This represents a significant improvement, as conventional lining materials (usually fibrous with high porosity) provide suitable noise reduction at higher frequencies but fail to reduce noise at lower frequencies [33]. Because lining materials have pores, the higher frequency noise, with smaller wavelengths, can be

captured by these pores, converting acoustical energy to heat. However, lower frequency noise, with larger wavelengths, bypasses the pores. By using HRs, liners benefit from the small dimensions of the HRs and their capability to reduce lower frequency noise.

The use of microperforated panels (MPPs) combined with cavity HRs was found to improve over the lower frequency deficiency of traditional fibrous lining materials and provide noise reduction within a broader bandwidth and resist harsher conditions such as high temperatures and pressures (for example, within an aircraft engine), compared to the conventional lining materials, However, MPPs fell short of providing continuous absorption. Each HR provided single peak noise reduction at the resonance; That is, the noise reduction was not smooth over the desired range of frequency for noise reduction. To overcome this, another layer of improvement was used which embedded HRs in metamaterials [34-37].

Metamaterials are engineered materials used to control and manipulate sound, light, and so on. Metamaterials are comprised of a series of elements whose size and spacing are much smaller than the scale of spatial variation of the exciting field [38-42]. Metamaterials introduce defects which can confine the acoustical wave energy to the defected area to achieve noise reduction. In [38-42] HRs were added to the defect of the metamaterial to increase the noise reduction at lower frequencies while keeping the overall dimensions as small as practicable in addition to offering a smoother attenuation across the desirable range of frequencies. The combination of HRs with metamaterials was among the latest developments in the pursuit of achieving broadband and smooth noise reduction with sound absorbers and HRs.

HRs are also used to attenuate noise generated by HVAC systems, engine noise, and flow-generated noise in ductwork and pipework systems, among many similar applications [43-53]. Reactive silencers, mufflers, and duct-mounted attenuators utilize one or more chambers of different shapes connected by sections of pipework that include expansion chambers and HRs. In addition to increasing the noise reduction at lower frequencies, HRs are also more resistant to harsh temperature and flow conditions, compared to dissipative silencers.

While HRs have been historically used in churches, concert halls and theaters, more modern applications can be found in architectural elements, such as windows, walls, tunnels, and similar elements [54-59]. The reason for the widespread use, both historically and contemporarily, is the deficiency of traditional construction materials (such as wood, steel, and concrete) in sound isolation in the lower frequency range. Like fibrous lining material and dissipative silencers, these materials exhibit the inability to reduce lower frequency noise due to the longer wavelengths that bypass the small pores in the materials. To overcome this deficiency in lower frequency sound isolation, HRs could be integrated into building construction materials such as concrete and masonry units [60-63]. These improved materials typically used an expanded clay aggregate, which was then poured into blocks having HR geometry.

In the study in this thesis, the objective is to investigate the noise reduction capabilities of a single HR coupled with a rectangular cuboid enclosure (commonly referred to as rectangular cavity) which may be used for noise mitigation in architectural spaces such as rectangular rooms.

1.3.2 The Use of HRs for Energy Harvesting

HRs are used in energy harvesting in two major ways: electromagnetic and piezoelectric [64-66]. When a magnetic field (produced by, for example, a pair of permanent magnets) moves relative to an electrical conductor (such as wires), an electrical potential is induced, with a magnitude proportional to the rate of change of the magnetic field [67-70].

HRs capture and amplify low-frequency acoustical energy from external sources of noise (such as vehicles, airplanes, trains, etc.). As the incident acoustic energy enters the HR, it can cause different parts of the HR's structure, say, the back plate of the cavity, to vibrate. When a pair of magnets are attached to the back plate, the vibrational force moves the magnets, inducing an electrical potential. This process converts the available acoustical energy into electric energy using HRs with magnets attached [71-74].

On the other hand, piezoelectric material transforms mechanical energy into electrical energy, and vice versa [75-77]. Direct piezoelectric refers to the transformation of mechanical deformation into electrical charge. The converse effect is when piezoelectric material is subjected to electrical potential difference across a specimen resulting in mechanical deformation. Rochelle salt, quartz, topaz, tourmaline, and cane sugar exhibit piezoelectric effects in nature. Piezoelectric energy harvesting devices are smaller, more sensitive to strain, flexible, and higher in energy output [78].

As the study in this thesis is involved with the energy harvesting capabilities of a single HR using piezoelectric material to convert acoustical energy to electrical energy, a more critical literature review regarding energy harvesting using piezoelectric materials is in order.

A recent experimental study demonstrated that when a piezoelectric beam was placed within the cavity of a spherical HR, and the system was excited with an acoustical signal between 90 dB and 110 dB at a frequency of 500 Hz, it harvested 0.2 V of electrical energy [79]. This setup resembled the HR subsystem employed in this thesis's study, as it used a semi-spherical cavity with similar physical dimensions and an embedded piezoelectric harvester. The study in [79] also suggested that the system could be used in locations such as schools, music venues and areas where people may converse, like the potential applications of the proposed system in this thesis.

Another research placed a circular piezoelectric film at the bottom of a cylindrical HR [80]. When the system was excited with an acoustical signal at 110 dB and a frequency of 831 Hz, it harvested 0.082 V of electrical energy. The authors of [80] proposed using this system near railways. They also stated that, while other studies used circular plates, this cylindrical HR with a circular piezoelectric membrane at the bottom of its cavity was novel because it focused on a lower frequency range of 831 Hz. It should be mentioned that the proposed HR in this thesis is aimed at even lower frequencies.

HRs are also used to harvest acoustical energy from metamaterials, using miniscule-sized HRs. With an incident sound pressure of 105 dB at 990 Hz, it harvested 0.2 V [81]. The main benefit of this system was its scalability to larger sizes and flat geometry. The researchers acknowledged that the overall frequency of the system shifted as HRs were placed within the metamaterial system [81]. Although this thesis is focused on a single HR, additional HRs can be used in practice to harvest even more energy; That is, the system is scalable. In the system in

[82], when the HR is coupled with the rectangular cavity, two frequencies appear on either side of the resonant frequency of the rectangular cavity (modal splitting [83]), which also influences the overall resonant frequency of the system.

A conical HR was proposed in [83] which had a cylindrical cavity with a conical neck. This system was excited by a sound pressure level of 94 dBA from 450 Hz to 550 Hz and harvested 1.4 V. The main advantage of this system was that it harvested energy from road traffic when embedded in a noise wall configuration which could collect traffic information and predict future traffic counts.

1.3.3 The Use of HRs for Noise Reduction and Energy Harvesting

HRs are used for simultaneous noise reduction and energy harvesting, particularly in the development of metamaterials [84]. In this thesis, a system is investigated that uses an HR coupled with a rectangular cavity to reduce noise and harvest energy using an embedded piezoelectric cantilevered beam inside the HR.

In a 2022 study, a research team used nine HRs graded in a stepped configuration with rectangular cavities embedding a cross-linked polypropylene (IXPP) ferroelectric film for energy harvesting [85]. The team used a sound pressure level of 100 dB, with the HRs operating at frequencies of 518 Hz, 602 Hz, and 690 Hz, respectively. The reported sound absorption coefficient was an average of 0.81, equivalent to a 14-dB drop. The average power output was approximately 1.43 nW. The team attributed the higher noise reduction to the use of multiple HRs of varying sizes.

In a 2020 study, researchers placed seven cylindrical HRs of varying sizes inside a rectangular cavity in a spiral configuration [86]. Using a sound pressure of 94 dB, they reported a noise reduction of 32.67 dB, attributed to the use of PVC (polyvinyl chloride) material, which also reduced the system's weight. The HRs utilized a trampoline-shaped PVDF (Polyvinylidene fluoride) film for converting acoustical energy to electrical energy, harvesting 0.7 μW with a resistive load of 1 kΩ, equivalent to 0.0265 V [86].

Another 2020 study investigated the joint noise reduction and acoustical energy harvesting capabilities of an array of HRs mounted on top of a rectangular cavity open at both ends [87]. The team used a sound pressure level of 97.1 dB, which was reduced to an average of 95 dB. The resonant frequency range of the HRs (which was 140 Hz) showed a noise reduction of 10 dB. The highest voltage output was 28.5 μW with a resistive load of 43 kΩ, equivalent to 0.6 V.

In a 2018 study, a cylindrical HR with a PVDF patch clamped to the side wall of the HR was investigated [88]. Using a sound pressure level of 1 Pa (94 dB), the PVDF membrane vibrated at 343 Hz and 402 Hz, producing voltage outputs of 0.136 V and 0.075 V, respectively. The study reported a transmission of nearly zero, corresponding to an average absorption coefficient close to unity.

The system studied in this thesis is like the above discussed research work in noise reduction and energy harvesting in that it is scalable for multiple HRs and operating with a host cavity (rectangular cavity). However, it uniquely leverages the modal resonance within the host

cavity as an additional energy source while attenuating noise at these resonant locations, with a negligible footprint compared to the size of the rectangular cavity.

1.4 Research Gaps and Objectives

As detailed in Section 1.3, previous studies have explored the use of Helmholtz Resonators (HRs) for either noise attenuation or energy harvesting. More recent developments have integrated HRs within metamaterials or multi-resonator arrays to achieve simultaneous noise reduction and energy harvesting. However, the dual functionality of HRs, specifically their ability to simultaneously attenuate noise and harvest acoustical energy, remains an area in need of further investigation. In particular, limited research has examined systems that leverage the modal resonances of a rectangular cavity both as a source requiring noise control and as an opportunity for acoustical energy harvesting using embedded piezoelectric harvesters. There exists a gap in the development of compact, low-frequency noise control devices, especially those targeting frequencies below 500 Hz, whose dimensions remain significantly smaller than the corresponding acoustic wavelengths. This study addresses that gap by investigating a simple, closed acoustical system employing a single HR integrated with a rectangular cavity to achieve dual functionality in a scalable and spatially efficient manner.

The primary objective of this research is to investigate the simultaneous noise reduction and acoustical energy harvesting capabilities of a coupled rectangular cavity system with a Helmholtz Resonator (HR). In achieving this objective, several intermediate goals are also examined:

1. Evaluating the sound amplification capabilities of a spherical HR under various acoustical excitations.
2. Analyzing modal resonance effects within a rectangular cavity when exposed to acoustical excitations near the corners.
3. Assessing the acoustical energy harvesting potential of a stand-alone HR unit using a cantilevered piezoelectric beam housed within the HR.
4. Developing finite-element (FE) models in ANSYS® that accurately represent the physical experimental environment.
5. Identifying the limitations associated with both physical experimentation and simulations and proposing key areas for improvement in future research.

1.5 Thesis Outline

This thesis consists of six chapters. Chapter 2 introduces the theoretical framework underlying stand-alone Helmholtz Resonators (HR), rectangular cavities, and the finite-element modeling of acoustical interactions. Chapter 3 outlines physical experimental measurements using a loudspeaker and a microphone to analyze the HR, rectangular cavity, and coupled system. The frequency response of each system under various acoustical excitations is presented, along with concluding remarks on the measurement results.

Chapter 4 presents the finite-element (FE) models in ANSYS®, calibrating the computational environment against the physical experimental results. It also discusses the development of the models and the corresponding simulation outcomes. Chapter 5 explores

optimization strategies for energy harvesting within the coupled cavity, evaluating different HR geometries and interior materials, followed by a critical analysis. Finally, Chapter 6 provides a succinct summary of key findings from the physical experiments and simulations while identifying areas for future research.

For ease of reference, the Reference section of this thesis lists bibliographies chapter by chapter. This would allow readers to quickly consult the relevant sources specific to the chapter they are engaged with.

Chapter 2 - Summary of Relevant Theories

This chapter is to present the following theories relevant to the research involved in this thesis. The chapter consists of: Sec. 2.1 - the natural frequency of the Helmholtz resonator (HR); Sec. 2.2 - the natural frequencies of a rigid-walled rectangular cavity, Sec. 2.3 – the basics of acoustics; and Sec. 2.4 - finite element modeling of acoustical interactions.

2.1 The Natural Frequency of the Helmholtz Resonator

The Helmholtz resonator (HR) can be analytically modeled as a single degree-of-freedom (DOF) system. The importance of finding the natural frequency of an HR is to select a geometry that not only generates a resonant frequency near the lower end of the audible frequency range (20 Hz to 20 kHz) as a stand-alone system but also produces a resonant frequency that aligns with the rest of the system - the rectangular cavity. In this study, selecting geometry was an iterative process involving experimentation with various geometries such as spheres and cylinders, adjusting dimensions such as the volume of the HR and the size of the neck. The final selection of the HR is the spherical glass aperture shown in Figure 2.1, where the neck diameter was 18 ± 1 mm with a length of 20 ± 1 mm. The volume of the spherical cavity was 269 ± 1 cc. Note that spherical glass apertures of different sizes were readily available, facilitating the experimentation to obtain a resonant frequency that was in the low hundreds and aligned with the resonant frequency of the rectangular cavity (which was also in the low hundreds).

The lumped parameter model is a simplification used in acoustical systems when the wavelengths are much larger than the overall dimensions of the HR. At room temperature, the

speed of sound is c = 343.6 m/s ($c = c_0 + 0.6T_c = 331.6 + 0.6 \cdot 20 = 343.6$ [1]), which means that if the frequency of the sound is, say, 300 Hz, the wavelength is [2] $\lambda = (343.6 \text{ m/s}) / (300 \text{ Hz}) = 1.145$ m. A comparison of the dimensions of HR (Figure 2.1) with wavelength λ shows that the lumped parameter approach is valid.

Figure 2.1. A glass spherical aperture with dimensions shown. [Amazon.com: Magic Season Decorative Glass Bottles with Cork Stopper (9 fl oz. Potion Bottles / 2 Pcs) : Home & Kitchen]

The lumped parameter approach models the HR as a vibration system consisting of a mass, a spring and a damper. As seen in Figure 2.2, the air in the neck portion of HR gives mass M, and the damping is considered negligible. For example, Ref. [3] pointed out that the Q-factor of HRs is $Q = 2\pi\sqrt{V(L'/A)^3}$. For the HR used in this thesis (details in Chapter 3 and meaning of symbols in latter part of this section), Q = 155.6. Since Q-factor is related to damping ratio by $Q = 1/(2\zeta)$, the corresponding damping ratio is ζ = 0.0032, which makes the vibration system underdamped. In fact, the Q-factor is also the gain at resonance [3].

The speed of sound in air is influenced by the density and the bulk modulus of the air, treating air as an ideal gas. The derivation of the speed of sound in an ideal gas can be conveniently found in the literature, for example [4], resulting in Eq. (2.1) which is commonly known as the Newton-Laplace equation.

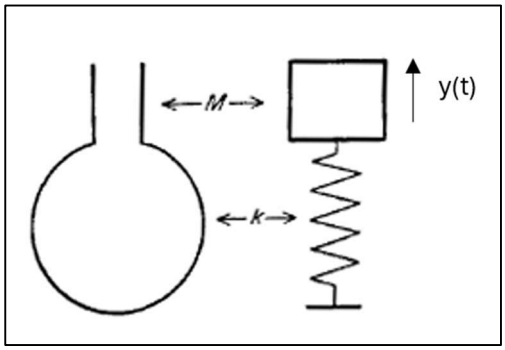

Figure 2.2. The mechanical-acoustical analogy of the Helmholtz resonator [4]

$$c^2 = \frac{\gamma p}{\rho} \qquad \textbf{Eq. (2.1)}$$

where c is the speed of sound in air; γ is the adiabatic index; p is the air pressure; and ρ is the density of air. The equation of motion (EOM) is [5]

$$M\ddot{y} + ky = 0$$

where y is the displacement. The natural frequency, or the resonant frequency, is [5]

$$\omega_n = \sqrt{k/M} \qquad \textbf{Eq. (2.2)}$$

To determine the spring constant k, the air is treated as ideal gas and the resonant process as an adiabatic process ($pV^{\gamma} = \text{constant}$). As a result, the differential change in pressure is:

$$dp = -\gamma p \frac{dV}{V} = -c^2 \rho \left(\frac{dV}{V}\right) = -c^2 \rho \left(\frac{Ady}{V}\right) = -c^2 \rho \frac{A}{V} dy$$

$$\therefore\ k = -\frac{Adp}{dy} = c^2 \frac{\rho}{V} A^2 \qquad \textbf{Eq. (2.3)}$$

where A is the area of the neck and V is the volume of the cavity. Substituting Eq. (2.3) into Eq. (2.2), and noting the $\omega_n = 2\pi f$, the resonant frequency f is found to be, in Hz,

$$2\pi f = \omega_n = c\sqrt{\frac{\rho A^2}{VM}} = c\sqrt{\frac{\rho A^2}{V\rho AL}} = c\sqrt{\frac{A}{VL}}$$

$$\therefore\ f = \frac{c}{2\pi}\sqrt{\frac{A}{VL}} \qquad \textbf{Eq. (2.4)}$$

where c is the speed of sound in air and L is the neck length. To consider the fact that the air in the neck portion vibrates as well, a length correction has been proposed [6] such that

$$\therefore\ f = \frac{c}{2\pi}\sqrt{\frac{A}{VL'}} \qquad \textbf{Eq. (2.5)}$$

where the corrected length is L’ = L + 1.5·r (r being the radius of the neck).

2.2 The Natural Frequencies of a Rigid-Walled Rectangular Cavity

The rectangular cavity here refers to rectangularly shaped enclosures. In literature, such enclosures are commonly known as rectangular cavities. Finding the natural frequencies of a rigid-walled rectangular cavity or a rectangular room starts with the wave equation [7]

$$\nabla^2 p - \frac{1}{c^2}\frac{\partial^2 p}{\partial t^2} = 0 \qquad \textbf{Eq. (2.6)}$$

or

$$\frac{\partial^2 p}{\partial x^2} + \frac{\partial^2 p}{\partial y^2} + \frac{\partial^2 p}{\partial z^2} + k^2 p = 0 \qquad \textbf{Eq. (2.7)}$$

where $p = p(x, y, z, t)$ is the sound pressure, and $k = \frac{\omega}{c}$ (c = the speed of sound in air; ω = the circular frequency of p [8]). Note that k^2 represents the eigenvalues and k is known as the wave number.

A rigid-walled rectangular cavity (Figure 2.3) has been found to have the following natural frequencies [9]

$$f_{l,m,n} = \frac{c}{2}\sqrt{\left(\frac{l}{L_x}\right)^2 + \left(\frac{m}{L_y}\right)^2 + \left(\frac{n}{L_z}\right)^2} \qquad \textbf{Eq. (2.8)}$$

where L_x, L_y and L_z are the side lengths of the cavity, and l, m, and n are integers having values from zero to infinity. Together they identify the mode of the sound wave. For example, in this

thesis, the dimensions of the cavity are (L_x, L_y, L_z) = (626.5, 472.5, 120.5) mm. As a result, the lowest natural frequency, or the resonant frequency corresponds to the mode (1, 0, 0).

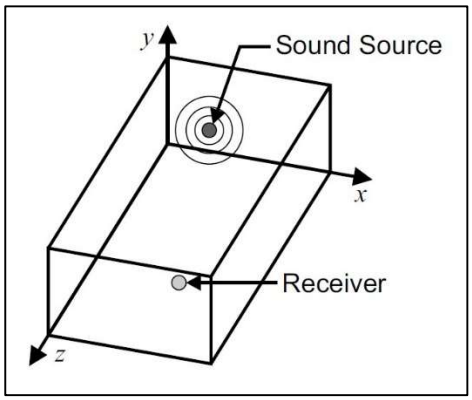

Figure 2.3. A rectangular cavity with sound source and receiver. [10]

It should be noted that Eq. (2.8) was derived based on the rigid-walled boundary conditions; that is, the sound pressure gradient along the normal to any wall is zero or the normal component of particle velocity is zero at all boundaries [11, 12]. Therefore, the mode shapes of the sound pressure are [9]

$$\Psi_{l,m,n}(x,y,z) = \cos\frac{l\pi x}{L_x}\cos\frac{m\pi y}{L_y}\cos\frac{n\pi z}{L_z} \qquad \textbf{Eq. (2.9)}$$

and the pressure and particle velocity [10] are

$$p(x,y,z,t) = \sum p_{l,m,n}\Psi_{l,m,n}(x,y,z)e^{i\omega t} \qquad \textbf{Eq. (2.10)}$$

$$v(x,y,z,t) = \frac{p(x,y,z,t)}{\rho_0 c} \qquad \textbf{Eq. (2.11)}$$

where $p_{l,m,n}$ are constants; ρ_0 is the density of air, and c is the speed of sound in air.

In passing, it should be mentioned that Ref. [10] also stated two other conditions or assumptions regarding Eq. (2.8): the sound source and the receiver are both placed inside the cavity [10]. However, such conditions are not included in, for example, [12 – 14]. The conditions listed in [10] may have to do with computational modeling.

2.3 The Basic Concepts in Acoustics

The basics of acoustics is presented here to facilitate discussions. However, it is not meant to be comprehensive.

2.3.1 Octave Bands

The audible sound frequency (to human hearing) is between 20 Hz and 20 kHz. It is customary to divide this range is divided into 1/1 or 1/2 or 1/3 octave bands. This is because [15], (1) human hearing is not equally sensitive to all frequencies; and (2) it allows analysts and researchers to separate complex continuous sound signals into a series of contiguous frequency bands using a sound analyzer. In this thesis, the 1/1 octave bands will be used. Each band has a center frequency, also low and high frequencies, as presented in Table 2.1 where only the three octave bands of interest are listed, and band numbers are in reference to 1/3 octave bands.

Table 2.1. Octave bands [16]

Band number	Lower band limit	Center frequency	Upper band limit
21	88	125	177
24	177	250	355
27	355	500	710

It is noted that [17]:

(1) the center frequencies of the next and current bands are related by $f_{n+1} = f_n / 2$; and,

(2) the lower and higher band frequences of a band are determined by $f_{n,lower} = f_n / \sqrt{2}$ and $f_{n,upper} = f_n \sqrt{2}$.

2.3.2 Near Versus Far Field Regime

In acoustics, the quantity kr (where $k = 2\pi f / c$ is the wave number, and r is the distance between the source and the receiver) can be used to determine whether the sound field is near or far. Based on [18], the receiver is in a near field regime if $kr < 0.1$ and a far field regime if $kr > 5$. For this research, r is approximately 0.6 m and c = 343.6 m/s, therefore the sound receiver is in the near field regime if $f < 5.5$ Hz (approx.) and in the far field regime if $f > 273.4$ Hz approx. Considering the range of frequency listed in Table 2.1 (i.e., 88 to 710 Hz) it is safe to conclude that the sound receiver in located in a far field.

2.3.3 Small Versus Large Enclosures

Enclosures can be classified as small and large enclosures. In small enclosures, the sound field is predominantly the direct field. In a large enclosure the sound field is of the reverberant kind. Some simple ways to determine if an enclosure is small or large are: $f L_{max} / c \leq 0.1$ for small enclosures [19] and $f \geq c / \sqrt[3]{V_0}$ for large enclosures [20], where f is the frequency, c is the speed

of sound in air, V_0 is the volume of the enclosure, and L_{max} is the largest dimension of the enclosure. Taking V_0 = (0.6265) (0.4725) (0.1205) m^3 = 0.03567 m^3, L_{max} = 0.6265 m and c = 343.6 m/s, it is seen that the rectangular cavity experimented with in this thesis is a small enclosure if $f \leq 55$ Hz and a large enclosure if $f \geq 1044$ Hz. For the range of frequency listed in Table 2.1 (88 to 710 Hz), the rectangular cavity used in this thesis is in the mid-range, which does not lead to a conclusion of direct or reverberant field. However, the discussion regarding near or far field has indicated that the rectangular cavity of interest has a reverberant field.

2.4 Finite Element Modeling of Acoustics

Finite element modeling will be used in this research to investigate the natural frequencies, the frequency response under acoustical excitation of the Helmholtz Resonator (HR) and the rectangular cavity, and the coupling of the two systems when connected through adjoining construction.

As stated in Sections 2.1 and 2.2, analytical solutions have been employed to predict the theoretical natural frequencies of HR and the rectangular cavity. However, as the system's geometry becomes more complex [21] and a more detailed analysis of various points within the enclosed volume is required [22], the finite element method (FEM) becomes the preferred approach for advancing the acoustical analysis in this research.

Additionally, as the complexity of the acoustical region increases, the need for a higher-accuracy FEM approach also grows. This requires finer discretization of the domain, three-dimensional subdivision of the acoustical region, and a higher number of degrees of freedom.

Since analytically solving all terms under these conditions is impractical, the use of acoustic computation software such as ANSYS® Student 2024 R2 becomes essential [23].

While this study primarily relies on experimental work to draw key inferences about the complex acoustical geometries being investigated, experimentation has inherent limitations. Therefore, mathematical and computational modeling, such as FEM, can be used to validate the experimental results (and vice versa) and further refine the acoustical investigation. The details of the experimental work will be outlined in Chapter 3, while Chapter 4 will discuss the limitations of experimental methods and the rationale for using ANSYS® Student 2024 R2 to develop the FEM model. Chapter 5 will investigate the potential for optimization of energy harvesting potential for the coupled system within the HR geometry using ANSYS® Student 2024 R2.

2.4.1 Equations of Motion

This section provides an overview of the framework within which FEA (finite element analysis) is conducted, with a focus on modal analysis as the foundation of this research.

The matrix form of the equations of motion for an acoustical system (such as the rectangular cavity), is [24]:

$$(-\omega^2[\boldsymbol{M}] + j\omega[\boldsymbol{C}] + [\boldsymbol{K}])\{p\} = \{f\} \qquad \textbf{Eq. (2.12)}$$

where $[\mathbf{M}]$ is the mass matrix, [**C**] is the damping matrix, [**K**] is the stiffness matrix, $\{p\}$ is the vector of nodal pressure, and $\{f\}$ is the acoustical excitation being applied to the system. ω is

the circular frequency (rad/s), and j is the imaginary unit. For acoustical modal analysis, damping is assumed negligible, and the excitation is removed from Eq. (2.12), Therefore:

$$\{p\} = \{\phi_n\}\cos(\omega_n t) \qquad \textbf{Eq. (2.13)}$$

where $\{\boldsymbol{\phi_n}\}$ is the eigenvector of pressures of the nth natural frequency, ω_n is the natural circular frequency (radians/s), t is time in seconds (s). Substituting Eq. (2.13) back in Eq. (2.12) gives:

$$(-\omega^2[\boldsymbol{M}] + [\boldsymbol{K}])\{\boldsymbol{\phi_n}\} = \{0\} \qquad \textbf{Eq. (2.14)}$$

Neglecting the trivial solution $\{\boldsymbol{\phi_n}\} = \{0\}$, the determinant should become zero:

$$|[\boldsymbol{K}] - \omega_n^2[\boldsymbol{M}]| = 0 \qquad \textbf{Eq. (2.15)}$$

It should be noted that the above modal analysis is well-known in dynamics and vibration, where the solutions of Eq. (2.15) give the natural circular frequencies ω_n. In ANSYS®, the solutions are in the form of natural frequencies f_n, in Hz.

$$f_n = \frac{\omega_n}{2\pi} \qquad \textbf{Eq. (2.16)}$$

2.4.2 Equations of Harmonic Response

The results from the modal analysis in ANSYS® can be used to study the response due to acoustical excitation [25]. The harmonic response of a system due to acoustical excitation can be calculated using the following equations:

$$[\boldsymbol{M}]\{\ddot{p}\} + [\boldsymbol{C}]\{\dot{p}\} + [\boldsymbol{K}]\{p\} = \{f\},$$

$$-\omega^2[\boldsymbol{M}]\{p\} + j\omega[\boldsymbol{C}]\{p\} + [\boldsymbol{K}]\{p\} = \{f\},$$

$$(-\omega^2[\boldsymbol{M}] + j\omega[\boldsymbol{C}] + [\boldsymbol{K}])\{p\} = \{f\} \quad \textbf{Eq. (2.17)}$$

Where $\{p\}$ is the acoustic pressure, and therefore is:

$$\{p\} = (-\omega^2[\boldsymbol{M}] + j\omega[\boldsymbol{C}] + [\boldsymbol{K}])^{-1}\{f\}. \quad \textbf{Eq. (2.18)}$$

The acoustic pressure *p* within the FE domain in ANSYS® is [26]:

$$p = \sum_{i=1}^{m} N_i p_i \quad \textbf{Eq. (2.19)}$$

where N_i is a set of shape functions, p_i are acoustic nodal pressures at node i, and m is the number of nodes forming the element. For pressure-formulated acoustic elements, the finite element equation becomes [25]:

$$[\boldsymbol{M_f}]\{\ddot{p}\} + [\boldsymbol{C_f}]\{\dot{p}\} + [\boldsymbol{K_f}]\{p\} = \{F_f\} \quad \textbf{Eq. (2.20)}$$

where $[\boldsymbol{K_f}]$is the equivalent fluid stiffness matrix, $[\boldsymbol{M_f}]$ is the equivalent fluid mass matrix, $[\boldsymbol{C_f}]$ is the equivalent fluid damping matrix, $\{F_f\}$ is a vector of applied fluid loads, $\{p\}$ is a vector of un-known nodal acoustic pressures, $\{\dot{p}\}$ is a vector of the first derivative of acoustic pressure, and $\{\ddot{p}\}$ is a vector of the second derivative of acoustic pressure with respect to time.

2.4.3 Acoustic Element Modelling in ANSYS®

In meshing or discretization of the FE models in ANSYS®, this research utilized FLUID220, a three-dimensional, second-order Hex20 (twenty-node hexahedral) element for the rectangular

cavity, and FLUID221, a three-dimensional, second-order TET10 (ten-node tetrahedral) element for the coupled system with an HR connected to the rectangular cavity [26].

The FLUID220 element employs a quadratic shape function, that allows a quadratic variation in the cross-sectional area and acoustic pressure [27]. This can result in a more accurate representation of the overall acoustic pressure compared to a lower-order element with a linear shape function, such as FLUID30 [28]. The use of a higher order element requires performing more calculations over higher degrees of freedom. The decision to use higher order elements inevitably results in a higher computational cost due to the greater number of integration points needed and extra complexity in the input data [29]. FLUID221 is similar to the FLUID220 element, with a 10-node tetrahedral geometric shape instead. The coupled system which uses a combination of HR and rectangular cavity simultaneously, will be discretized by the TET10 tetrahedral elements in this research, as this type of element is suitable for use where the geometry becomes more complex (than, say, a rectangular shape), and difficult to mesh with hexahedral (brick) elements [30].

The theoretical framework established in this chapter serves as the basis for the experimental and numerical investigations presented in the subsequent chapters.

Chapter 3 - Experiments and Results

This chapter contains the experimental methodology and findings associated with a stand-alone Helmholtz resonator (HR), a rectangular cavity, and a coupled system consisting of the HR and rectangular cavity, with and without energy harvesting by a piezoelectric module (or chip). The organization of the chapter is as follows: Sec. 3.1 - The experimental methodology; Sec. 3.2 - Experimental results and discussions and Sec. 3.3 - Concluding remarks. Sec. 3.2 is further divided into four sub-sections: Sec. 3.2.1 - a stand-alone HR subject to excitations; Sec. 3.2.2 - a rectangular cavity subject to excitations; Sec. 3.2.3 - the coupled system subject to excitations; and Sec. 3.2.4 - energy harvesting by the HR and coupled system.

The primary purpose of this chapter is to demonstrate, via experimental work, the behaviors of the stand-alone HR, the rectangularly shaped enclosure (or the rectangular cavity as it is commonly referred to as in the literature), and the coupled system of the HR and rectangular cavity, in particular the behaviors near the resonant frequency of the HR. It is also to demonstrate the capacities in energy harvesting of the systems of HR-piezoelectric, and HR-rectangular cavity-piezoelectric.

3.1 Experimental Methodology

The most critical aspect in selecting the sizes and geometry of ***the Helmholtz resonator*** (HR) is that it not only generates strong resonance within the lower audible frequency range as a stand-alone system but, more importantly, produces resonant frequencies that align with the rest of the system. This was an iterative process involving experimentation with various

geometries and dimensions related to the cavity volume and neck dimensions. In this study, HRs with spherical cavity and cylindrical neck were selected due to their ready availability. After iterations of experimentation, a spherical glass aperture was chosen and used as the HR where the neck diameter was 18 ± 1 mm with a length of 20 ± 1 mm. The volume of the spherical cavity was 269 ± 1 cc (cubic centimeter), see Figure 3.1.

Figure 3.1. An image of the spherical glass aperture [Amazon.com: Magic Season Decorative Glass Bottles with Cork Stopper (9 fl oz. Potion Bottles / 2 Pcs) : Home & Kitchen]

Based on Eq. (2.5) (or [1]), the resonant frequency of the HR is found to be f = 291 Hz where $A = \pi\,(18\times10^{-3}\text{ m})^2/4 = 0.2545\times10^{-3}\text{ m}^2$, $V = 269\times10^{-6}\text{ m}^3$, $L' = 20\text{ mm} + 1.5\cdot18\text{ mm}/2 = 33.5\times10^{-3}\text{ m}$, and c = 343.6 m/s at room temperature [2]. The lower and upper estimates of the resonant frequencies are, respectively, 267 and 316 Hz.

Apertures made of glass was chosen also because glass demonstrates a very low coefficient of sound absorption. When sound waves strike the glass aperture at the boundary of glass and outside air, most of the incident acoustic wave is reflected back and only a small amount of incident acoustic energy is absorbed by the glass aperture. The coefficient of sound

absorption at 125 Hz is 0.35 and it decreases to 0.25 at 250 Hz for glass [3]. A value of unity for the coefficient of sound absorption means that the incident acoustic energy is entirely absorbed by the material. A zero coefficient of sound absorption, on the other hand, indicates that the incident acoustic energy is entirely reflected.

A loudspeaker (Logitech UE Boom 2) was utilized to excite the HR to establish the resonant frequency experimentally.

A Piccolo II (soft dB) professional integrating-averaging IEC 61672/ANSI S1.4 Class 2 sound omni-directional microphone was used to log/record the sound pressure associated with the background sound pressure level and inside the HR near the neck. The microphone has a 30 to 130 dBZ dynamic range and 20 Hz to 16 kHz frequency span. It is also capable of recording one-second equivalent continuous average sound pressure level Leq (1 sec) in A, C, and Z weightings. While A and C-weighting apply corrections to mimic the perception of audible noise for the human sensory system, the Z-weighting was used in this study because it does not include any corrections and reflects the true sound pressure level (SPL) as measured. In Sec. 3.2, the recorded SPL is denoted as "one-second overall sound pressure level LZeq (dB)". It is noted that LZeq (dB) or LZeq (1 sec) is the Z-weighted SPL in decibels. SPL is sound pressure amplitude integrated over a certain time duration, divided by the time duration. One-second is the shortest logging time interval for LZeq when using the Class 2 omni-directional microphone.

An online ***signal generator*** [Online Tone Generator - generate pure tones of any frequency (szynalski.com)] was used to generate tonal sinusoidal signals and broadband pink noise acoustic signals to sweep the HR while the microphone logs the LZeq (1 sec) and

frequency spectral data. The pink noise signal was used as a first test to quickly establish the neighborhood of the resonant frequency. This is because the pink noise signal contains the audible frequency tones (20 Hz to 20 kHz) simultaneously with equal energy density, monitoring the frequency response of the HR gives the resonant frequencies. Once the neighborhood of the dominant resonant frequency was established, a sinusoidal signal was then used to excite the HR at the established resonant frequency. This would give better resolutions in recorded data.

A rectangular cavity of the dimensions 626.5 × 472.5 × 120.5 mm^3 was constructed of from acrylic sheets with a thickness of 5.88 mm. The sheets were glued using all-purpose construction grade liquid latex adhesive at the conjunctions of all six surfaces. Next, the adjoining surfaces were caulked using non-hardening acoustical sealant to reduce any large gaps or holes around the perimeter at the junctions. The near airtight construction of the rectangular cavity prevents sound from flanking from weak points such as cracks or gaps at the adjoining acrylic surface junctions.

Using Eq. (2.8) or [4], the lowest five natural frequencies of the rectangular cavity, when the walls are rigid, are listed below in Table 3.1.

Table 3.1. Lowest natural frequencies of rigid-walled rectangular cavity*

Natural Frequency	(l, m, n)	f (Hz)
Lowest	(1, 0, 0)	274
Second Lowest	(0, 1, 0)	363
Third Lowest	(1, 1, 0)	455
Fourth Lowest	(2, 0, 0)	548
Fifth Lowest	(2, 1, 0)	658

* L_x = 626.5 mm = 0.6265 m, L_y = 472.5 mm = 0.4725 m, L_z = 120.5 mm = 0.1205 m, and c = 343.6 m/s.

It should be noted that the above natural frequencies, plus the estimates of the resonant frequency of HR (between 267 and 316 Hz) are well within the three octave bands listed in Table 2.1. In presenting experimental results as will be seen in later sections of this chapter, the range of frequency is set to 88 to 710 Hz, despite of the fact that the instrument, the microphone in particular, is capable of a 30 dB to 130 dB dynamic range and has a 20 Hz to 16 kHz frequency span.

A piezoelectric beam [PIEZO VIBRATION SENSOR (leeselectronic.com)] was placed inside the HR to demonstrate the energy harvesting capabilities of the spherical glass aperture. Next, the HR was incorporated outside the rectangular cavity and the coupled system of HR-rectangular cavity to show the energy harvesting capacities. Figure 3.2 shows the LDT0-028K piezoelectric module [LDT_Series.pdf (dlnmh9ip6v2uc.cloudfront.net)]. It has laminated flexible PVDF piezoelectric polymer fitted with two crimped leads at one end for electrical output

connection. The beam is 28 µm thick with a 0.125 mm laminated substrate without any added tip mass. The piezoelectric beam was clamped at one end using an electrical clip and free on the other end.

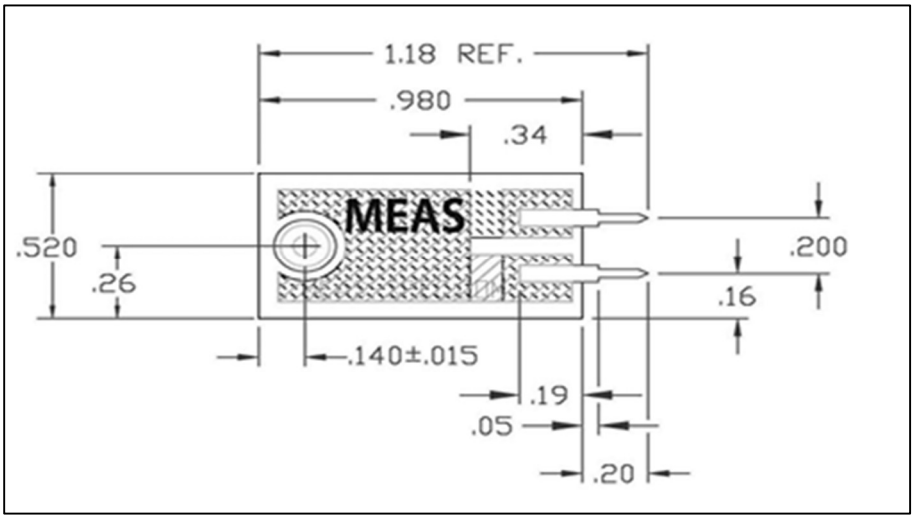

Figure 3.2. Top view of the piezoelectric module [LDT_Series.pdf (dlnmh9ip6v2uc.cloudfront.net)]

Finally, ***a handheld Hantek oscilloscope*** was used to monitor the electrical AC voltage output of the piezoelectric beam. The oscilloscope was clipped to the two ports of the piezoelectric and the voltage output was sent to a laptop for ease data acquisition.

Figure 3.3 below shows the experimental setup and instrumentation that was used. As will be seen in later sections of the chapter, the experiments include,

1. measuring the background noise level without the HR, the rectangular cavity, and the coupled HR-rectangular cavity system.

2. measuring the sound pressure levels (SPLs) of the HR, the rectangular cavity, and the coupled system of HR-rectangular cavity using a pink noise signal to monitor the frequency response for each system and identify the resonant frequency.
3. exciting the systems with a sinusoidal signal of the identified resonant frequency to obtain the frequency response of the individual systems; and
4. recording the voltage measurements for the stand-alone HR system with a piezoelectric beam, and the coupled HR-rectangular system.

The logged data by the Class 2 sound omni-directional microphone are exported into Microsoft Excel for signal processing. Such data include the one-second LZeq for both the overall average sound pressure level and spectral data.

It should be noted that in this chapter, background noise refers to noise or sound without the HR or the cavity or the coupled system, but subject to an excitation. Therefore, it should not be confused with the ambient noise or sound. On SPL spectra presented in the chapter, the background noise is denoted as "*BG*".

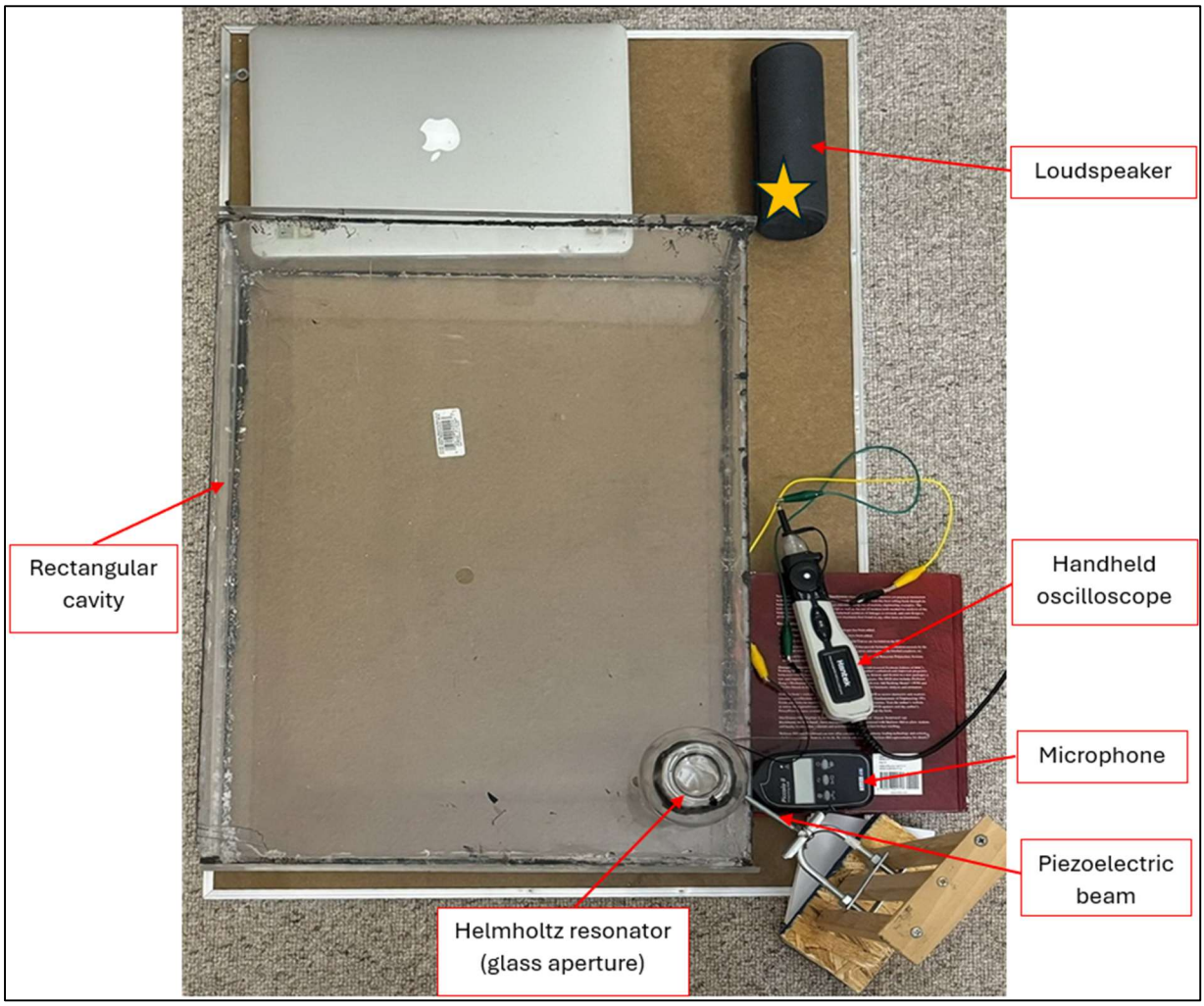

Figure 3.3. The experimental setup using a loudspeaker, microphone, handheld oscilloscope, signal generator from laptop, Helmholtz resonator, rectangular cavity, piezoelectric beam, and a stand. The "star" indicates the location of sound source. The rectangular cavity is fully enclosed.

Table 3.2 summarizes the experiments conducted so far. It should also be mentioned that all the experiments were not conducted in a controlled laboratory environment.

Table 3.2. Summary of experiments conducted

Experiment	Excitation	Section and figures where results are shown
HR only	Pink noise at 99, 90, 80, 71 and 58 dB	3.2.1 (Figures 3.5 – 3.9)
HR only	Tonal signal of 90 and 58 dB at 307 Hz	3.2.1 (Figures 3.10 – 3.11)
Rectangular cavity	Pink noise at 90 and 58 dB	3.2.2 (Figures 3.13 – 3.14)
Rectangular cavity	Tonal signal of 90 and 58 dB at 307 Hz	3.2.2 (Figures 3.15 – 3.16)
Coupled system	Pink noise at 90 and 58 dB	3.2.3 (Figures 3.18 – 3.19)
Coupled system	Tonal signal of 90 and 58 dB at 307 Hz	3.2.3 (Figures 3.20 – 3.21)
Energy harvesting by the HR	Tonal signal of 90 dB at 307 Hz	3.2.4 (Figure 3.24)
Energy harvesting by the coupled system	Tonal signal of 90 dB at 307 Hz	3.2.4 (Figure 3.25)

3.2 Experimental Results and Discussions

3.2.1 Helmholtz Resonator Subject to Excitations

The experimental set up is shown in Figure 3.4. A pink noise signal was generated using the online signal generator to excite the spherical glass aperture. A pink noise signal is suitable since the energy density within the frequency spectrum is equal. A pink noise signal is a broadband signal.

The pink noise was generated with several “loudness” or sound pressure levels (SPL) as measured by decibel (dB). For each SPL, two one-second duration signals were collected: one with the HR, the other without which represented the background sound. The overall SPL signals were subsequently analyzed by Microsoft Excel to obtain the one-second overall SPL spectra. Figures 3.5 through 3.9 show the spectra (as measured by dB or dBZ) when subject to pink noises of SPLs of 99, 90, 80, 71 and 58 dB, respectively. It can be seen from Figures 3.5 through 3.9 that

1. The SPL spectra illustrated in Figures 3.5 through 3.8 show very similar trend: (a) below approx. 200 Hz, the HR does not gain in SPL, nor does it experience losses in SPL; (b) near 307 Hz, the HR resonates as indicated by the increase in SPL over the background’s SPL; and (c) above approx. 500 Hz, the decrease in SPL, HR compared with the background, seems uniform across frequencies 500–710 Hz when subject to pink noise of the same SPL.

2. Figures 3.5 through 3.8 show that there is a rather consistent increase in SPL at or near 307 Hz. This increase seems to be independent of the SPL of excitation. For pink noise

SPLs of 99, 90, 80 and 71 dB, respectively, the increases in HR's SPLs are 17, 18, 17 and 19 dB, respectively. An increase of 17 dB in SPL is perceived as approx. 3.25 ($=2^{(17/10)}$) times as loud.

3. When the pink noise excitation is at 58 dB (Figure 3.9), the SPLs of the HR and background are rather close to each other. At 307 Hz, the SPL in the HR sees an increase to 65 dB from 58 dB.

4. The locations of the peaks are between 302 and 310 Hz. They are within the mid to upper estimates of the resonant frequency (291-316 Hz). Hereinafter, 307 Hz is referred to as the resonant frequency of HR.

It is worth noting that going with SPLs (or "loudness") below what is outlined here requires access to specialized laboratory environment. At this juncture, it may be concluded that HR consistently increases the background's SPL, independent of the excitation's sound pressure level.

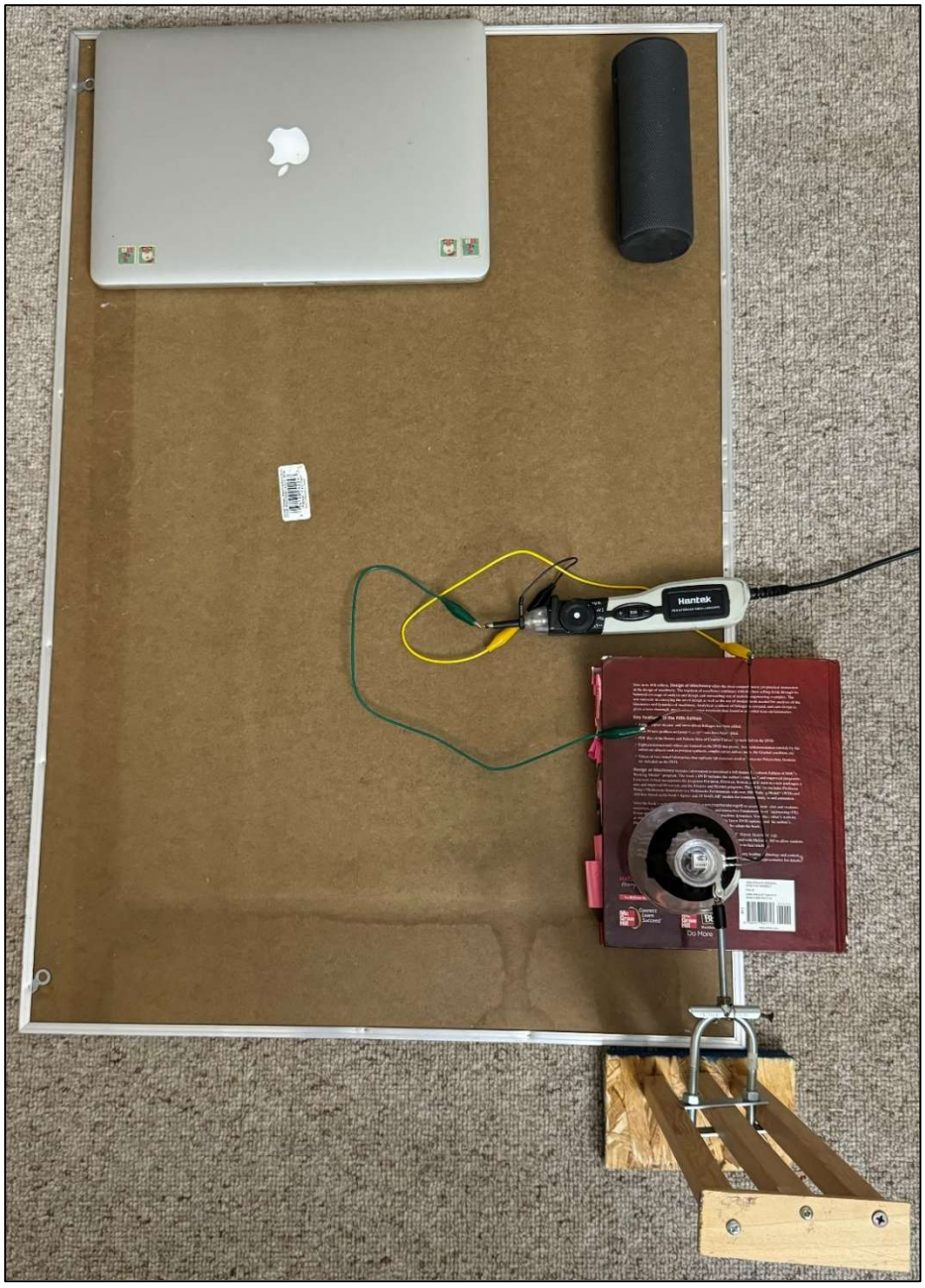

Figure 3.4. The experimental setup using a loudspeaker, handheld oscilloscope, signal generator from laptop, Helmholtz resonator, piezoelectric beam, and stand.

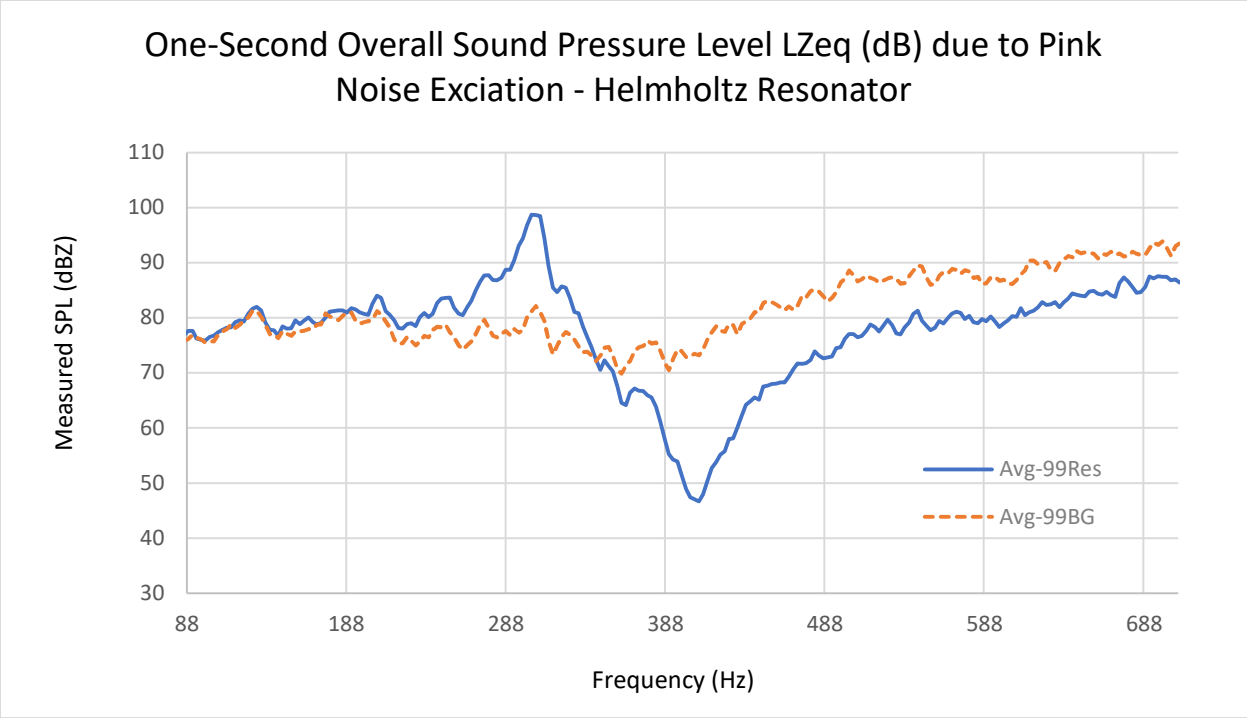

Figure 3.5. Graph showing the measured spectrum from pink noise excitation (99 dB) within the Helmholtz resonator and without any resonator (or 'BG')

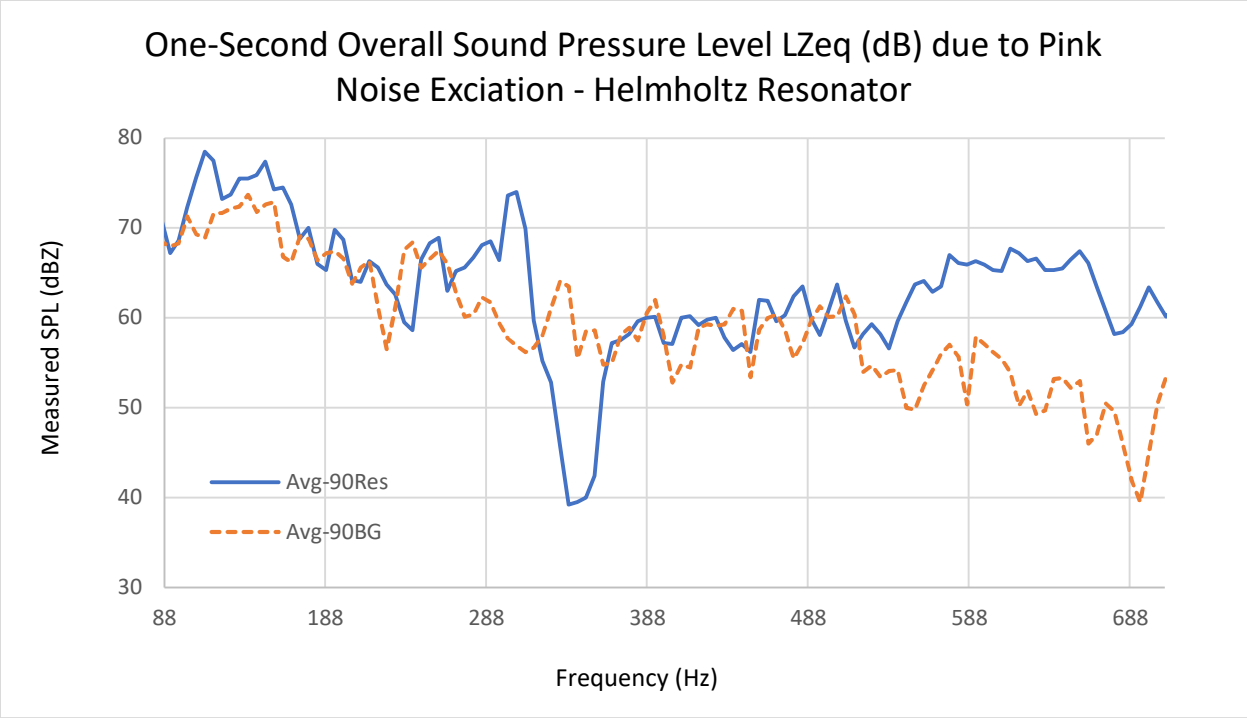

Figure 3.6. Graph showing the measured spectrum from pink noise excitation (90 dB) within the Helmholtz resonator and without any resonator (or 'BG')

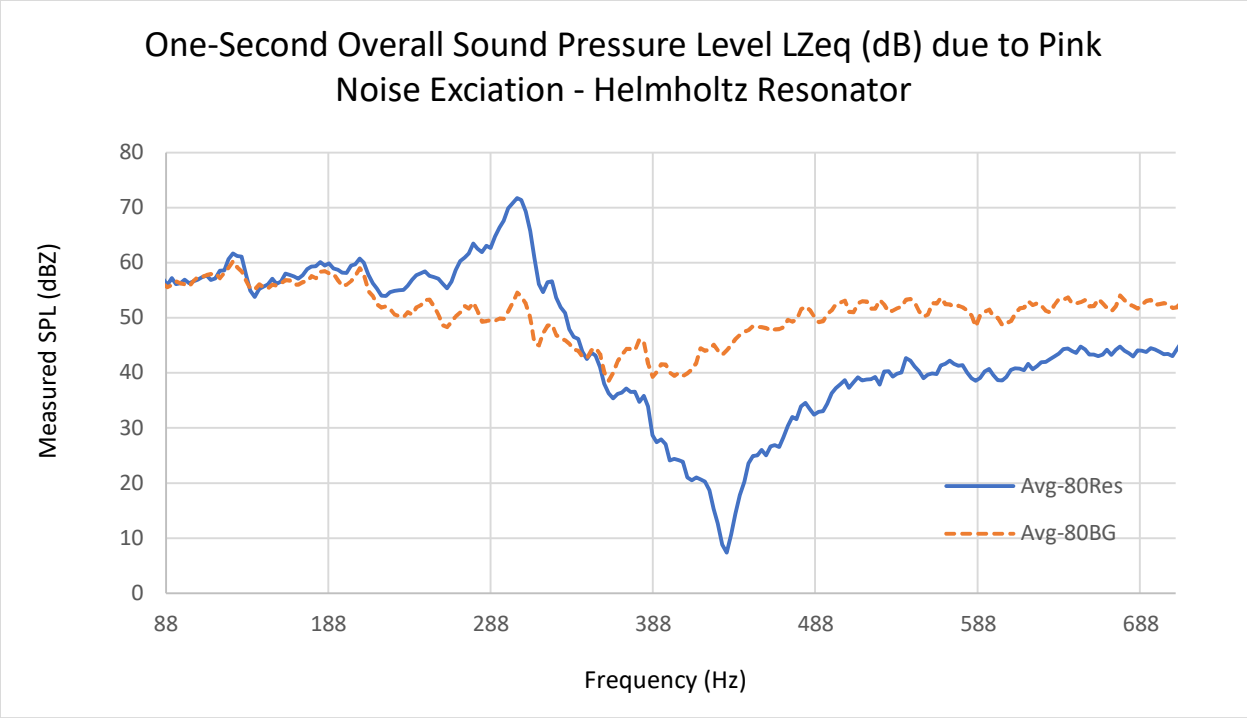

Figure 3.7. Graph showing the measured spectrum from pink noise excitation (80 dB) within the Helmholtz resonator and without any resonator (or 'BG')

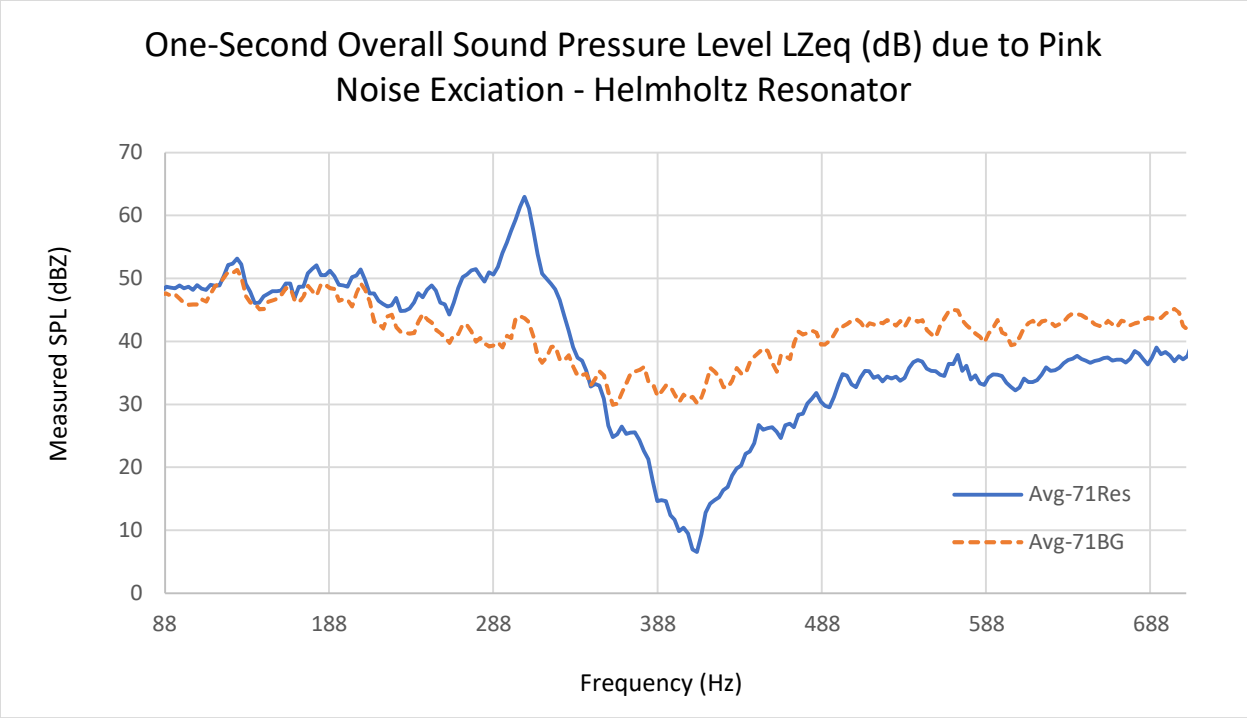

Figure 3.8. Graph showing the measured spectrum from pink noise excitation (71 dB) within the Helmholtz resonator without any resonator (or 'BG')

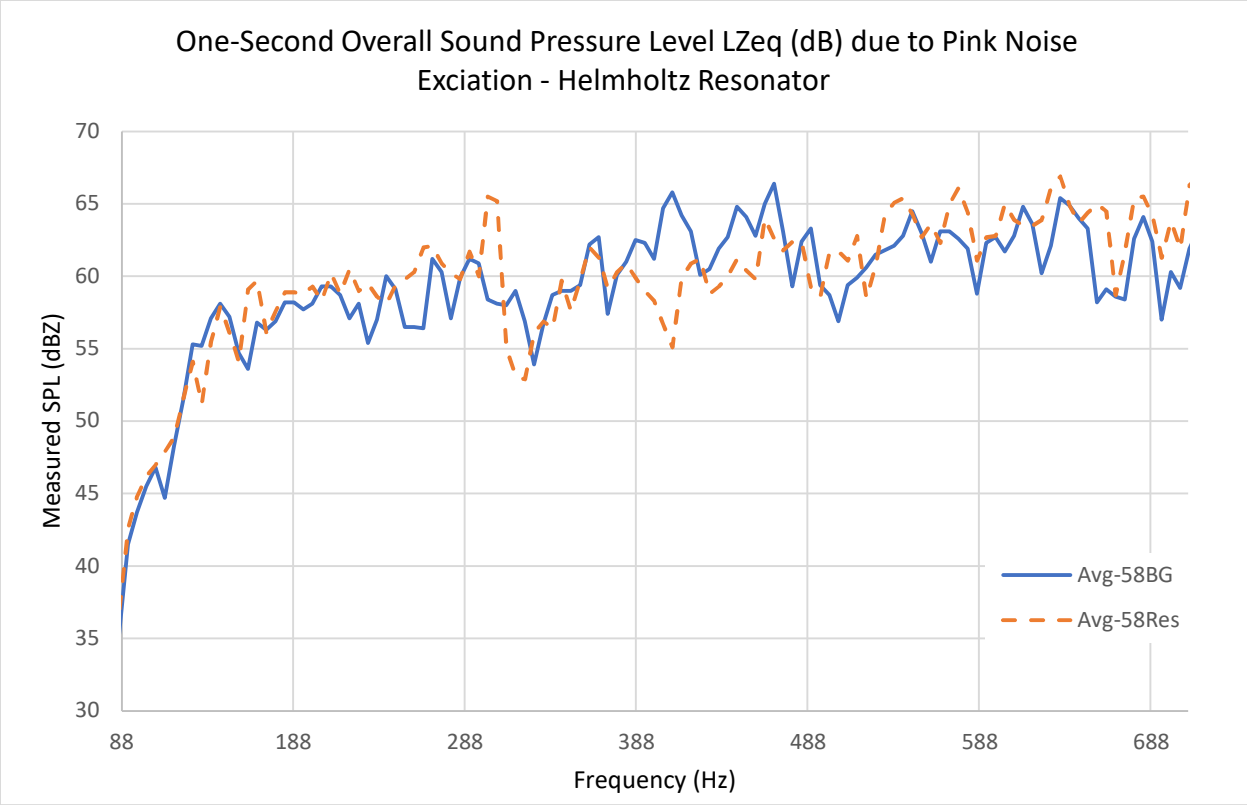

Figure 3.9. Graph showing the measured spectrum from pink noise excitation (58 dB) within the Helmholtz resonator without any resonator (or 'BG')

Having verified the resonant frequency of the spherical glass aperture (which is taken as 307 Hz) and having found that at the resonant frequency of the HR there is a rather consistent increase of 17-19 dB in SPL that is independent of the SPL of the pink noise, two tonal signals are generated and used to excite the spherical aperture at the identified resonant frequency of 307 Hz. The signals include one with an amplitude of 90 dB and the other 58 dB.

The experimental results with 90-dB tone are shown in Figure 3.10. The increase in SPL is 8 dB at 307 Hz, which is substantial. At the second harmonic or 614 Hz, the SPL is increased by 5 dB.

Figure 3.11 shows the experimental results with the 58-dB tonal signal. The increase in SPL is 9 dB at 307 Hz, also a substantial amount. However, there is little increase in SPL at 614 Hz. At the half-harmonic of 150 Hz, the increase in SPL is 7 dB. However, the SPL decreases by 2 dB at 460 Hz and by 1 dB at 662 Hz. Note that 460 Hz is a half-harmonic, while 662 Hz is a one-sixth harmonic.

Comparing Figures 3.10 and 3.11, the peaks at 307 and 614 Hz are both prominent, confirming fundamental harmonic at 307 Hz and second harmonic at 614 Hz. With a tonal signal of 90 dB, the difference in SPL is 10-20 dB at a quick glance between the HR and background. On the other hand, when the tonal signal is 58 dB, the gaps are smaller between the HR and background.

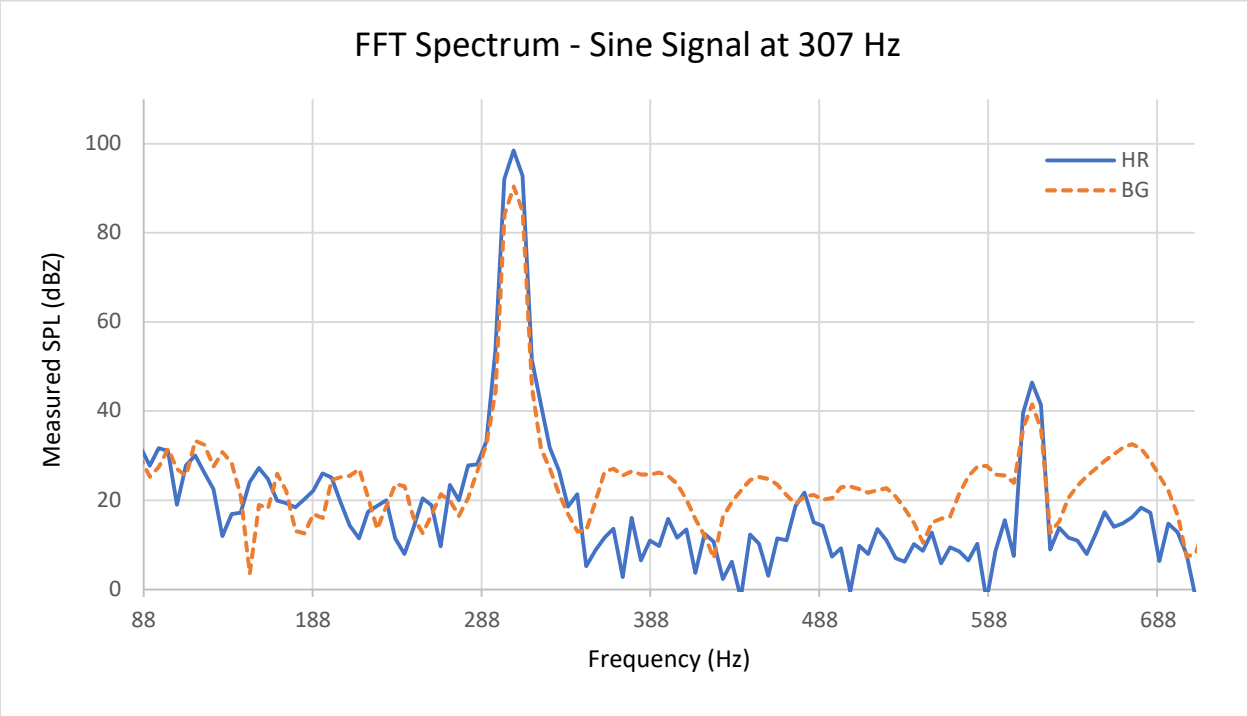

Figure 3.10. Graph showing the measured spectrum from tone at 307 Hz, SPL = 90 dB, within the Helmholtz resonator and without any resonator (or 'BG')

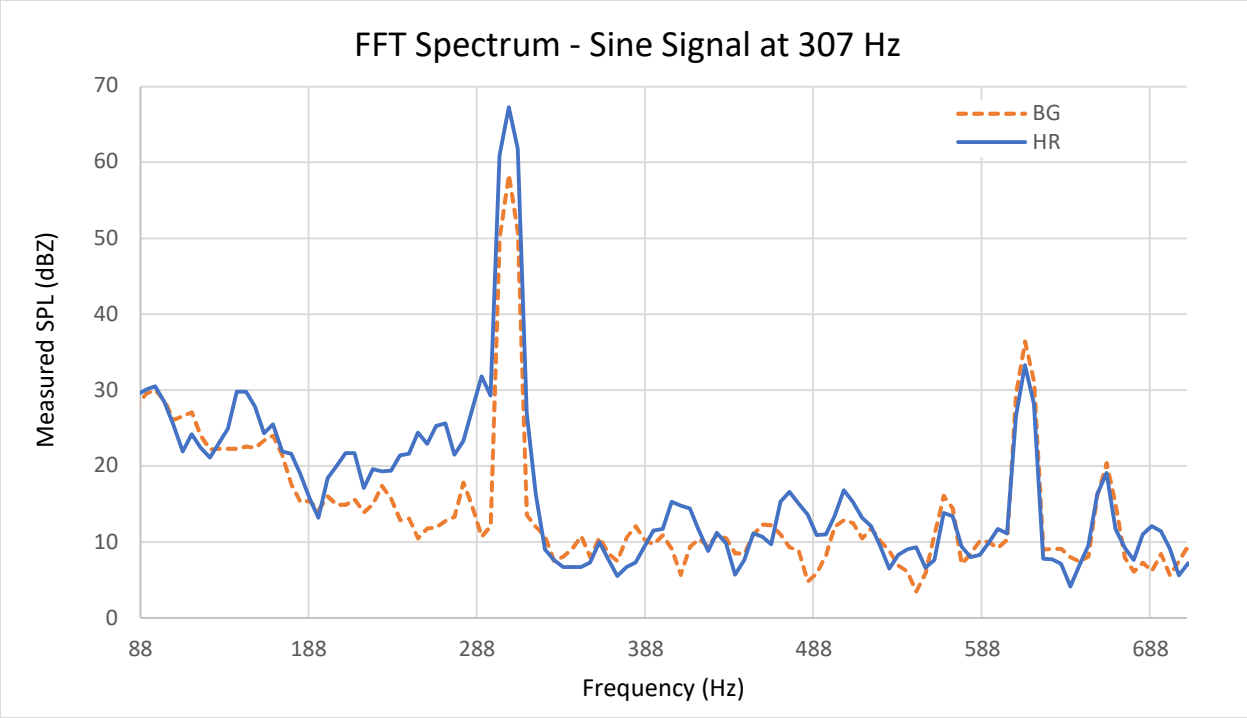

Figure 3.11. Graph showing the measured spectrum from tone at 307 Hz, SPL = 58 dB, within the Helmholtz resonator and without any resonator (or 'BG')

3.2.2 Rectangular Cavity Subject to Excitations

For this portion of the experiment, the excitations include a pink noise at 90 and 58 dB respectively, and a tonal signal of frequency 307 Hz and at 90 and 58 dB, respectively. Note that 307 Hz is the resonant frequency of HR. The methodology employed for HR is repeated, but with the HR being replaced by a rectangular cavity, as depicted in Figure 3.12. Figures 3.13 and 3.14 show the spectra of the cavity when subjected to pink noise at 90 and 58 dB, respectively. On the other hand, Figures 3.15 and 3.16 show the SPLs when subjected to tonal signals at 90 and 58 dB, respectively.

Figure 3.12. The rectangle cavity subject to pink noise and tonal signal from a loudspeaker as measured by a microphone.

As can be seen from Figure 3.13, when subject to a pink noise at 90 dB, the rectangular cavity increases the SPL of the background noise by 16 dB at 285 and 27 dB at 307 Hz. Note that 285 Hz is rather close to 274 Hz, the theoretical estimate of the resonant frequency of the cavity. The discrepancy between 274 and 285 Hz may be attributed to, (1) the rigid-walled

assumption in arriving at Equation (2.8) that gives the theoretical estimate of resonant frequencies; and (2) the location of the sound source (the experimental setup had the source on the outside of the cavity and near a corner of the cavity as shown in Figure 3.12; but [4] states that the source is located inside the cavity; on the other hand, other references [5-7] do not expressly include the conditions of source and receiver both being located inside the cavity). The SPL is also seen having peaks at 388 Hz (peak value = 68 dB), at 480 Hz (peak = 62 dB), at 576 Hz (peak = 75 dB), and at 609 Hz (peak = 72 dB). However, at 415 Hz, the SPL is decreased from the SPL of the background noise by 8 dB.

When subject to a pink noise of 58 dB (Figure 3.14), the rectangular cavity increases the SPL of the background noise by 12 dB at 269 Hz, by 4 dB at 285 Hz, and by 12 dB at 307 Hz. The SPL is also seen having peaks at 393 Hz (peak = 38 dB), at 480 Hz (peak = 41 dB), at 566 Hz (peak = 26 dB) and 689 Hz (peak = 30 dB).

The SPL levels are notably higher in the rectangular cavity, particularly at 307 Hz, highlighting the effect of modal resonance. This is evident when comparing the SPL measurements between the background noise and the rectangular cavity. Since the only difference between the background SPL and that of the rectangular cavity is the presence of the cavity itself, the observed difference can be attributed to the effects caused by the cavity.

Intuitively, one might expect the SPL within the rectangular cavity to be lower, as the cavity walls would typically block noise emissions from the loudspeaker placed outside. Additionally, the rectangular cavity walls have an absorption coefficient greater than zero, which should increase the total absorption in the test environment and, in theory, reduce the

overall noise level within the cavity. However, the modal resonance within the cavity interacts with the acoustic excitation, leading to significantly higher noise levels. This phenomenon, which is the focus of this thesis, demonstrates how modal resonances can occur at the cavity's corners, thereby increasing the SPL.

Thus, it may be stated based on the experimentation that the SPL within the rectangular cavity is not dominated by the direct field caused by the acoustic excitation from the loudspeaker. Instead, it is primarily influenced by the reverberant field within the cavity, which results from the coupling between the modal resonance and the frequency of the acoustic excitation.

Figures 3.15 and 3.16 show the SPL of the cavity when it is subject to a 307-Hz tonal excitation at 90 and 58 dB, respectively. It is shown that at 307 Hz and 90 dB (Figure 3.15), the rectangular cavity increases the SPL of the background noise by 20 dB. This 20 dB increase is substantial. Increases in SPL over the background noise are also seen at 275, 296, 334, 425, 705 and 662 Hz by 13, 19, 19, 17, 27 and 14 dB, respectively.

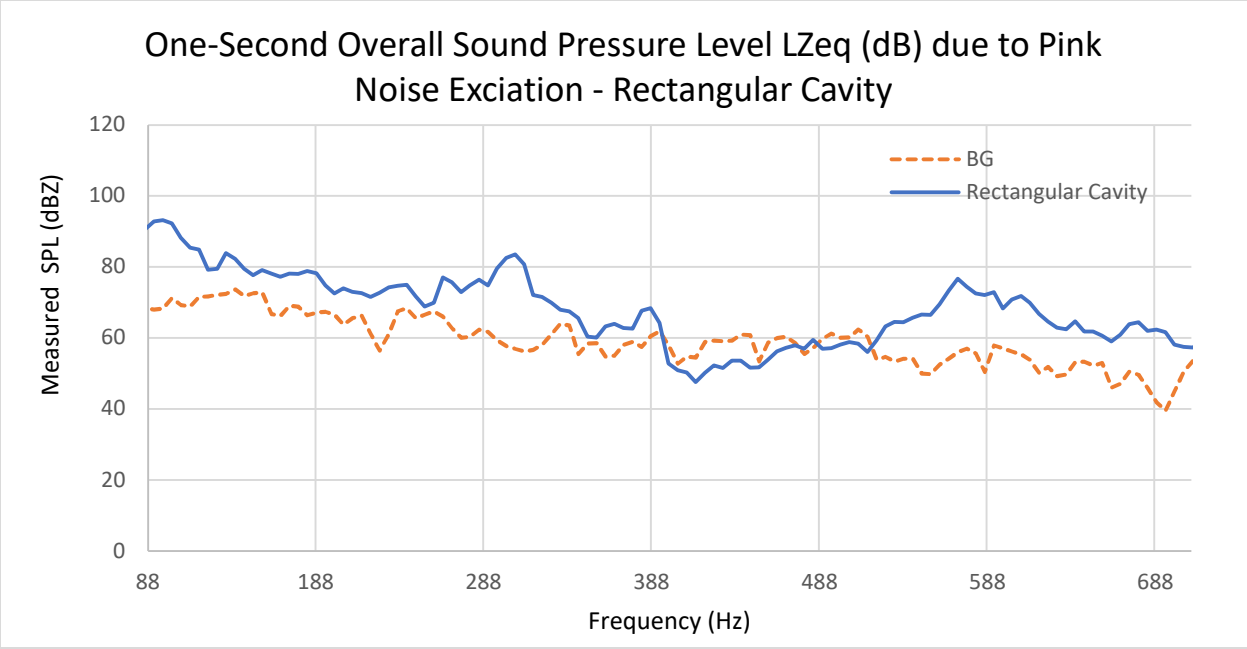

Figure 3.13. Graph showing the measured spectrum from pink noise excitation (90 dB) within the rectangular cavity and without any resonator (background labelled as 'BG')

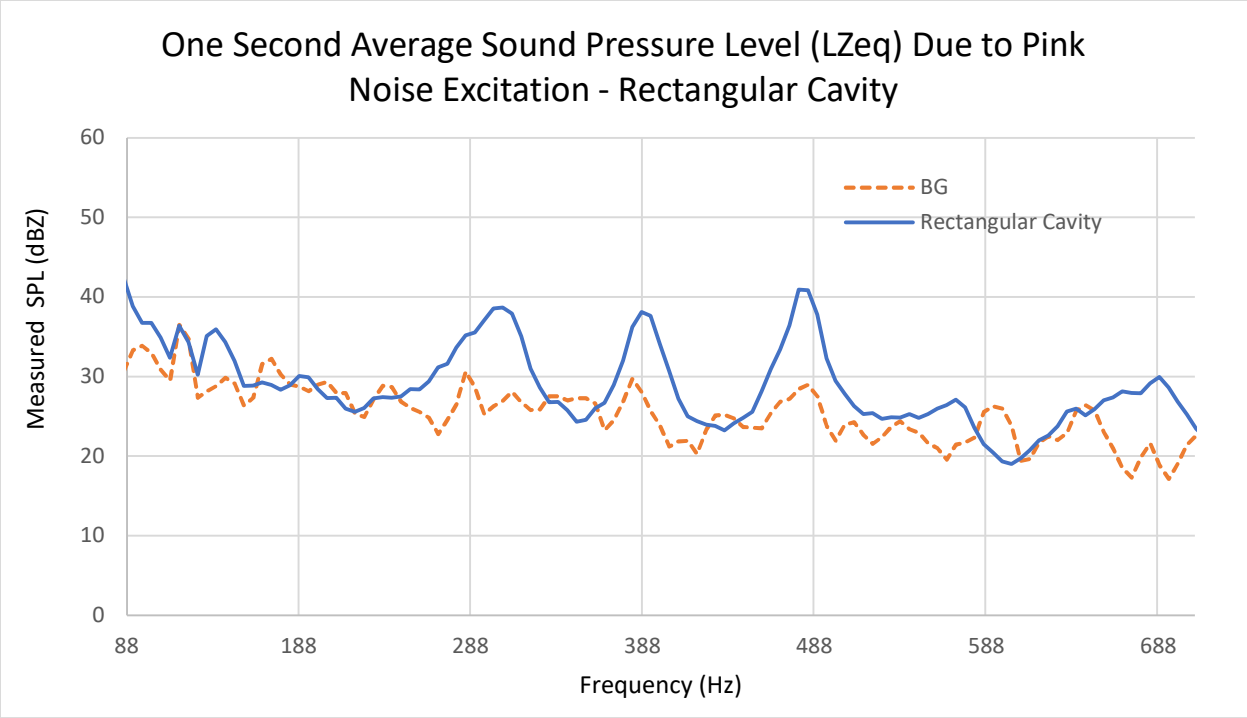

Figure 3.14. Graph showing the measured spectrum from pink noise excitation (58 dB) within the rectangular cavity and without the cavity (or 'BG')

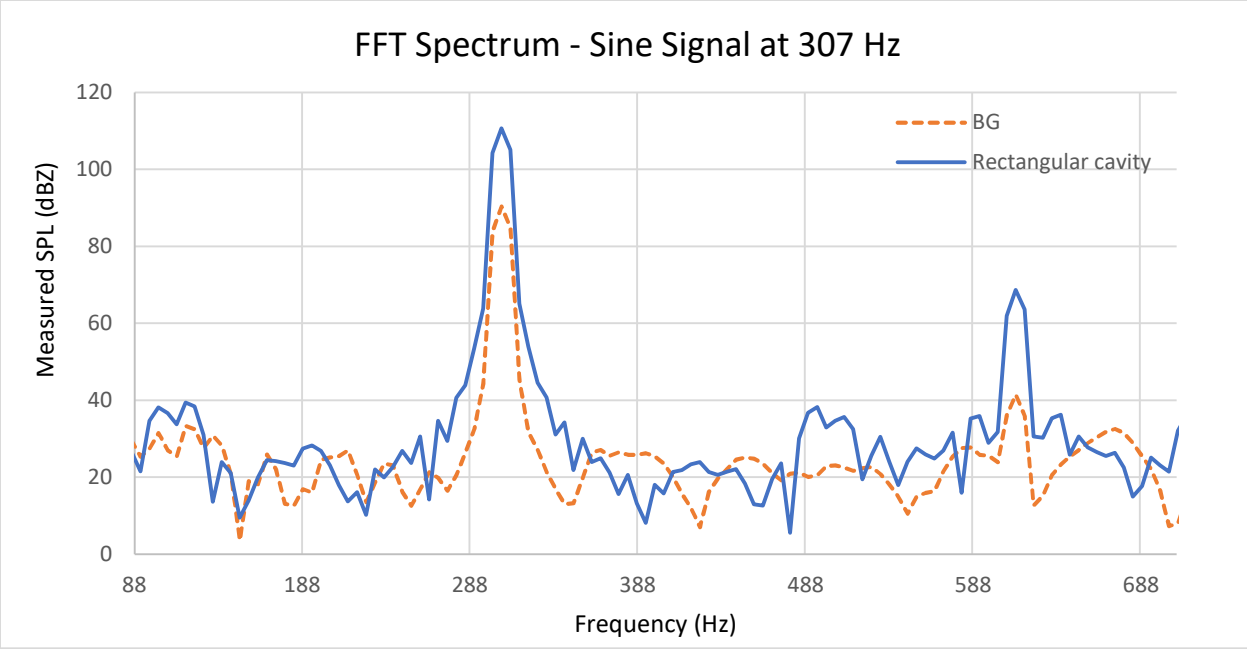

Figure 3.15. Graph showing the measured spectrum from tone at 307 Hz at 90 dB within the rectangular cavity.

At 307 Hz and 58 dB (Figure 3.16), the rectangular cavity increases the SPL of the background noise by 7 dB. Increases in SPL over the background noise are also seen at 264, 625 and 662 Hz by 6, 4, 15 dB, respectively. Interestingly, the increase in SPL at 285 HZ is negligible. This reconfirms that the resonant frequency is consistent with the already verified frequency of 307 Hz which is consistent with the experimental results so far.

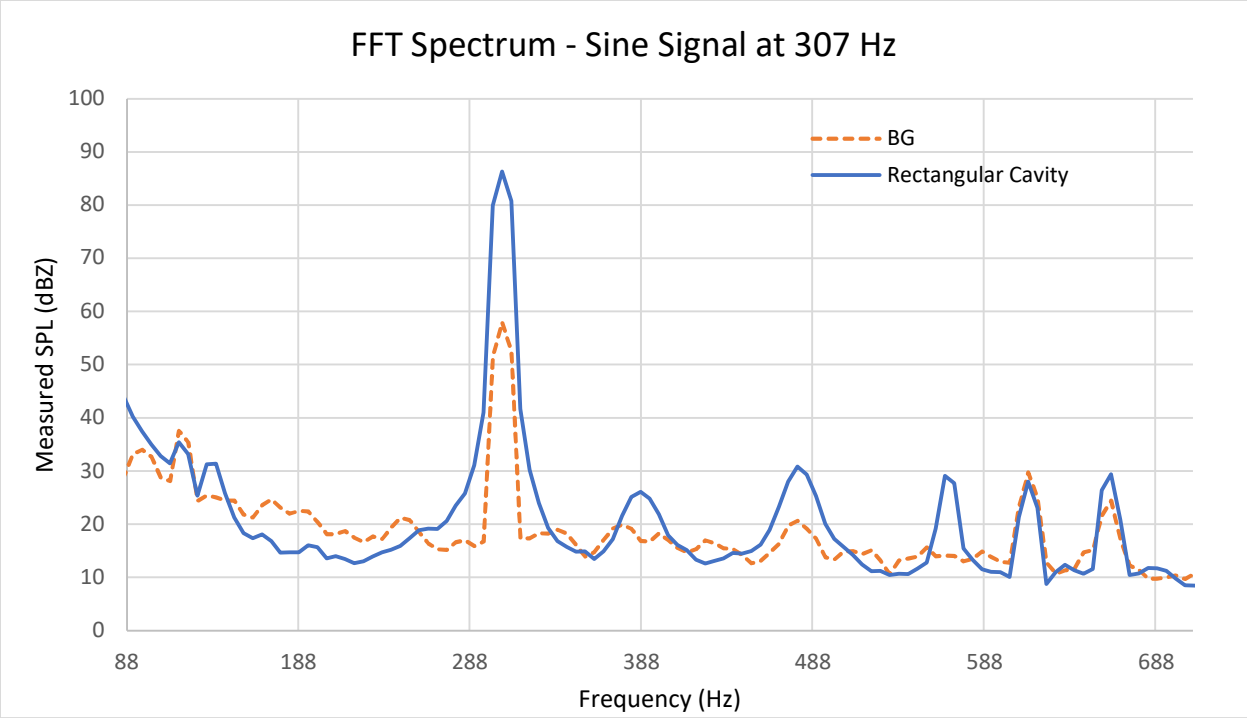

Figure 3.16. Graph showing the measured spectrum from tone at 307 Hz at 58 dB within the rectangular cavity.

3.2.3 The Coupled System Subject to Excitations

The coupled system refers to the HR being attached to the outside of the rectangular cavity, as displayed in Figure 3.17. The HR is positioned near a corner of the cavity, with the neck opening being glued to the top surface of the cavity. The same experimental routine is repeated using the pink noise and a tonal signal as excitation. Figures 3.18 and 3.19 illustrate the spectra of the coupled system under pink noise at 90 and 58 dB, respectively. On the other hand, Figures 3.20 and 3.21 present the spectra of the system when excited by a tonal signal of 307 Hz and at 90 and 58 dB, respectively.

Taking Figures 3.13 and 3.18, also 3.14 and 3.19 together, it is observed that,

1. When the excitation is at 90 dB (Figure 3.18), the coupled system reduces the SPL at 307 Hz by 5 dB, indicating that the system is capable of significant noise reduction at the target frequency. This is particularly important because the addition of the tuned HR to the rectangular cavity effectively attenuates noise caused by modal resonance within the reverberant field, a challenge that would have been difficult to achieve using conventional methods, such as adding absorption material to the walls, floor, and ceiling of the rectangular cavity.
2. When the excitation is pink noise of 90 dB (Figure 3.18), the coupled system increases the SPL over the background noise levels by 18 dB at 269 Hz and 21 dB at 274 Hz.
3. With a 58-dB pink noise excitation and compared with background noise only (Figure 3.19), the coupled system reduces the SPL at 307 Hz by 5 dB, indicating that the system is capable of significant noise reduction at the target frequency, consistently.
4. With a 58-dB pink noise excitation and compared with background noise only (Figure 3.19), having the HR coupled with the rectangular cavity increases the SPL by 16 dB at 269 Hz, 12 dB at 393 Hz, 13 dB at 479 Hz and 8 dB at 566 Hz. At 285 Hz, the SPL decreases by 4 dB.

Figure 3.20 shows the spectrum of the coupled system when subject to a tonal signal at 307 Hz and 90 dB. Examining Figures 3.13 and 3.20, it is seen that at 307 Hz, the coupled system decreases the SPL by at least 5 dB.

Figure 3.21 shows the spectrum of the coupled system when subject to a tonal signal at 307 Hz and 58 dB. Examining Figures 3.14 and 3.21, it is seen that at 307 Hz, the coupled system decreases the SPL by at least 5 dB.

Figure 3.17. The coupled system subject to pink noise and tonal signal from a loudspeaker as measured by a microphone.

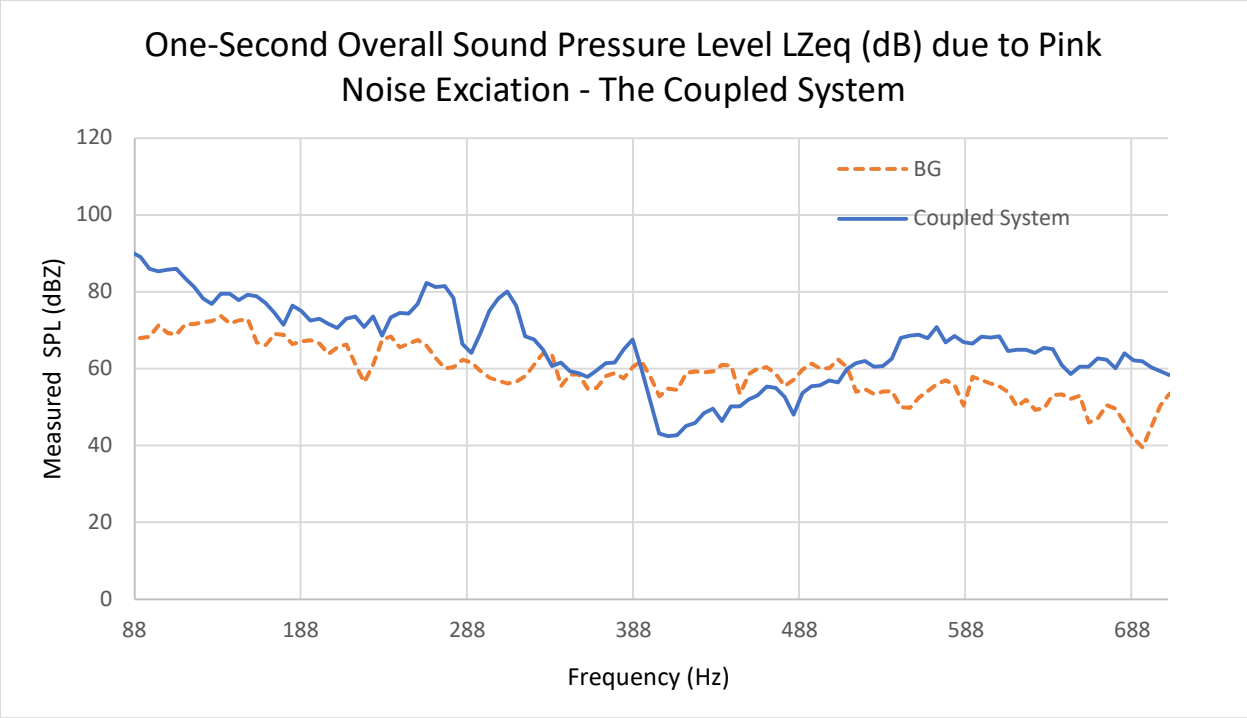

Figure 3.18. Graph showing the measured spectrum from pink noise excitation (90 dB) within the coupled system.

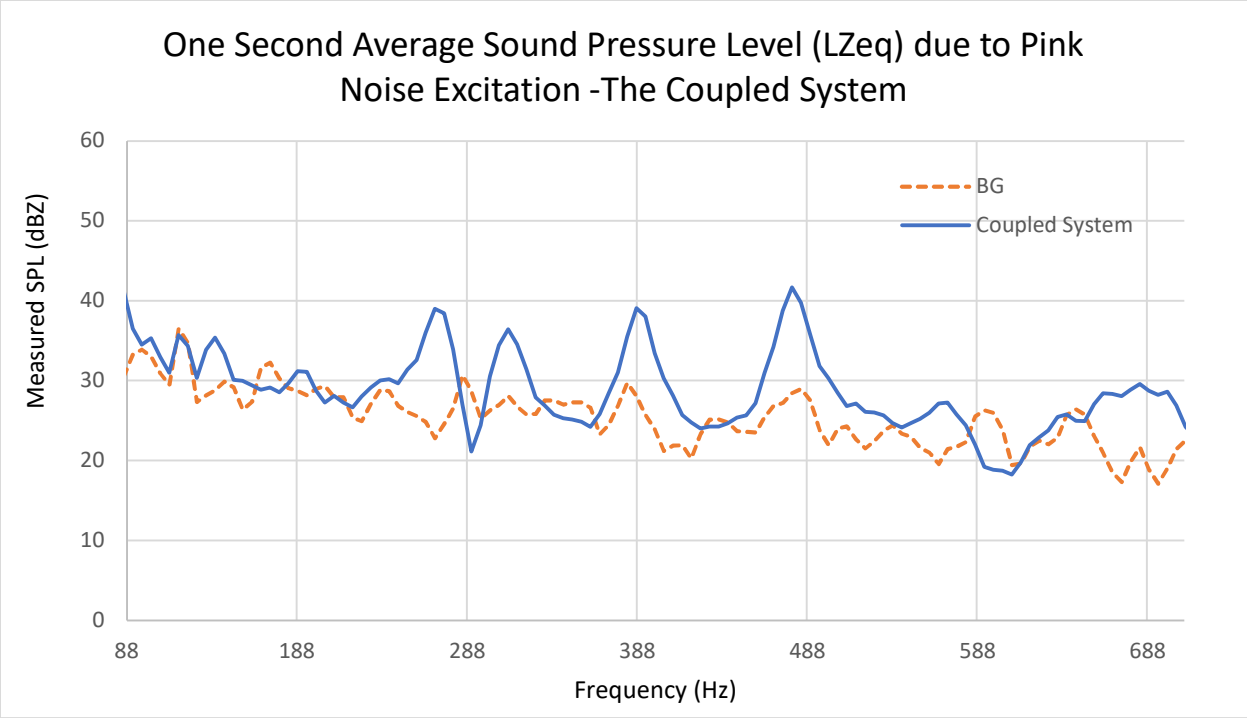

Figure 3.19. Graph showing the measured spectrum from pink noise excitation (58 dB) within the coupled system.

Figure 3.20 shows the spectrum of the coupled system when subject to a tonal signal at 307 Hz and 100 dB. Examining Figures 3.13 and 3.20, it is seen that at 307 Hz, the rectangular cavity by itself increases the SPL to 112.5 dB, but the coupled system experiences only an increase to 92.9 dB. The difference is 19.6 dB between the two setups.

Figure 3.21 shows the spectrum of the coupled system when subject to a tonal signal at 307 Hz and 58 dB. Examining Figures 3.14 and 3.21, it is seen that at 307 Hz, the cavity by itself increases the SPL to 86 dB, but the coupled system sees only an increase to 81 dB. The difference is 5 dB between the setups.

Moreover, comparing Figures 3.10 and 3.20 (when subject to a tonal signal of 100 dB at 307 Hz), the coupled system sees increases in SPL at half-harmonics of 154 and 460 Hz (by 13.1 and 17.8 dB, respectively, over the SPL with HR only). However, at 307 and 614 Hz, the SPL is decreased by 33.5 and 13 dB, respectively.

Next comparing Figure 3.11 and 3.21 (subject to a tonal signal of 58 dB at 307 Hz), the coupled system sees increases in SPL at 307 and 662 Hz by 13.7 and 9.9 dB, respectively, over the SPL with HR only. On the other hand, at 150 and 614 Hz, the SPL decreases by 10 and 5.4 dB, respectively.

Overall, it seems that whether the 307-Hz tonal signal is with higher (100 dB) or lower (58 dB) amplitude, there are certain frequencies at which the coupled system responds with increased SPL over the SPL with HR only. The opposite is also true. However, such frequencies (at which the coupled system increases or decreases SPL over that with HR only) are signal-amplitude dependent. Similar observations can be made when the excitation becomes a pink noise.

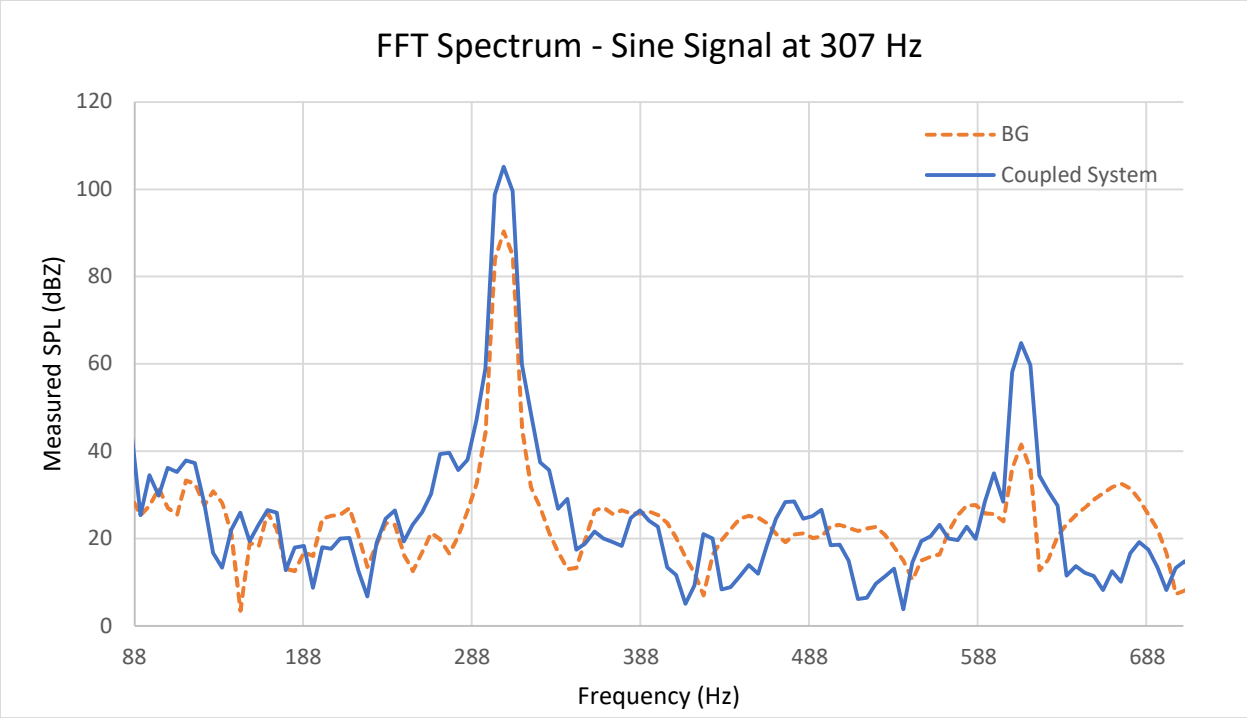

Figure 3.20. Graph showing the measured spectrum from tone at 307 Hz at 90 dB within the coupled system.

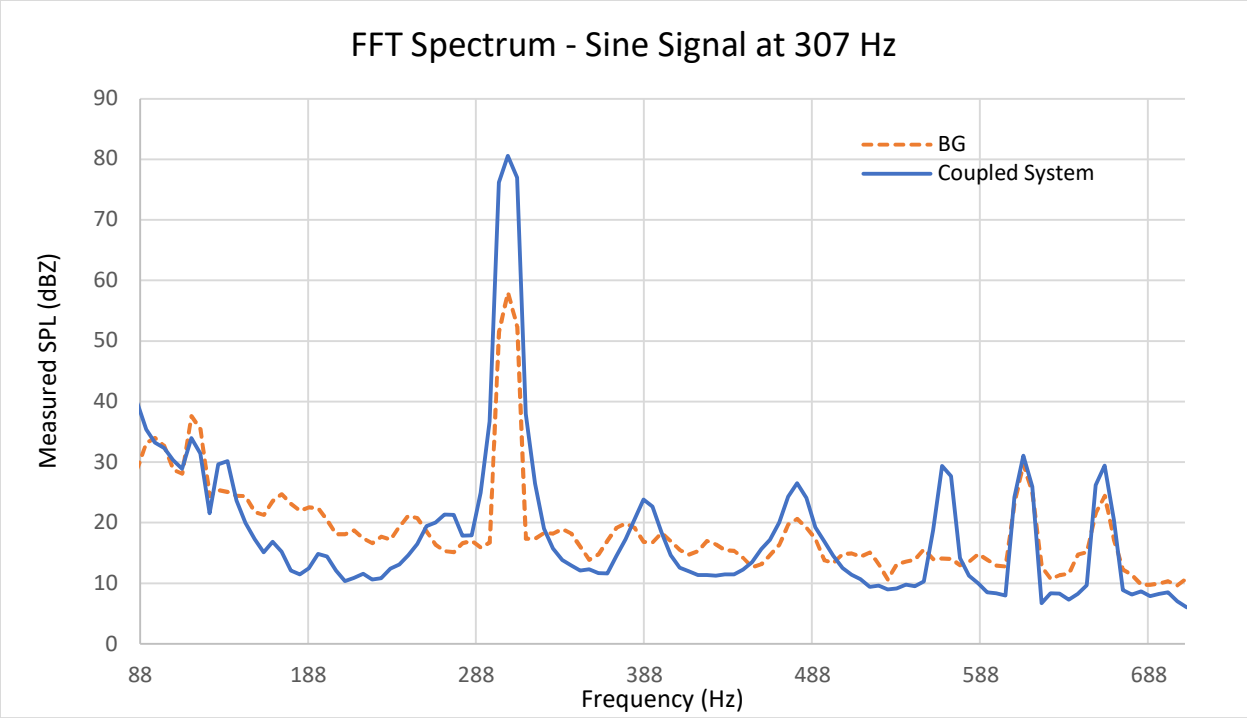

Figure 3.21. Graph showing the measured spectrum from tone at 307 Hz at 58 dB within the coupled system.

3.2.4 Energy Harvesting by HR and Coupled System

A piezoelectric beam is utilized to demonstrate the energy harvesting capacities of the HR and coupled system. As portraited by Figure 3.22, the beam is clamped at one end from a stand, while the piezoelectric is clipped to the free end of the beam. A slit is made within the spherical glass neck area so that the HR houses the piezoelectric (Figure 3.23). When the system is subjected to acoustical excitation, voltage signal in the piezoelectric is measured using the calibrated handheld Haneke oscilloscope.

Figure 3.24 shows that a voltage of 327 mV AC is harvested by the HR when excited by a 90 dB sinusoidal tone at 307 Hz. It should be noted that the 327 mV is the RMS (root-mean-

squared) value of the measured voltage signal. Next, the HR and piezoelectric beam is placed at a corner of the rectangular cavity. A tonal signal (307 Hz and 100 dB) is employed as the excitation. Figure 3.25 shows that an average of 200 mV AC is harvested using the coupled system excited by a 90 dB sinusoidal tone at 307 Hz.

In summary, the coupled system has demonstrated its ability to attenuate the SPL by 21 dB (relative to the background) and harvest 200 mV AC electricity when subjected to tonal excitation at 307 Hz and 90 dB. The 307 Hz represents the common tuned resonant frequency of both the HR and the rectangular cavity. Thus, the system is capable of significantly reducing noise while simultaneously harvesting energy for potential applications. The stand-alone HR system was able to harvest 127 mV AC more than the coupled system when subjected to the same excitation SPL. This is because, when used in an open system, the HR system primarily amplifies the acoustic excitation SPL at its tuned resonant frequency. In contrast, in a closed system like the tuned coupled system, the coupling effect attenuates the rectangular cavity modal resonance, resulting in less energy harvested. This observation, consistent with SPL measurements, further demonstrates that the coupled system attenuates energy, as evidenced by the reduced voltage harvested by the piezoelectric harvester compared to the HR system. Additionally, it highlights the coupled system's ability to simultaneously harvest energy. Attempts were made to demonstrate the energy harvesting capabilities of the coupled system at a lower SPL than 58 dB. However, due to limitations in the oscilloscope's sensitivity, the harvested energy was omitted from this thesis. More sensitive instrumentation and an improved energy harvester could prove beneficial if energy harvesting at such low SPLs is desired.

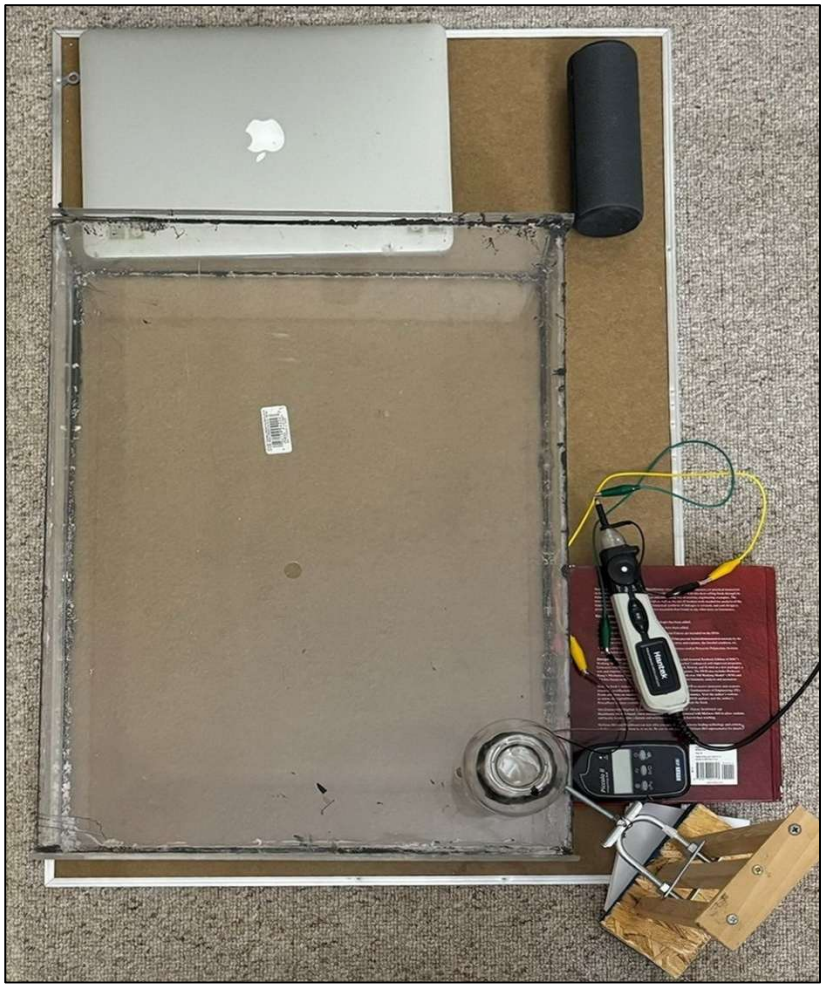

Figure 3.22. Piezo inside the Helmholtz resonator.

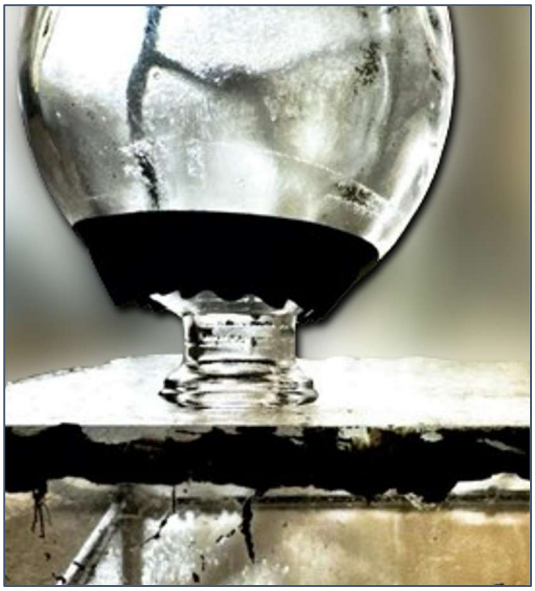

Figure 3.23. Helmholtz resonator with a slit at the neck to house the piezo beam's free end.

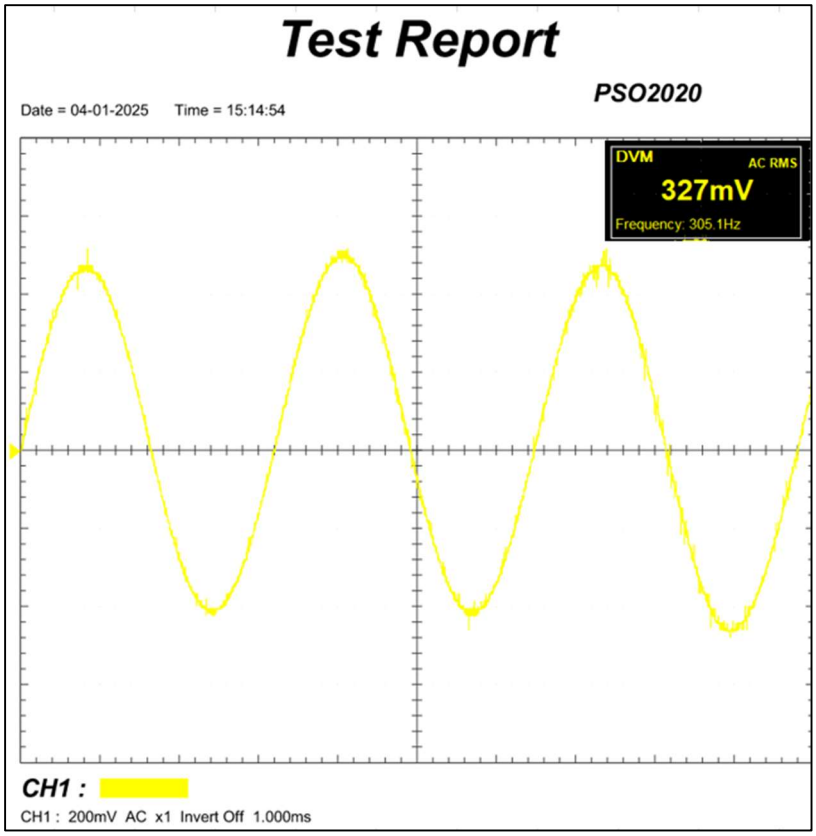

Figure 3.24. Voltage measurement at Helmholtz resonator neck using a cantilever piezoelectric beam at 90 dB of tonal excitation at 307 Hz.

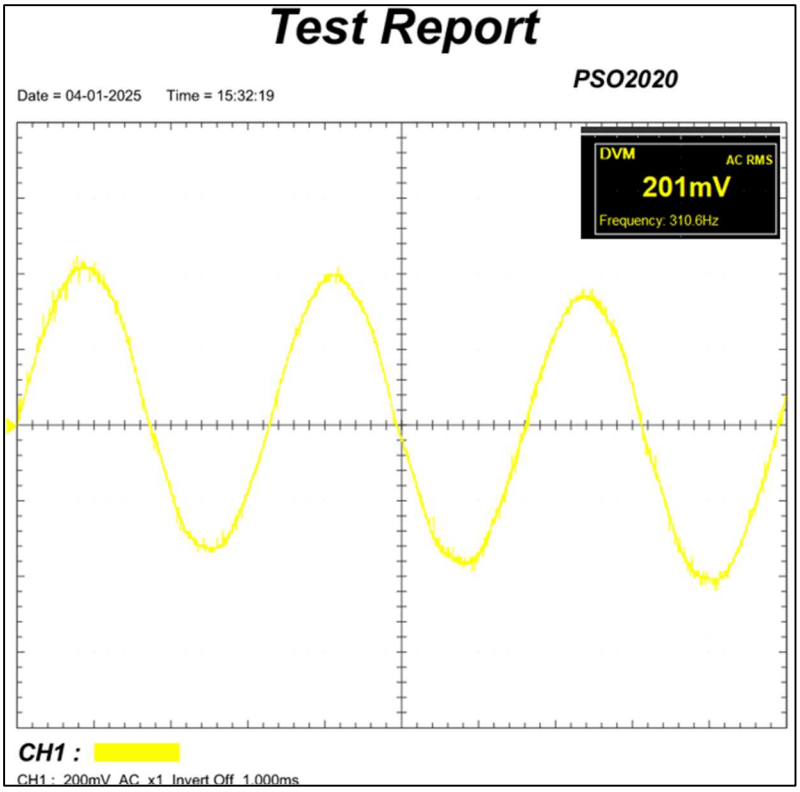

Figure 3.25. Voltage measurement within the coupled system using a cantilever piezoelectric beam at 90 dB of tonal excitation at 307 Hz

Finally, it should be mentioned that several variants of the spherical aperture were experimented with, using the same routine (excited by pink noise, then by a tonal signal). The variants included different placements of the slit cut into the glass aperture, for example, slits in the bottom and middle of the cavity. It has been observed that the neck slit as shown in Figure 3.23 proved to be more suitable for energy harvesting because the length of the piezo beam spans the diameter of the neck.

3.3 Concluding Remarks

The main findings of the experimental work are,

1. The resonant frequency of the HR was found to be near or at 307 Hz which was close to the theoretical estimate of 296 Hz.
2. The lowest natural frequency of the rectangular cavity was found to be near 285 Hz. The theoretical estimate, with the boundary conditions being rigid walls all around, was 274 Hz.
3. Although the resonant frequency of the HR system may not precisely align with the rectangular cavity in the system, the coupled system's frequency response exhibits a measurable and noticeable coupling effect. This demonstrates that the HR system modulates and attenuates the peak within the tuned resonant frequency range, particularly near the rectangular cavity corners where the peak SPL is expected.
4. For the stand-alone HR subject to pink noise, a rather consistent increase in SPL at 307 Hz was observed. This increase of 17-19 dB seemed to be independent of the SPL of the excitation.
5. The increase in SPL in the HR under tonal excitation was 8-9 dB, a smaller increase but significant still.
6. The rectangular cavity demonstrated an average increase of 15 dB at 307 Hz when subject to pink noise.
7. The increase in the cavity's SPL was 20 and 7 dB when the excitation was a 307-Hz tonal signal of 90 and 58 dB, respectively.

8. Under pink noise excitation, the coupled system showed a decrease of 5 dB in SPL at 307 Hz as compared to the rectangular cavity system.
9. The coupled system demonstrated a decrease of, also 5 dB, at 307 Hz when subject to tonal signals (307 Hz, 90 and 58 dB).
10. A voltage of 327 mV AC was harvested from the HR-piezoelectric setup when excited at 307 Hz with 90 dB.
11. The HR-rectangular cavity-piezoelectric system harvested 200 mV AC when excited at 307 Hz with 90 dB.
12. The HR was successfully tuned to align with the rectangular cavity, both systems achieving a common resonance frequency of 307 Hz. This demonstrates that the experimental results were effectively applied to construct and test the coupled resonating system. While this tuning process was challenging and iterative, particularly given the discrepancies between the theoretical and experimental outcomes, the experimental approach proved invaluable in advancing the analysis. It was crucial for tuning two resonating systems with distinct geometries.
13. Although the rectangular cavity exhibits SPL peaks at various frequencies, the focus was on examining the effect of adding the HR to the cavity, specifically in terms of its combined noise reduction and energy harvesting capabilities.

Tuning the HR to match the resonance frequency of the rectangular cavity, while the HR exhibits a relatively narrow frequency range, was significant, made possible by iterative experimentation. Relying solely on theoretical predictions could have hindered progress;

therefore, numerous experiments were conducted to ensure both the HR and rectangular cavity consistently resonated at the same frequency within the targeted range.

It can be concluded that, to effectively harvest energy and attenuate noise, the coupled system should be excited at 307 Hz. However, the system shows greater tonal noise reduction at 285, 291, and 296 Hz. Since the study focuses on simultaneous noise reduction and energy harvesting, 307 Hz was chosen as the optimal excitation frequency. For maximum noise reduction, the system performs best at 291 Hz, even though the HR's resonant frequency is designed for 307 Hz. The resonant frequency of the HR was found to be near or at 307 Hz which was close to the theoretical estimate of 296 Hz.

Chapter 4 - ANSYS® Simulation of Base Models

This chapter will present the simulation methodology and findings by using ANSYS® Student 2024 R2 software and related to the behaviors of the rectangular cavity, and the coupled system consisting of the Helmholtz Resonator (HR) and the rectangular cavity which have previously been used in the physical experimentation setup. Collectively they are known as the base models in this thesis. The chapter is organized as follows: Section 4.1 outlines the simulation methodology; Section 4.2 discusses simulation results and their associated analyses; Section 4.2 is further subdivided into four sub-sections: Section 4.2.1 focuses on the simulation of the rectangular cavity subjected to excitations and its calibration with the physical experimentation results; Section 4.2.2 investigates the simulation of the rectangular cavity under excitation using additional probing points; Section 4.2.3 investigates the simulation results of the coupled system under excitation; and Section 4.2.4 explores energy harvesting capabilities of the coupled system using the comparison of SPL within various probing points within the HR. Finally, Section 4.3 provides a summary of the key findings.

The principal objective of this chapter is to develop a computational model with the ANSYS® software. The simulation environment, once calibrated, would become representative of the physical experimentation setup, including the rectangular cavity and the coupled system. The simulation facilitates achieving the following objectives:

1. Calibrating a computational model based on physical experimentation methodology and apparatus.

2. Studying the various components of the physical apparatus in more detail.

3. Investigating possible reasons for discrepancies and their implications; and

4. Preparing a calibrated model for optimization and future work.

4.1 Simulation Methodology

The overall simulation process involves the following workflow, as depicted by Figure 4.1:

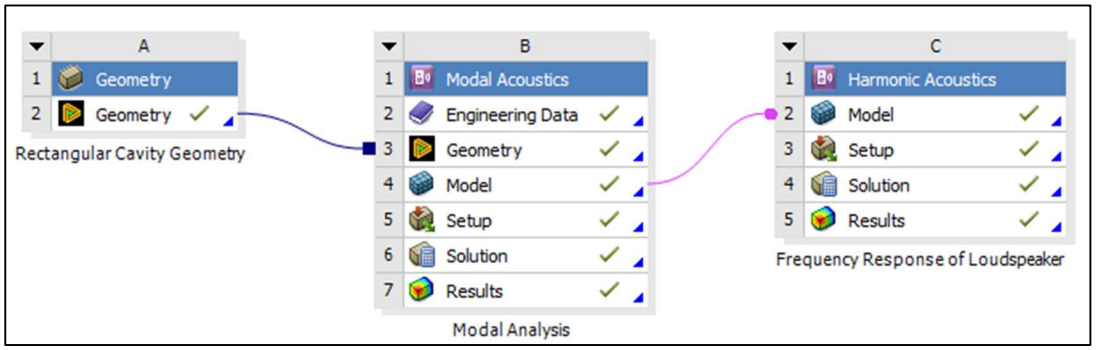

Figure 4.1. Typical workflow in ANSYS® Student 2024 R2 software

The key factors in progressing the simulations through the workflow of Figure 4.1 are:

1. Developing geometry using the dimensions which were used for the physical model in the *DesignModeler* or *SpaceClaim* Module. (Hereinafter, terms unique to ANSYS® Student 2024 R2 software will be in the italic font).

2. Importing the geometry into the *Modal Acoustics Module* to mesh (discretize) the continuous domain of the model and perform modal analysis to determine the overall acoustical modes; and,

3. Acoustically exciting the system uses a point source loudspeaker within the *Harmonic Acoustics Module* to study the frequency response of the system under excitation.

Meshing, in ANSYS® as well as other finite element analysis software, is the discretization of the geometry which is used in simulations. It divides the model geometry from a continuous domain into smaller, finite-sized elements which facilitate numerical computation of the results. Each element has nodes where the variables (or the unknowns) are solved.

Mesh density can affect the accuracy of the overall results. ANSYS® acoustical solver uses the wavelength to progress the computation of the discretized domain. Therefore, it is vital to realize that as the upper end of the frequency range increases, the need for a higher number of meshed elements in a model increases exponentially, which would demand greater computational resources and time to solve [1]. A general rule is to allow for a minimum of 6 elements per wavelength for quadratic elements, or 12 elements per wavelength for linear elements would be desirable, however an increase mesh density is more desirable at junctions of surfaces [2]. For example, at the target frequency range between 100 and 500 Hz, the shortest wavelength would be [3] $\lambda = (343.6 \text{ m/s}) / (500 \text{ Hz}) = 0.69$ m, therefore it would require at least 18 elements per meter of the geometric model (12 elements per wavelength / 0.69 m = 17.4 elements per meter). After convergence test (see next paragraph), the mesh size of 20 elements per meter is chosen, as it exceeds the requirement of 18 elements per meter in each direction to give better accuracy in the simulations. Other factors such as mean flow could also be incorporated into the model, but a reasonable assumption is that since the physical experimentation did not include any significant airflow (such as high velocity duct flow,

turbulence, etc.), simulation modeling would exclude the effects of air flow. This assumption is also consistent with the research focus of this thesis, the acoustical responses of the rectangular cavity and the coupled system. To study any aeroacoustics phenomenon, Computational Fluid Dynamic (CFD) software to analyze the problem would be more suitable which falls outside the scope of the current research.

A mesh convergence study was conducted to ensure the accuracy and reliability of the simulation results at the target frequency of 307 Hz. The convergence criterion was that the variation of the computed sound pressure level (SPL) at a representative location within the rectangular cavity became indiscernible, as the mesh was progressively refined. The results of the convergence study were presented in the Appendix. These results demonstrate that a mesh size of 0.055 m or finer is sufficient for obtaining stable and accurate SPL values in the harmonic acoustics analysis of this system. The 0.05 m mesh (or 20 elements per meter) was subsequently selected as the baseline for all subsequent simulations to balance computational efficiency with numerical accuracy.

Overall, 1404 elements (FLUID220, a 3D second order Hex20/Brick element) were used for the mesh with 6828 nodes. A typical meshed domain for the rectangular cavity is shown in Figure 4.2 where the numbers of elements used are 9, 12 and 13 elements along the width, height, and length, respectively; or 19, 99, and 20 elements per meter along the width, height, and length, respectively.

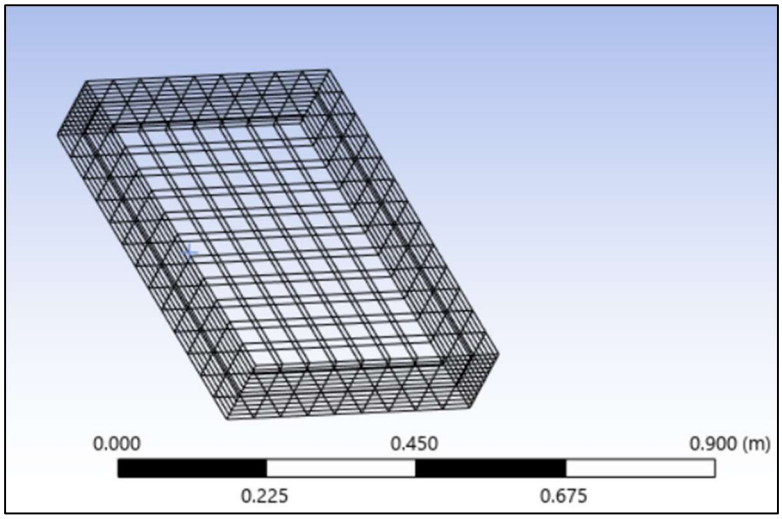

Figure 4.2. A typical mesh of the rectangular cavity in ANSYS® Modal Acoustics Module

Boundary conditions define how the model interacts with its surroundings and govern how sound waves behave at the boundaries of the domain. Proper application of boundary conditions is critical for accurate acoustical simulations.

Rigid-wall conditions at boundaries are used for all the walls in the rectangular cavity, and the walls plus the geometric boundaries of the spherical HR for the coupled system. This means that the computational model assumes that the sound waves will be contained inside the walls for the model of rectangular cavity only, and inside the walls as well as the geometric boundaries of the spherical HR for the model of the coupled system. The rigid-wall boundary condition simplifies the modeling process. However, the surfaces of the physical model are made of acrylic (or Plexiglas) and glass and therefore do not have infinite rigidity. As a result, sound waves will interact with the walls and geometric boundaries, modulating the acoustic responses within the enclosure, and the mode shapes and resonance frequencies within the system, leading to fluid-structure interaction (FSI). FSI is beyond the scope of the thesis because

it requires substantial computer resources to explore. Careful consideration was made at the beginning of the research to use materials as rigid as feasible and to select geometries requiring limited connections, adjoining surfaces, and to avoid flimsy construction. Therefore, the glass was selected for the spherical aperture which came with the single-piece construction. Thick acrylic sheets were used to construct the rectangular cavity. While a simpler acoustic model could be constructed by assuming rigid-walls for a lighter weight acoustical system (such as one constructed from lightweight sheet metal), the flexible walls when subjected to high levels of sound pressure could radiate off sound which would further reduce the effectiveness of the rigid wall assumption [4]. While there is a trade-off between minimizing simulation errors and computational resources, such as selecting to use a simpler acoustic model with using rigid-wall conditions during our simulations versus using a more complex modeling scheme which would incorporate materials flexibility, which subsequently would require more resource allocation (such as software licensing, computational cost, modelling time), every effort was made to ensure that the physical system would reflect such conditions as much as practicable.

Probing points of SPL and frequency are specific locations within the simulation domain where acoustic variables, such as pressure fluctuations and sound wave behavior, are analyzed. These points play a critical role in validating the model against experimental data and understanding sound propagation within the system. In ANSYS®, the acoustic SPL results are determined at discrete locations. In contrast, the physical model used an omnidirectional microphone to measure acoustic pressure, which provided a more global representation of the sound pressure level. In identifying the probing points in ANSYS®, *Named Selections* were used

to assign a probing point to a particular node which would reflect the vicinity at which the physical acoustic pressures were conducted in the physical experiments. Figure 4.3 depicts the node which was selected (Node ID 1270) as a modelling receptor probing point for the evaluation of the sound pressure level and frequency response in ANSYS®.

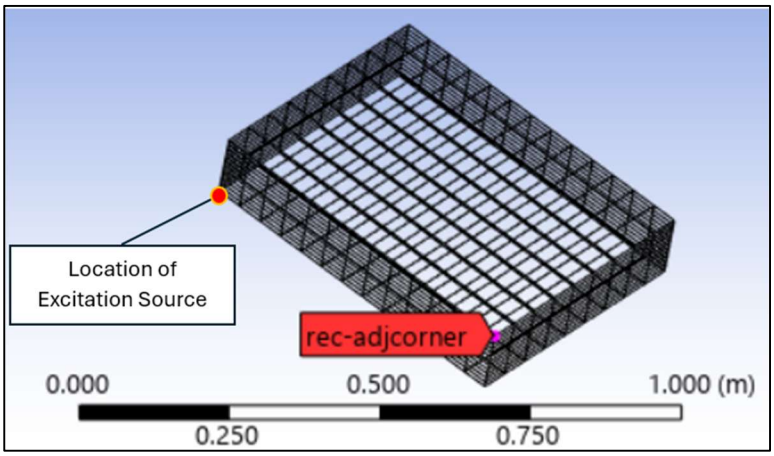

Figure 4.3. A probing point near the rectangular cavity corner in ANSYS®

The *Acoustic Region* in an ANSYS® model is used to assign acoustical properties to various geometries, such as the rectangular enclosure and the spherical Helmholtz resonator, for simulation purposes. Initially, these geometries are assigned to material, such as air, but are still treated as structural elements. To enable acoustical simulation, all bodies in the model are then designated as part of the *Acoustic Region*. This transformation converts the selected structural elements into acoustic domains, which are subsequently meshed with *Acoustic Elements*.

Mass Source in ANSYS® models is used to replicate the excitation by the loudspeaker which is suitable for harmonic analysis [5]. In the model used in this thesis the mass source was

assigned to a vertex (Figure 4.4) which was representative of the point source simplification of the physical loudspeaker which was used during physical experimentation. The unit for a *Mass Source* in ANSYS® is kg/s which resembles the mass flow rate unit for fluid flow.

The effects of the material used to construct the model were previously discussed in terms of selecting the appropriate boundary conditions. Another significant implication of the material is the absorption that it introduces into the system.

Absorption Surfaces were used to assign per-octave absorption coefficients to different materials, such as glass or acrylic. Intuitively, an empty room made of reflective surfaces, such as concrete, would have lower sound absorption properties (commonly referred to as a 'live room'), leading to a higher likelihood of sound buildup within space. In contrast, an occupied room with thick carpets, fabric curtains, and gypsum wallboards would exhibit higher sound absorption properties, attenuating sound buildup more effectively. This variation in abortion can affect the overall sound pressure level with an enclosure such as the rectangular cavity. This effect was added into the ANSYS® model for a more accurate representation within the simulation environment.

The speed of sound was set to 343.6 m/s within the *Engineering Data* tab. Within the *Model* tab, air was assigned to the continuous domain. The geometry of the rectangular cavity was developed using the physical models' dimensions: (L_x, L_y, L_z) = (626.5, 472.5, 120.5) mm. Next, the cavity was meshed as outlined above. The mass source was placed within one corner and the simulation was run using the rigid wall boundary condition and the surface absorption values for glass and acrylic. The surface absorption for glass and acrylic is selected from the

available literature [6]. For acrylic, specific absorption coefficient data are not as readily available in open literature as glass. However, it is generally recognized that acrylic, being a non-porous and rigid material, exhibits low sound absorption properties, like glass.

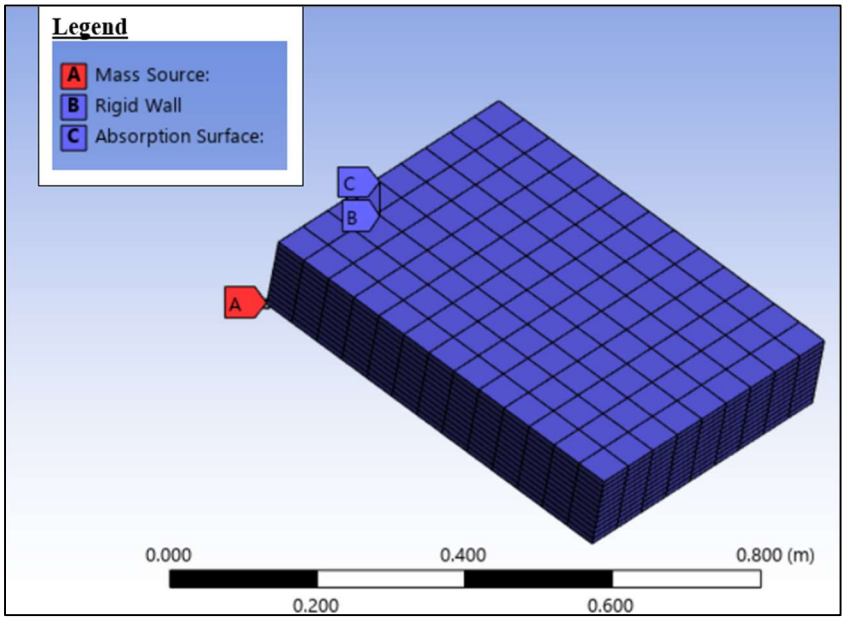

Figure 4.4. The rectangular cavity in ANSYS® with the mass source, rigid wall boundaries, and the absorption surface areas

Finally, due to limitations with ANSYS® Student 2024 R2, it is not possible to study the frequency response spectrum beyond 500 Hz without having access to a full license. However, the primary focus of the analysis in this thesis is within the frequency range of 88 to 500 Hz.

4.2 Simulation Results and Discussions

4.2.1 ANSYS® Simulated Rectangular Cavity Subject to Excitations Calibration

The simulation setup for the rectangular cavity is shown in Figure 4.4. A constant sound signal was generated using the ANSYS® *Mass Source Signal* at an arbitrary value of 0.3×10^{-6} kg/s and the sound pressure results were computed at the probing point (Figure 4.3). The preliminary results showed an exceptional agreement in terms of the locations of the resonant peaks with those of the physical experimentation results illustrated in Figure 3.14, particularly at the most dominant peak frequency of 480 Hz. However, the values of the SPLs were significantly higher. Through iterations of different values for the mass source signal, a constant value of 0.19×10^{-6} kg/s was found to reflect the physical model's loudspeaker's sound power level more accurately. Additionally, it is also noted that the results calculated by ANSYS® should be 3 dB lower than those from physical experimentation [7]. In the following, all simulated results are from a mass source signal at 0.19×10^{-6} kg/s.

The results of the frequency response from the ANSYS® simulations and its comparison with the physical experimentation results from pink noise excitation at 58 dB within the rectangular cavity is shown in Figure 4.5. As can be seen from Figure 4.5, the simulated SPLs are consistent with those from physical experimentation. The locations of the peaks for the simulation results are at 284, 387, and 480 Hz, respectively. The peaks for the physical experimentation results are 307, 388, and 479 Hz, respectively. The lowest natural frequency of the rectangular cavity was found to be near 285 Hz (see Sec. 3.2.2) which is also considered to be consistent with the results from ANSYS® simulations. The percent error appeared to be very small when considering the locations of the peaks and comparing the simulation results to those of the physical experimentation results.

To progress the analysis with the simulations and comparison with the physical experimentation results it is suggested that normalized data be studied as well. This technique is better suited for error quantification, enabling a more objective assessment of agreement between experimental and simulation results. Specifically,

1. Accounting for different scales: Experimental and simulation data could be recorded or calculated on different absolute scales due to variations in measurement techniques, equipment sensitivity, or simulation algorithms. Normalizing ensures that these differences in magnitude do not skew the comparison.
2. Focus on relative trends: Normalization allows for a focus on the relative patterns, behaviors, and trends in the data rather than absolute values since the goal is to validate the accuracy of the simulation in predicting overall system behavior.
3. Reduced systematic bias: Systematic differences, such as discrepancies in source strength, boundary conditions, or environmental factors, could have led to variations in absolute values. Normalization could mitigate these effects, making it easier to compare the underlying behaviours.
4. Comparing across conditions: Normalization enables comparisons across different experimental conditions or configurations. For example, the SPL during the physical experimentation vary significantly between different setups, normalizing them allows for consistent comparisons without being affected by setup-specific variations.

5. Improved visual comparisons: When visualizing data in graphs, normalized datasets can highlight deviations between the two data sets more effectively, making differences or similarities clearer.

Min-Max Normalization is used to scale the SPL values between 0 and 1. Figure 4.6 illustrates that the locations of the peaks are consistent between the ANSYS® and physical experimentation results at four peaks occurring beyond 300 Hz. Both show two peaks beyond 300 Hz. Below 300 Hz, while the number of peaks (one) is similar, the location of the peak differs by 7.5% between the ANSYS® and physical experimentation results. However, this peak is consistent with the overall remarks and conclusion made in Chapter 3 (see Sec. 3.3, concluding remark 1), identifying the lowest natural frequency of the system.

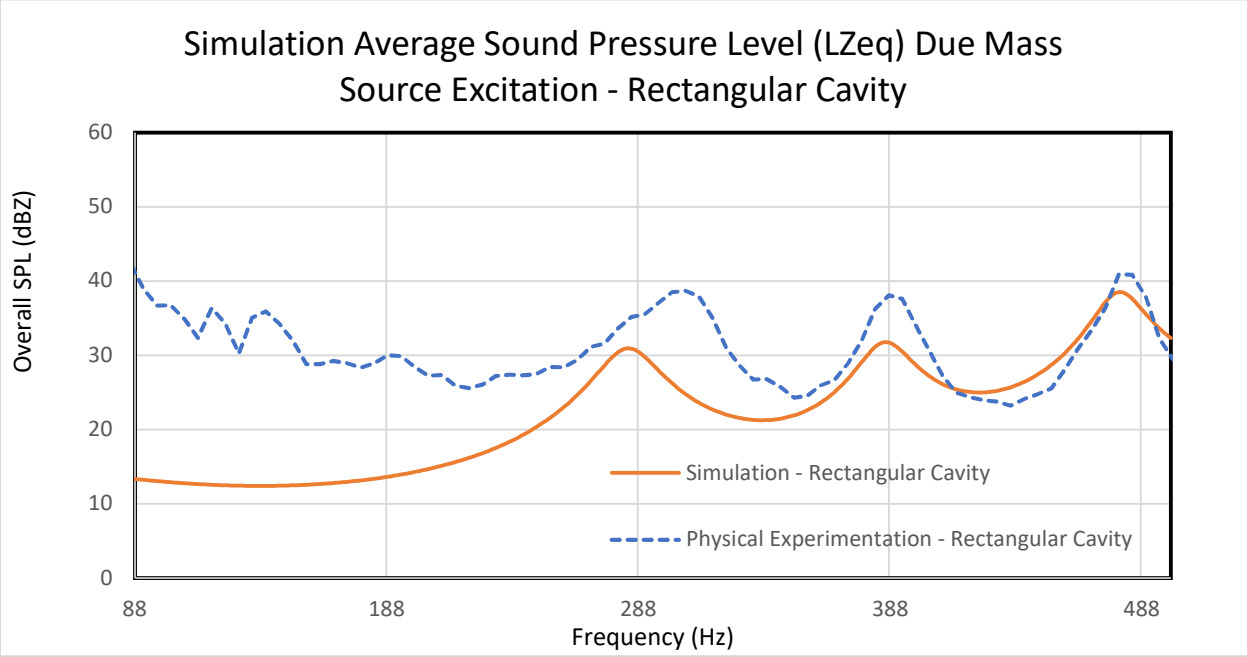

Figure 4.5. Simulated SPL results from mass source excitation at 0.19×10^{-6} kg/s and the measured spectrum from pink noise excitation (58 dB) within the rectangular cavity

The results outlined above are significant in identifying potential errors and quantifying the expected percentage of error in the subsequent simulations. This is crucial for advancing the research, as it ensures that various behaviors can be studied using a calibrated model. The ANSYS® simulations, verified against physical experimentation, provide a reliable foundation for further exploration and analysis.

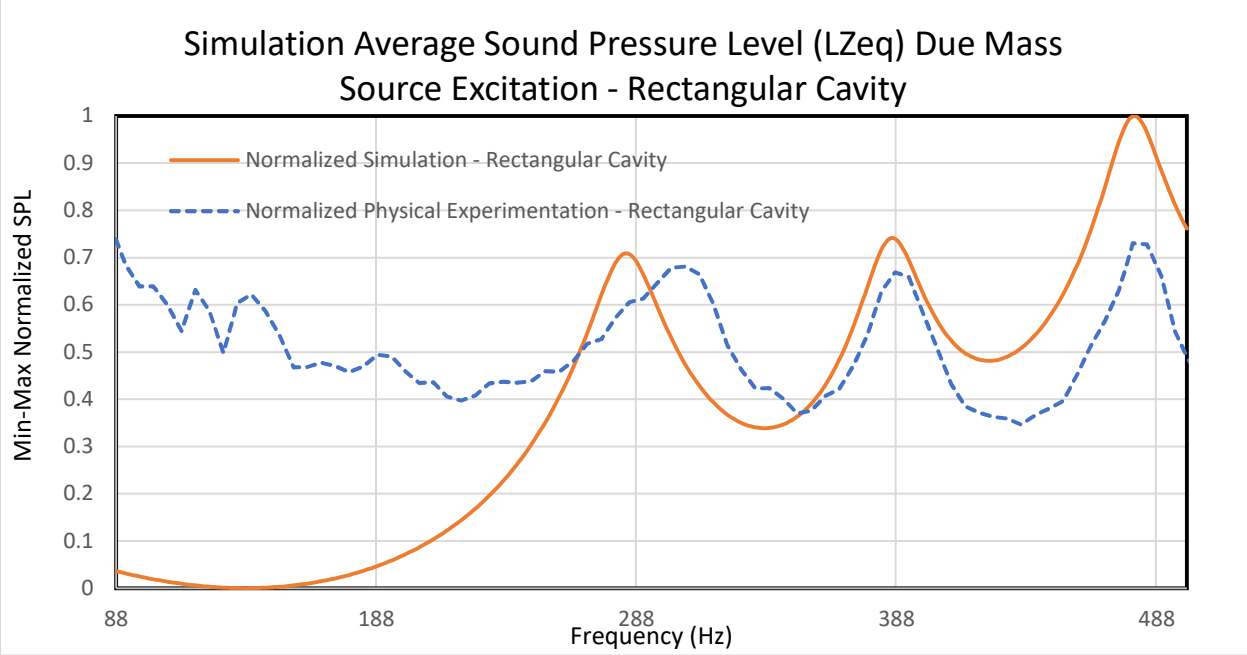

Figure 4.6. Simulated SPL results excitation within the rectangular cavity for the ANSYS® simulation and physical experimentation

4.2.2 ANSYS® Simulated Rectangular Cavity Subject to Excitations at Other Probing Points

Once the simulation results were calibrated and the errors identified by comparing the simulated results to those from physical experimentation, it becomes feasible to explore other locations within the system that were previously impractical to study using physical experimentation. This is due to the following reasons:

1. Preserving the integrity of the physical model: Measuring SPL within the physical system is an invasive process where penetrations are made which could accommodate the microphone capsule. Creating multiple penetrations in the physical model can compromise its structural integrity and alter its acoustic properties, leading to inaccuracies in measurements. Additionally, excessive perforations can introduce unintended absorption or reflection effects, which distort the results and reduce the validity of experimental data.
2. Reducing experimental error: Holes in the enclosure may allow airflow that affects the propagation of sound waves, leading to deviations from expected results. Holes can create sharp edges that scatter sound waves and introduce artifacts that do not present in the actual design.
3. Enabling high-resolution data collection: ANSYS® allows virtual probing at an unlimited number of points, including locations that may not be physically accessible in the real model.
4. Saving time and resources: Building a physical model with multiple measurement points requires significant effort and time, whereas simulations allow for testing different configurations and conditions rapidly. Avoiding physical modifications reduces the cost

of materials and labor associated with constructing and reconstructing experimental setups. The cost of instrumentation, such as high-precision microphones, can be substantial, particularly when capturing accurate acoustic data is essential. Additionally, data acquisition systems, calibration equipment, and signal processing tools further add to the overall cost. When experiments involve acoustic excitation using loudspeakers - sometimes generating sound levels of 100 dB - additional challenges arise. Efforts must be taken to ensure the testing environment remains safe and does not cause disturbance or annoyance to nearby personnel. This may result in operational delays, limited time windows for conducting experiments, and additional constraints on testing.

5. Enhancing physical model's safety: Excessive modifications to the model might lead to structural failure, especially for a brittle material such as glass under stress.

6. Efficient parameter variation and optimization: ANSYS® simulations allow for easy changes in parameters (e.g., material properties, geometry, etc.) without physically altering the model.

Two additional probing points are selected for further study under identical simulation conditions to Sec. 4.2.1, as shown in Figure 4.7. Note that the mid-point receptor is located at the middle of the top wall of the mesh.

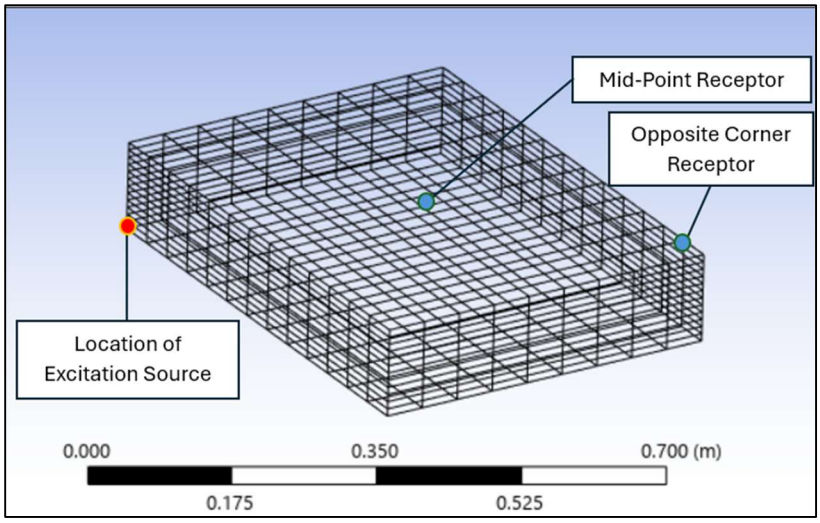

Figure 4.7. Additional probing points within the rectangular cavity's ANSYS® model

Figure 4.8 shows the simulation results associated with the average SPLs for the mid-point receptor. As can be seen from the simulated frequency response spectrum, the location of the peaks varies significantly from the previously presented results on Figure 4.6 where the receptor is at the corner adjacent to the excitation. The peak is shown to be at 390 Hz which is slightly shifted from comparison to the peak at 387 Hz for the adjacent corner receptor. The shift is less than 1%. However, there are no other peaks observed at the mid-point location. The SPL at 358 Hz approaches a minimum within the 100 to 500 Hz range. The SPL at 284, 387, and 480 Hz are 25, 14, and 22 dB, respectively, lower than at the adjacent corner (Figure 4.6).

Figure 4.9 shows the simulated average SPLs for the opposite-corner receptor. The simulation results indicate that there are peaks at 284, 389, and 479 Hz, respectively. While the results are like those of the previously presented adjacent corner receptor (Figure 4.6), the SPL drops to a minimum at 350 Hz which is 11 dB lower. The peak at 387 Hz for the adjacent corner

receptor is shifted by less than 1% for the oopposite corner receptor. The SPL at 284 Hz is slightly lower for the adjacent corner receptor, and higher for the peak at 479 Hz. However, the change in SPL is less than 0.5 dB and can be considered negligible.

The results at the additional probing points within the rectangular cavity are significant as they highlight the dependency of acoustic pressure peaks on location within the enclosure. The acoustic sound pressure within a small enclosure is not uniform. In fact, the probing points within the enclosure exhibit markedly different behaviors. Simulations reveal that the behavior of the acoustic sound pressure is influenced by the relative location of a receptor to the source of acoustic excitation (or mass source in ANSYS®). Additionally, it is observed that the pressure peaks predominantly occur at the corners of the enclosure, which aligns with observations from the physical experiments. The mid-point frequency response is markedly different, as the mid-point falls along the region where there is expected to be a node where the pressure variation is minimal [8].

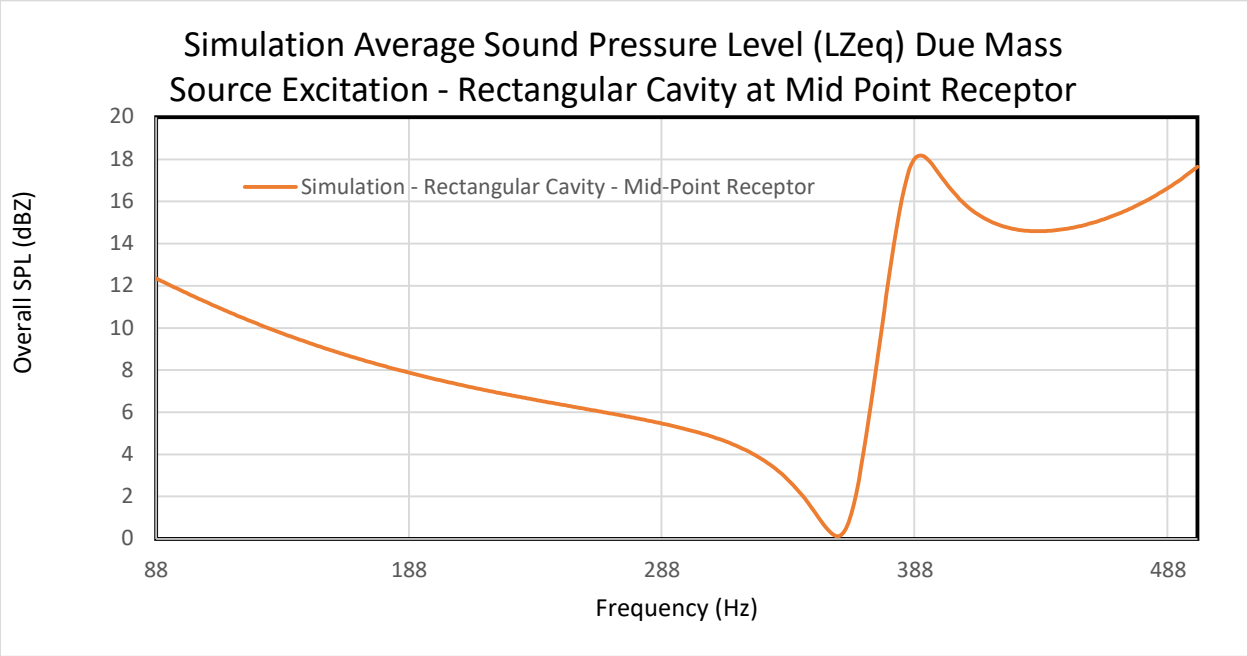

Figure 4.8. Simulated SPL results from mass source excitation at 0.19×10^{-6} kg/s for the mid-point receptor within the rectangular cavity

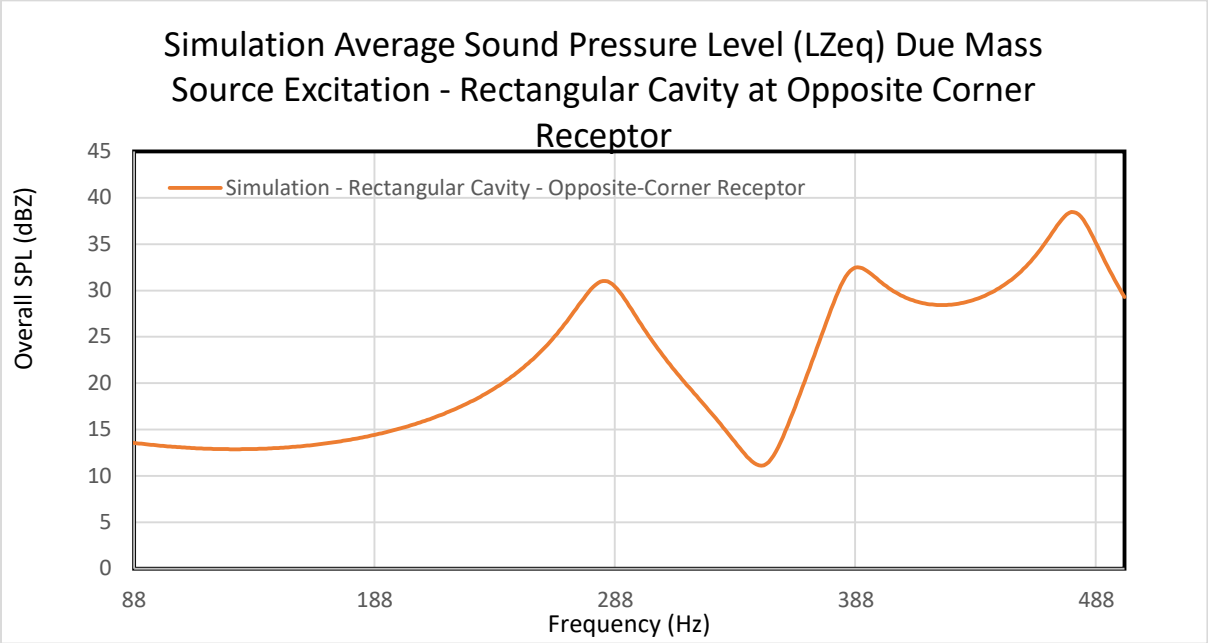

Figure 4.9. Simulated SPL results from mass source excitation at 0.19×10^{-6} kg/s for the opposite corner receptor within the rectangular cavity

4.2.3 ANSYS® Simulation of the Coupled System Subject to Excitations

Using similar methodology, a geometry for the coupled system was developed. The domain was subsequently discretized with 15753 elements (FLUID221, second order 3D elements TET10), and 27981 nodes, using a meshing method which would allow for more elements since the coupled system included additional spherical HR, as shown in Figure 4.10. The geometry was developed using the best approximation for the spherical HR that was utilized during physical experimentation. The approximation was based on its neck geometry and equivalent volume. Subsequently, the HR was positioned atop the rectangular cavity and gradually moved vertically down into the rectangular geometry until a slight interference was detected. This interference

was resolved, and the bodies were shared for seamless modeling. In other words, air is free to move between the rectangular cavity and HR. While this approach may introduce some discrepancies compared to the physical model, it enables progression through the analysis with a connected acoustic body. The SPLs of the adjacent receptor due to excitation from a mass source with identical properties and locations to those in Sec. 4.2.1 for rectangular cavity only were examined.

Figure 4.11 illustrates the results of the simulation results and compares it with the measured spectrum from pink noise excitation at 58 dB within the coupled system, previously presented in Figure 3.19. Figure 4.11 shows that there are peaks at 251, 367, and 448 Hz, respectively. On the other hand, the simulated spectrum of the coupled system shows a minimum SPL at 311 Hz. The physical experimentation results for the HR coupled with the rectangular cavity showed an increase in SPL at 269, 393, and 479 Hz, respectively (see Sec. 3.2.3). The SPL decreased at 285 and 307 Hz. Table 4.1 lists, for the coupled system, locations of peaks as they are computed as well as through physical experimentation. The percentage error is also included in Table 4.1. The lowest discrepancy is observed at 307 or 311 Hz where the SPL is decreased. The maximum error occurs at 296 Hz (or 251 Hz) where SPL sees an increase.

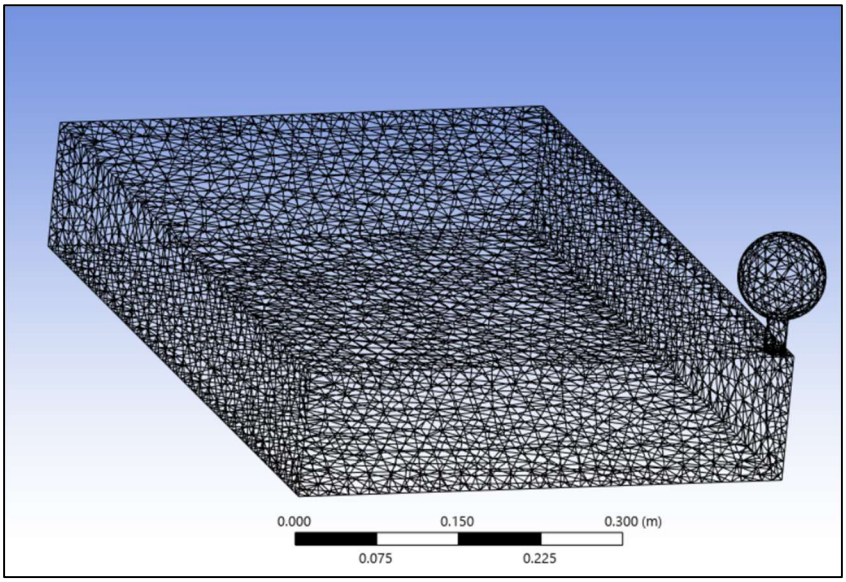

Figure 4.10. Coupled system as meshed in ANSYS®

Table 4.1. Comparison of locations of peaks for the coupled system

Physical experimentation	Simulation	% Error
269	251	6.7
393	367	6.6
479	448	6.5
285	311	9.1
307	311	1.3

Figure 4.12 shows the comparison of the simulated SPL results from mass source excitation for the coupled system and the rectangular cavity. Compared with the rectangular cavity, the maximum decrease in the SPL in the coupled system is 14 dB and occurs at 285 and 290 Hz, respectively. The coupled system's SPL decreases at 307, 387, and 480 Hz is approximately 10 dB, relative to the rectangular cavity's SPL. However, the SPL at 243 Hz increases by 4 dB, relative to that for the cavity.

The above simulation results indicate that the coupled system can attenuate noise at the target frequency of 307 Hz which is consistent with previously presented remarks regarding noise attenuation in the coupled system for the physical experimentation (see Sec. 3.3, concluding remarks 8 and 9). Unfortunately, the discrepancy increases with the addition of HR to the calibrated rectangular cavity system. This may be attributed to the following key elements such as:

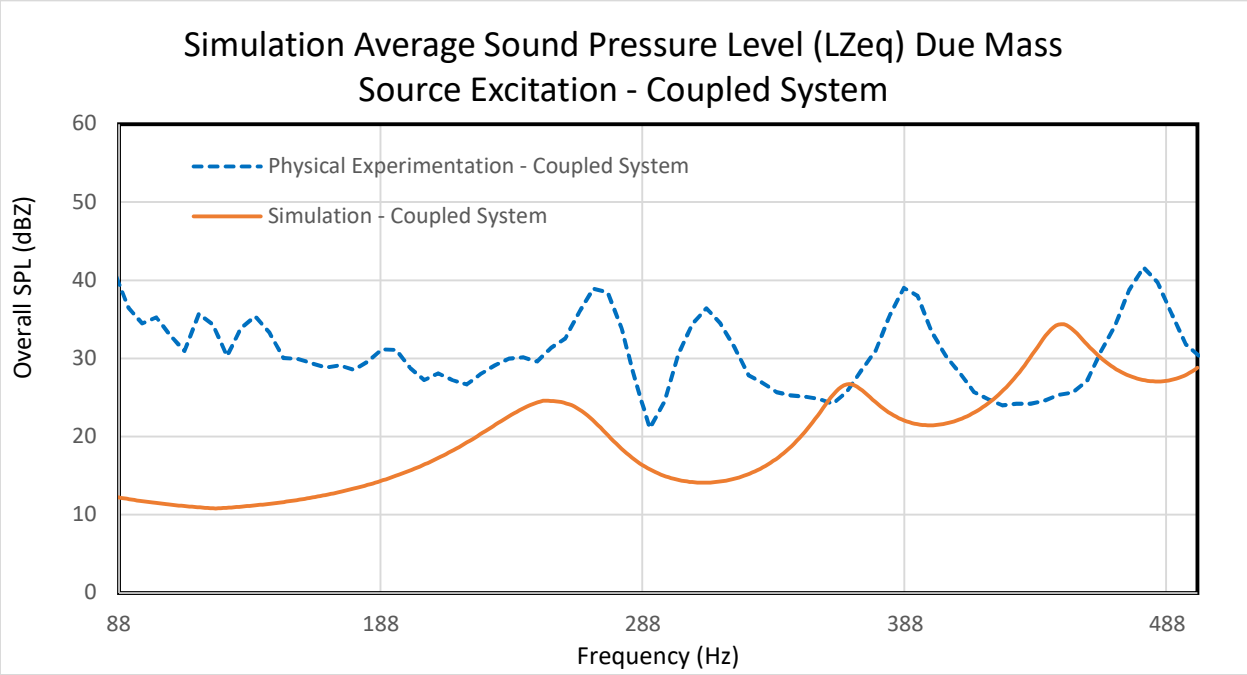

Figure 4.11. Simulated SPL results from mass source excitation at 0.19×10^{-6} kg/s and the measured spectrum from pink noise excitation (58 dB) within the coupled system

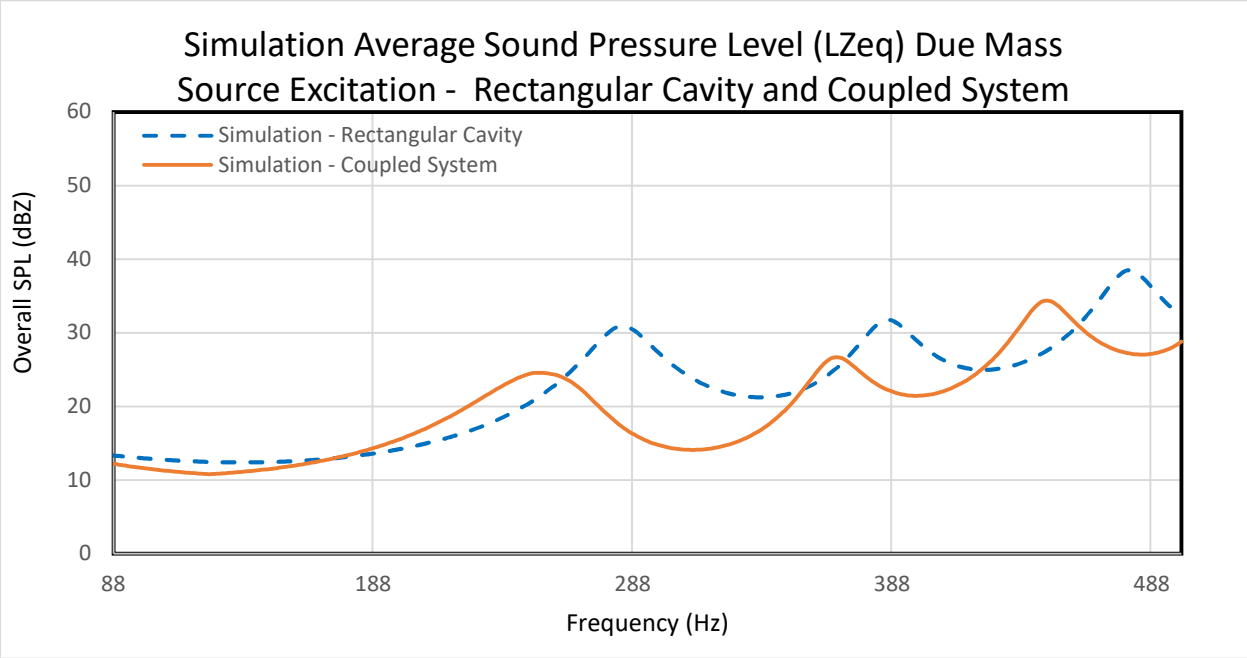

Figure 4.12. Simulated SPL results from mass source excitation at 0.19×10^{-6} kg/s within rectangular cavity and the coupled system

1. Increased geometric complexity: Adding the HR introduces a more complex geometry, which may lead to challenges in accurately meshing the system. Mesh quality, especially at the interface between the HR and the rectangular cavity, affects numerical accuracies and influences simulation outcomes.

2. Interaction between acoustic domains: The coupling between the rectangular cavity and the HR creates new acoustic interactions, such as impedance mismatches or resonant coupling, that are challenging to model accurately. These interactions may not have been fully captured by the calibration process.

3. Assumptions and approximations: The HR's geometry in the simulation was an approximation of the physical model based on neck geometry and equivalent volume.

This approximation may not perfectly replicate the actual physical behavior, leading to discrepancies between simulated and experimental results. Assumptions about boundary conditions, material properties, or air properties inside the HR could further introduce inaccuracies.

4. Boundary and interface effects: The interface between the HR and the rectangular cavity may introduce additional complexities, such as small gaps, imperfect connections, or mismatched acoustical impedance. These effects might be challenging to model and could amplify simulation errors.

5. Change in resonance behavior: The addition of the HR changes the overall resonant frequencies and acoustic modes of the system. Simulating these new modes accurately requires recalibration, and any deviations in the modeled acoustic response will contribute to the error.

6. Increased sensitivity to source and probing locations: The addition of the HR alters the sound field within the system, making the simulation more sensitive to the placement of the acoustic excitation source (e.g., mass source) and probing points. Small errors in these locations can lead to amplified discrepancies.

4.2.4 ANSYS® Simulation of the Coupled System Subject to Excitations at Other Probing Points within the HR

Two additional probing points (Figure 4.13) were also studied under identical simulation conditions to those mentioned in Sec. 4.2.3. Figure 4.14 demonstrates the simulated average SPL for the HR Neck Receptor. As can be seen in Figure 4.14, the peaks are located at 251, 367,

and 447 Hz. The maximum increase when compared to the simulated SPL within the rectangular cavity, at the adjacent corner receptor (Figure 4.12), is seen at 447 Hz by 7 dB. The maximum increase, compared to the simulation SPL at the adjacent corner receptor within the rectangular cavity, is 14 dB at 288 Hz within the HR at the HR Neck receptor. This increase at 307 Hz is 11 dB.

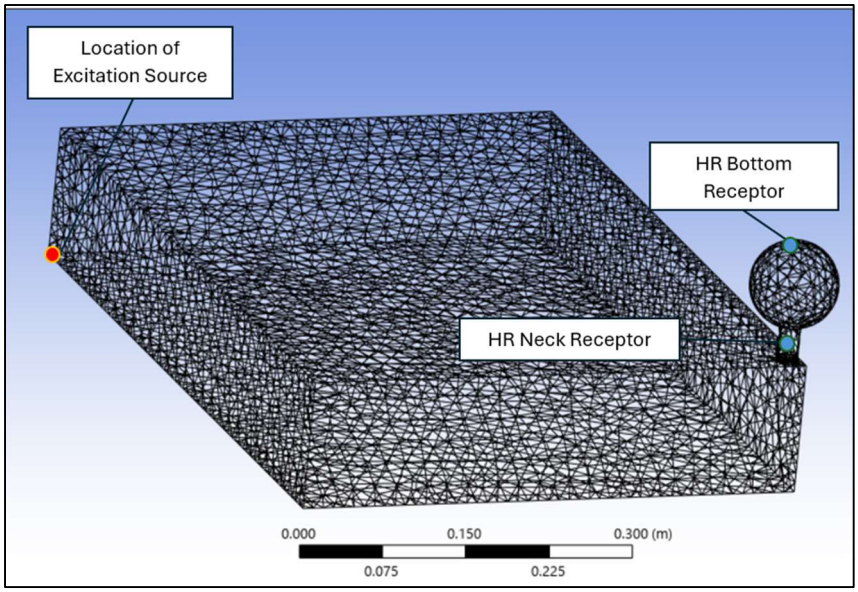

Figure 4.13. Additional probing points selected within the coupled system ANSYS® simulation model

Figure 4.15 presents the simulation results for the average SPL at the HR bottom receptor. The frequency response spectrum shows peaks at 259, 366, and 447 Hz, respectively. Notably, the maximum SPL increase compared to the rectangular cavity simulation (Figure 4.12) occurs at 250 Hz, with an increase of 15 dB. This receptor is particularly significant because it shows that the SPL at 307 Hz is 10 dB higher than that at the HR Neck Receptor.

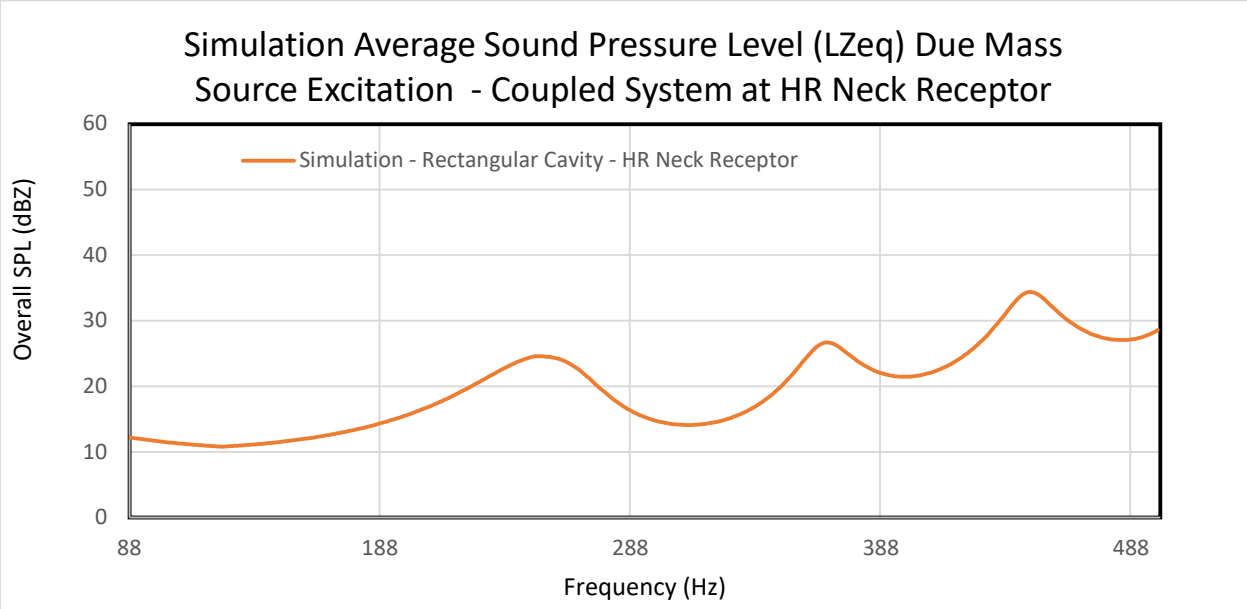

Figure 4.14. Simulated SPL results from mass source excitation at 0.19×10^{-6} kg/s for the HR neck receptor within the coupled system

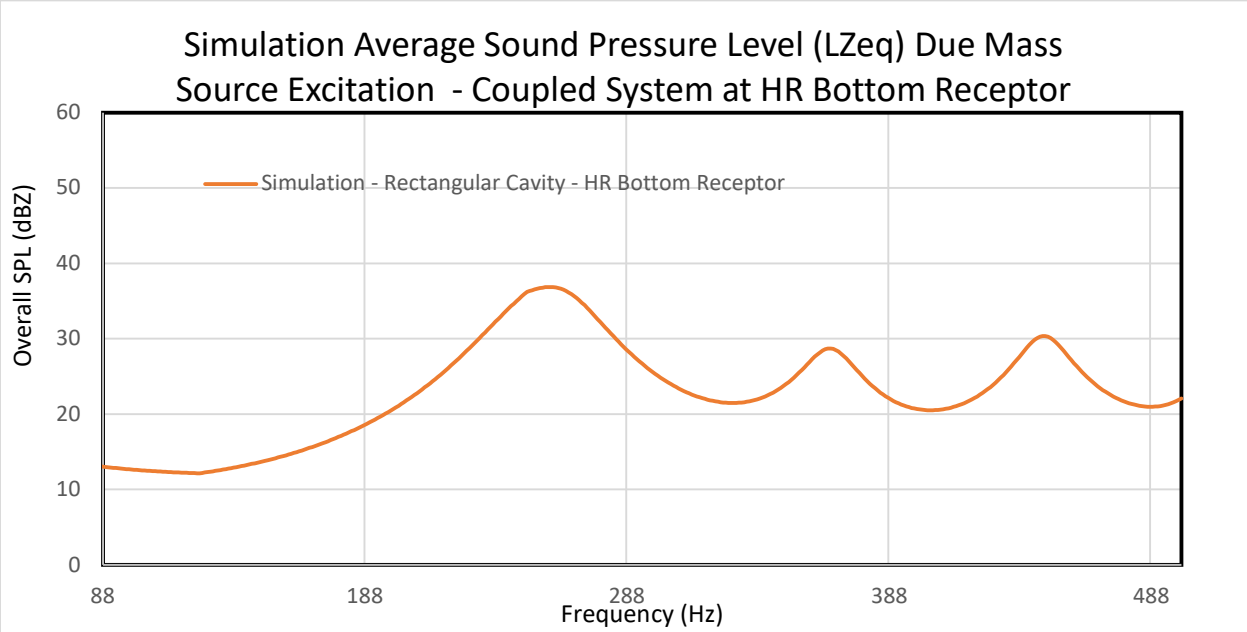

Figure 4.15. Simulated SPL results from mass source excitation at 0.19×10^{-6} kg/s for the HR neck receptor within the coupled system

While the HR's attenuation effect is independent of the specific location studied within the HR, the potential for energy harvesting is not. For instance, the higher SPL at the HR bottom receptor suggests a better opportunity for energy harvesting at 307 Hz, given the increased acoustic energy available. This finding enables exploration of optimal geometry and configuration and gain valuable insights into the acoustic behavior of different probing points within the HR and its coupling with the rectangular cavity.

4.3 Concluding Remarks

The main findings of the simulation work are,

1. The simulation results demonstrated strong agreement with the physical experimentation data, particularly in the identification of peak frequencies and overall

behavior of the rectangular cavity and coupled systems. The calibration process was instrumental in refining the accuracy of the ANSYS® model to match the physical experimentation, with a 7.5% discrepancy for the lowest natural frequency, which is deemed within acceptable margins for practical applications.

2. Proper meshing, particularly exceeding the minimum requirement of 18 elements per meter, ensured accurate frequency response predictions within the model. However, simplifications such as rigid-wall boundary conditions introduced limitations in capturing the fluid-structure interactions that could have contributed to some discrepancies between experimental and simulation results.

3. The simulation confirmed that the assumption of uniform sound pressure in small enclosures is incorrect. The results showed significant variations in SPL at different receptor locations within the rectangular cavity, with pressure peaks predominantly occurring at corners, aligning with physical observations.

4. The inclusion of the HR into the rectangular cavity system introduced increased geometric complexity and interactions between acoustic domains, which contributed to higher simulation error. Despite this, the HR addition proved effective for target frequency attenuation at 307 Hz, consistent with physical experimentation.

5. The study of SPL at different receptors within the HR revealed that the HR bottom receptor exhibited a higher SPL at 307 Hz compared to the HR neck receptor, indicating an opportunity for energy harvesting at this receptor location and at this frequency due to the increased acoustic energy available.

6. The ANSYS® simulations allowed for analysis of additional probing points, including those inaccessible in the physical model, without compromising the system's structural integrity. This facilitated a comprehensive exploration of acoustic behavior across the system and reduced the time and cost associated with physical modifications.
7. Errors in the coupled system simulations were attributed to factors such as increased geometric complexity, impedance mismatches, and approximations in HR geometry. While these errors were non-negligible, they did not significantly detract from the overall utility of the simulation as a tool for studying the system's behavior.
8. Normalizing the data was crucial for accurate comparison between experimental and simulation results, mitigating biases introduced by differing scales or measurement techniques. The normalized results further validated the consistency between the two approaches.
9. The calibrated model offers a reliable foundation for optimization and future studies, including energy harvesting applications and acoustic performance improvements. Further refinement of simulation techniques, such as incorporating fluid-structure interactions and higher-frequency analysis, could enhance the model's accuracy.

However, it is also worth mentioning that the discrepancies between the experimental results and results of numerical simulations were anticipated. These differences can be primarily attributed to the assumptions within the simulation model, including simplified boundary conditions, material property approximations, and the exclusion of structural details and environmental factors inherently present during physical testing.

Chapter 5 - Optimization of Energy Harvesting Potential

This chapter presents the simulation methodology and findings related to the energy harvesting potential of a stand-alone Helmholtz resonator (HR), a rectangular cavity, and a coupled system consisting of the HR and the rectangular cavity. The chapter is organized as follows: Sec. 5.1 outlines the limitation in using ANSYS® Student Version for optimization analysis; Sec. 5.1 is further subdivided into two sub-sections: Sec. 5.1.1 provides an overview of the specific limitation related to the availability of advanced optimization modules in ANSYS® Student Version; Sec. 5.1.2 details the exclusion of detailed piezoelectric harvester optimization analysis in ANSYS® Student Version. Sec. 5.2 provides an overview of the overall optimization methodology. Sec. 5.3 discusses experimental results and their associated analyses of the various parameter variation analysis using the ANSYS® software; Sec. 5.3 is subdivided into two sub-sections: Sec. 5.3.1 investigates the variation of sound pressure behavior within the spherical HR due to various interior finishes and its effect on energy harvesting potential; Sec. 5.3.2 explores and compares the variation of sound pressure behavior between using a spherical versus a cylindrical HR geometry. Sec. 5.4 provides concluding remarks for optimization of energy harvesting potential of the coupled system consisting of the HR and the rectangular cavity.

The primary objective of this chapter is to conduct a parameter variation analysis using the ANSYS® software to explore options for maximizing the energy-harvesting potential of the coupled system of HR and rectangular cavities. The analysis focuses on material selection, placement of the energy-harvesting piezoelectric beam, and geometric variations. Building

upon the calibrated base model investigated in Chapter 4 where simulation results demonstrate consistency with experimental data (within an upper limit for error of 9% for resonant frequencies), this chapter aims to expand upon the simulations to identify configurations that enhance energy harvesting capabilities within the HR in the coupled system.

While Chapter 4 examined in-depth the discrepancies between the simulation frequency response and experimental results, this chapter shifts focus to optimization strategies. Given the unavailability of the ANSYS® module for studying piezoelectric response, SPL results are used as a proxy to assess energy-harvesting potential. This provides a focused investigation into the acoustic coupling of the HR and rectangular cavity, where an increase in SPL within the HR correlates with greater vibrational energy available for harvesting, indirectly enhancing the piezoelectric performance without being constrained by having to physically experiment with various piezoelectric designs.

5.1 Optimization by the Means of ANSYS® Student Version

5.1.1 ANSYS® Student Version

ANSYS® Student Version provided valuable tools for simulations but lacks the advanced optimization capabilities needed for comprehensive parameter studies, which include ANSYS® DesignXplorer or ANSYS® OptiSLang that are integral to the professional version. Many advanced tools for optimization, such as Design of Experiments (DOE), response surface generation, and multi-objective optimization, are also absent in the Student Version. As a result, this research relies on manual parameter variation, a time-intensive and less efficient process. The advanced tools are crucial for exploring parameter interactions and identifying

optimal configurations in a systematic manner. Without these tools, the process of refining design parameters to achieve optimal results will not be automated.

The Student Version also lacks the capacity to perform comprehensive sensitivity analyses or explore complex parameter spaces efficiently. Sensitivity analysis involves systematically modifying design parameters, running simulations for each variation, and analyzing the results to identify trends and improvements. The approach adopted in this thesis, while providing some insights, is inherently less efficient and limited compared to automated optimization. Manual parameter variation involves an iterative trial-and-error process to explore the effects of design changes. Researchers must adjust one parameter at a time, observe the results, and make further adjustments based on the findings. This method is time-intensive and requires careful tracking of parameter combinations and outcomes. Manual studies demand significant time and effort from researchers to set up, run, and analyze multiple simulations. This labor-intensive process may increase the likelihood of errors and inconsistencies in data collection and interpretation. Due to time and resource constraints, only a narrow range of parameter values will be simulated. Results may not be optimal in the mathematical sense, as the full parameter space is not explored comprehensively.

Additionally, the ANSYS® Student Version imposes restrictions on the number of elements, nodes, and system size, limiting the complexity of models that can be analyzed. Therefore, focusing on the most influential parameters such as the increase in SPL could streamline the process and maximize the impact of limited optimization runs. For future studies, access to the full ANSYS® software suite is highly desired.

5.1.2 Exclusion of Piezoelectric Analysis

The decision to exclude detailed piezoelectric analysis from this study ensures a focused examination of acoustic interactions. Piezoelectric energy harvesters are highly sensitive to material properties, manufacturing tolerances, and environmental factors. Their performance depends on specific design parameters (such as beam dimensions, placement of beam, and polarization) which require a separate study to optimize. Including these variables would introduce additional complexities that are beyond the scope of optimizing energy harvesting potential attributed to acoustical behavior with the HR in the coupled system.

The decision to exclude detailed piezoelectric analysis is also due to the lack of access to the required ANSYS® module for piezoelectric analysis. By instead focusing on acoustical interactions and SPL optimization, this study provides insights that are broadly applicable to energy-harvesting systems and can serve as a foundation for future studies integrating piezoelectric materials.

SPL serves as an effective proxy for energy-harvesting potential, as higher SPL correlates with greater energy available for harvesting. Excluding piezoelectric-specific complexities allows the study to isolate and address key acoustic variables, such as HR geometry, material properties, and placement of beam, without being influenced by the intricacies of piezoelectric design. This decision ensures the research remains focused, manageable, and relevant to its primary objective. Future work can build on these findings to integrate piezoelectric-specific considerations and optimize the complete system.

5.2 Overview of Optimization Methodology

The optimization process aims to simulate multiple variants of the coupled system to understand their impact on the SPL relative to the base model. It employs base models consisting of a Helmholtz resonator (HR) positioned atop a corner of the rectangular cavity, like that shown in Figure 4.13. It also employs the simulation methodology described in Chapter 4, Sec. 4.1. In Chapter 4, by analyzing various probing points it was determined that the bottom receptor within the HR exhibited the highest potential for energy harvesting. This finding is now guiding the optimization methodology which will be a focused approach that prioritizes regions with the greatest energy-harvesting potential.

Optimization is inherently an iterative process, involving parameter variations to assess their overall effect on SPL. The optimization here will examine variations in HR geometry, interior finishes, and placement of piezoelectric beam within the system to identify configurations that maximize energy-harvesting potential.

Parameters will be analyzed through a trial-and-error approach: variations that result in increases in SPL are potential optimal solutions, while those that fail to enhance SPL inform the research of their limitations and what to avoid. The ultimate goal is to categorically identify configurations and design changes that will maximize SPL within the HR, thereby enhancing energy-harvesting potential. By systematically modifying design parameters, including HR geometry, material properties, placement of piezoelectric beam, and interior finishes, the optimization will lead to refinement of the system's performance. These findings could also provide a foundation for future studies focused on integrating piezoelectric energy harvesters or exploring additional acoustic and structural interactions. Moreover, this trial-and-error

approach enables practical insights into SPL enhancement even under the limitations of computer software (such as piezoelectric-specific modules or optimization solvers).

5.3 Optimization Results and Discussions

5.3.1 Coupled System with Various Surface Finishes and Subject to Excitations

5.3.1.1 Coupled System with Spherical HR and Concrete Finish

The setup is identical to that depicted in Figure 4.13, conducted under the same simulation conditions, except for a different surface finish. In Chapter 4, the HR was assumed glass finish. Here a concrete finish is simulated, by changing the material's absorption coefficient data to those for concrete [1]. It is noted that concrete is more sound-reflective than glass. Table 5.1 lists the absorption coefficients for glass, concrete and steel. Steel is the surface finish discussed in Sec. 5.3.1.2.

Table 5.1. Sound absorption coefficients

Material	Sound Absorption Coefficient		
	125 Hz	**250 Hz**	**500 Hz**
Glass	0.18	0.06	0.04
Concrete	0.01	0.02	0.04
Steel	0.05	0.10	0.10

Figure 5.1 shows the simulation results for the average SPL at the HR bottom receptor for the coupled system with a concrete finish. The frequency response spectrum reveals peaks at 237, 268, 366, and 447 Hz, respectively. Interestingly, near 237 and 268 Hz, the SPL spectrum shows double peaks or an M-shape.

As demonstrated in Figure 5.2, the SPL due to concrete finish sees an increase over the range of frequency under consideration, when compared with the SPL with glass finish. The maximum increase is observed near 237 and 268 Hz, where the concrete finish SPL curve shows double peaks or an M-shape. At 237 and 268 Hz, the concrete finish SPL increases by 13 and 10 dB, respectively, compared to the glass finish. These results are intuitive, as the concrete finish, being more reflective, contributes to higher SPL levels within the system. This means that concrete reflects more sound energy back into the air inside the HR rather than absorbing it, resulting in a higher SPL within the HR. The reflective nature of concrete helps traps sound waves within the system, reinforcing standing waves and resonant peaks, which contributes to an increase in SPL. The double peaks at 237 and 268 Hz observed with the concrete finish

suggest that the reflective surface enhances interactions between modes, possibly creating constructive interference that boosts SPL in those bands. Concrete's higher density and rigidity also is consistent with the assumption of rigid wall for the acoustical region. Glass, while reflective, can have a higher absorption coefficient in certain low-frequency bands due to its thinner nature and potential for minor flexural vibrations, which can dissipate energy. Therefore, concrete outperforms glass in increasing the SPL within the HR because of its highly reflective nature, and ability to enhance resonance and internal reflections. These characteristics make concrete effective material for systems requiring higher sound pressure levels, particularly in low-frequency ranges for energy harvesting.

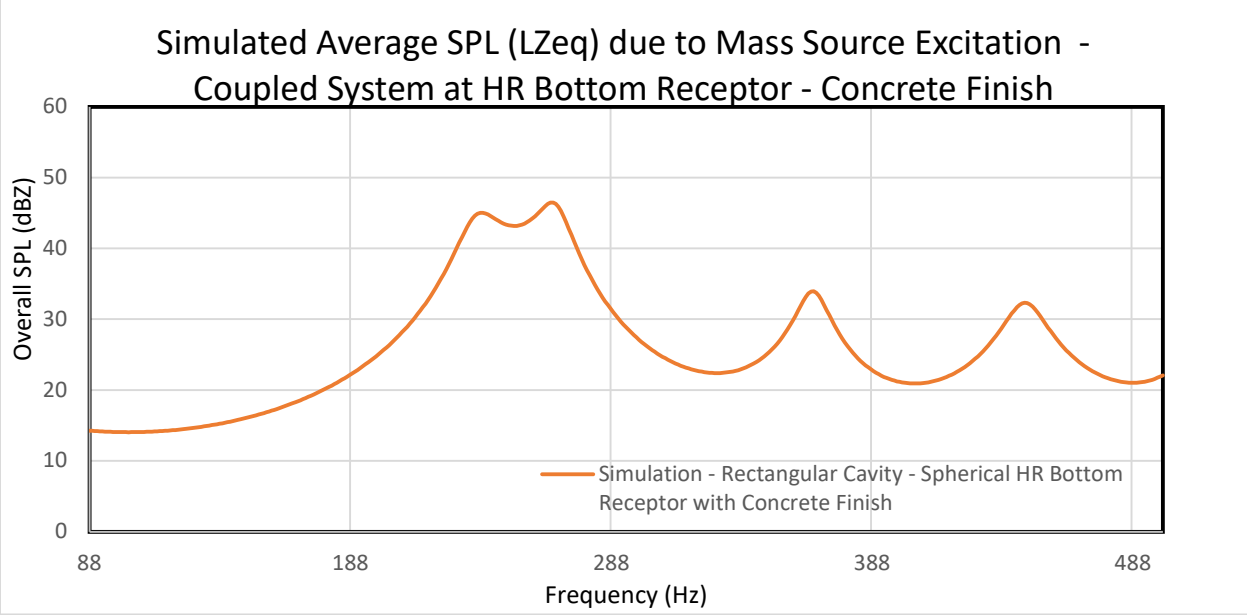

Figure 5.1. Simulated SPL results from mass source excitation at $0.19(10^{-6})$ kg/s for the HR bottom receptor within the coupled system with concrete finish

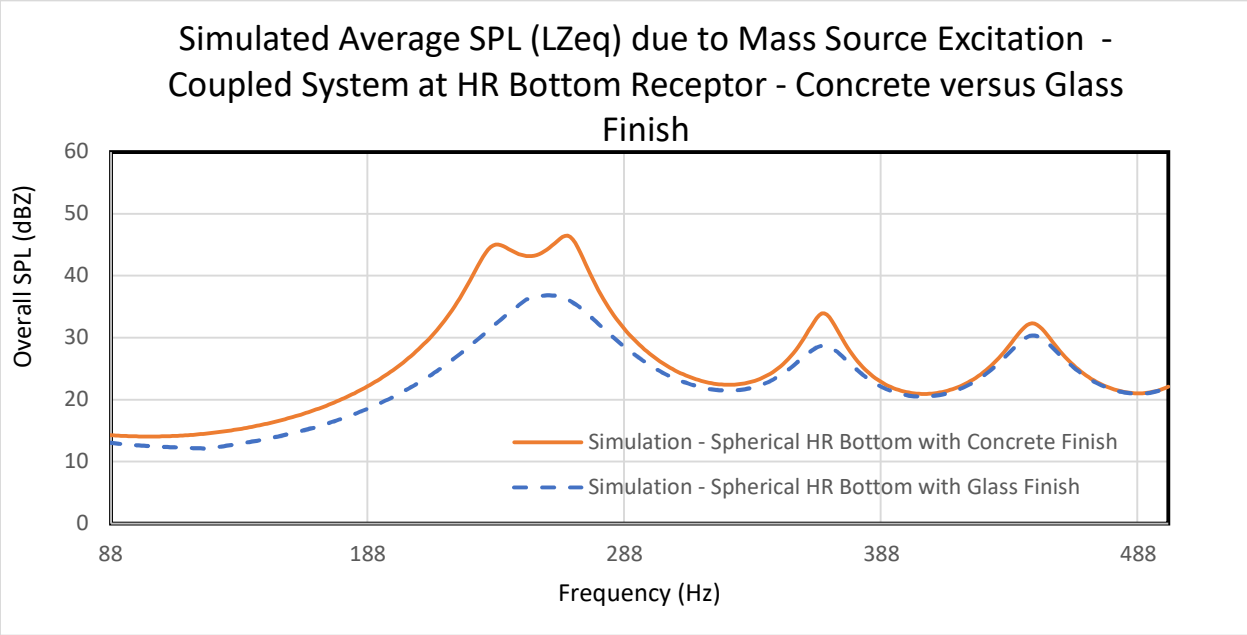

Figure 5.2. Simulated SPL results from mass source excitation at $0.19(10^{-6})$ kg/s for the HR bottom receptor within the coupled system for glass versus concrete finish

5.3.1.2 Coupled System with Spherical HR and Steel Finish

The setup is identical to the previous variant, except for utilizing a steel finish. It is important to highlight that concrete is less sound-reflective compared to glass. Figure 5.3 compares the simulation results for the average SPL at the HR bottom receptor for the coupled system with a steel and a glass finish. The frequency response spectrum indicates peaks at 237, 366, and 447 Hz, respectively. However, the SPL is higher for frequencies below 220 Hz with the steel finish when compared to the glass finish. Conversely, for frequencies above 220 Hz, the coupled system with glass finish sees increases in SPLs over those with steel finish.

When compared to the glass finish, the SPL for the steel finish is 3 dB lower at 237 Hz, 8 dB lower at 366 Hz, and 8 dB lower at 447 Hz. The lower SPL observed with the steel finish can

be attributed to the higher density and internal friction in steel, enabling it to absorb and dissipate vibrational energy more effectively.

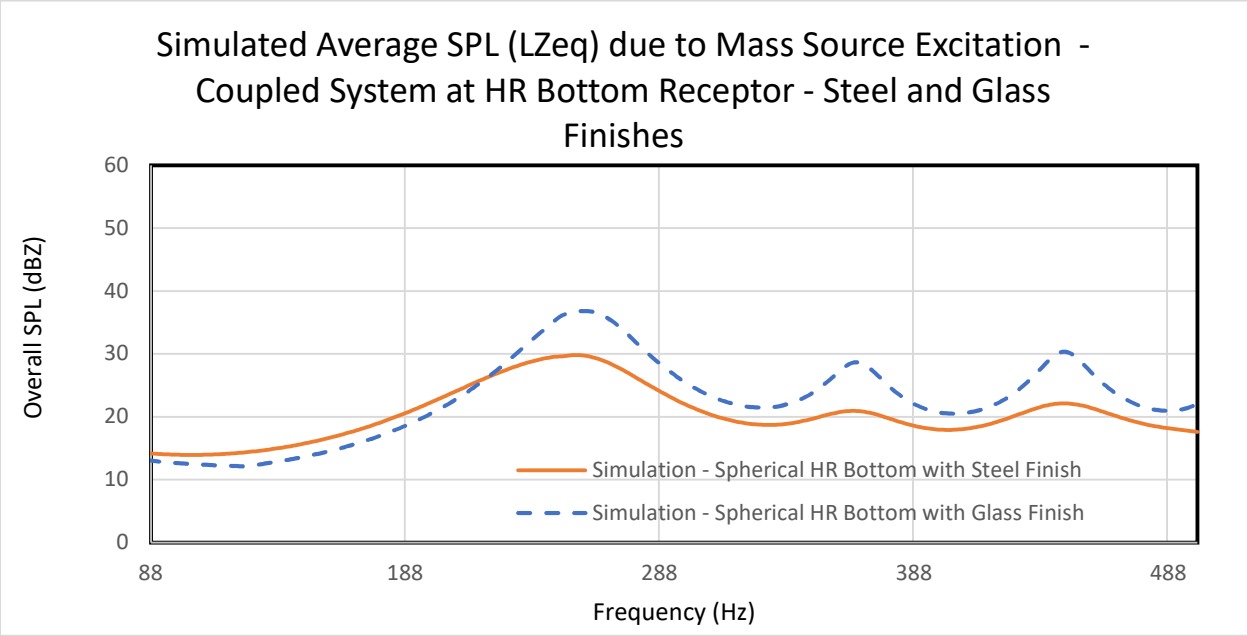

Figure 5.3. Simulated SPL results from mass source excitation at $0.19(10^{-6})$ kg/s for the HR bottom receptor within the coupled system, steel versus glass finishes

On the other hand, Figure 5.4 compares the simulated results of the average SPL at the HR Bottom Receptor for the coupled system with a steel, concrete, and a glass finish. The concrete shows to have the highest SPL increase compared to the other finishes and therefore would be considered the best option for increasing the potential for energy harvesting within the HR bottom region. The higher stiffness and damping of steel reduce the amplification of sound waves at the low frequencies under consideration compared to other finishes, which is least pronounced in concrete due to its relatively lower damping capacity. These combined factors may account for the variation of SPL in the systems with different interior finishes.

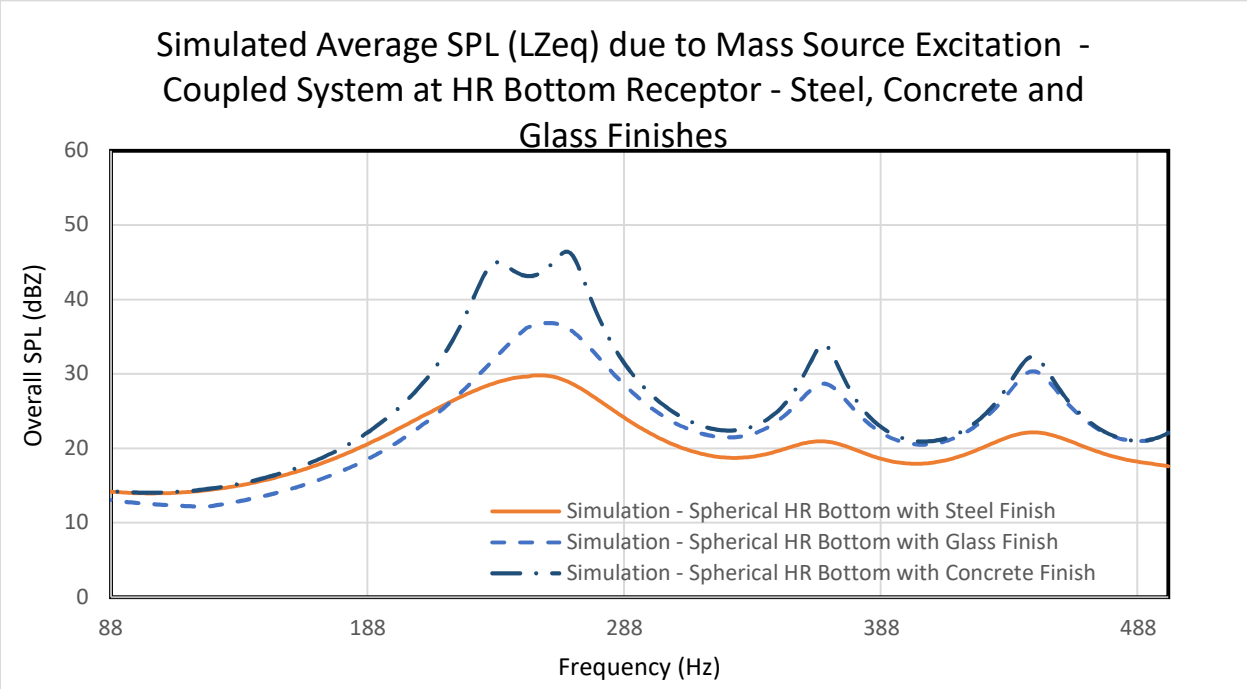

Figure 5.4. Simulated SPL results from mass source excitation at 0.19(10^{-6}) kg/s for the HR bottom receptor within the coupled system, steel, concrete and glass finishes

5.3.2 Coupled System with Cylindrical HR Geometry Subject to Excitations

5.3.2.1 Coupled System with Cylindrical HR and Glass Finish

The simulation setup is like the previously studied variant of glass finish and spherical HR (see Sec. 4.2.4). The difference here is the use of a cylindrical geometry for HR as shown in Figure 5.5. The neck geometry is the same as that of the spherical HR previously modeled and tested. Additionally, the cavity volume remains unchanged.

Figure 5.6 presents the simulation results for the average SPL at the cylindrical HR's bottom receptor for the coupled system with a glass finish. The results exhibit a trend like that

observed when a spherical HR was used with a glass finish. However, as shown in Figure 5.7, the spherical resonator slightly outperforms the cylindrical resonator in enhancing the SPL within the lower frequency range of 88 Hz to 278 Hz, with an average increase of 1 dB. Beyond 278 Hz, the cylindrical resonator demonstrates slightly better performance, increasing the SPL by approximately 0.5 dB over the spherical variant.

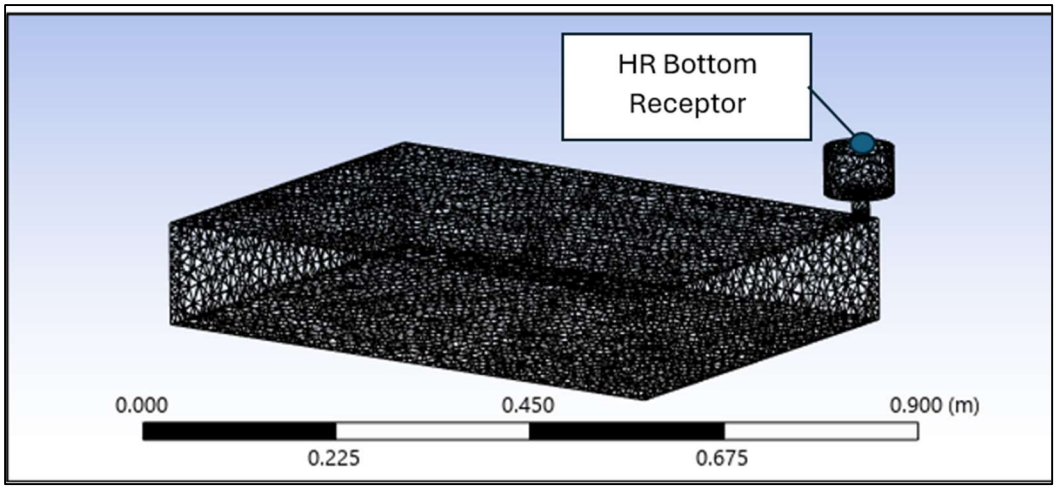

Figure 5.5. Probing point selected within the coupled system with ANSYS® simulation model for the cylindrical HR

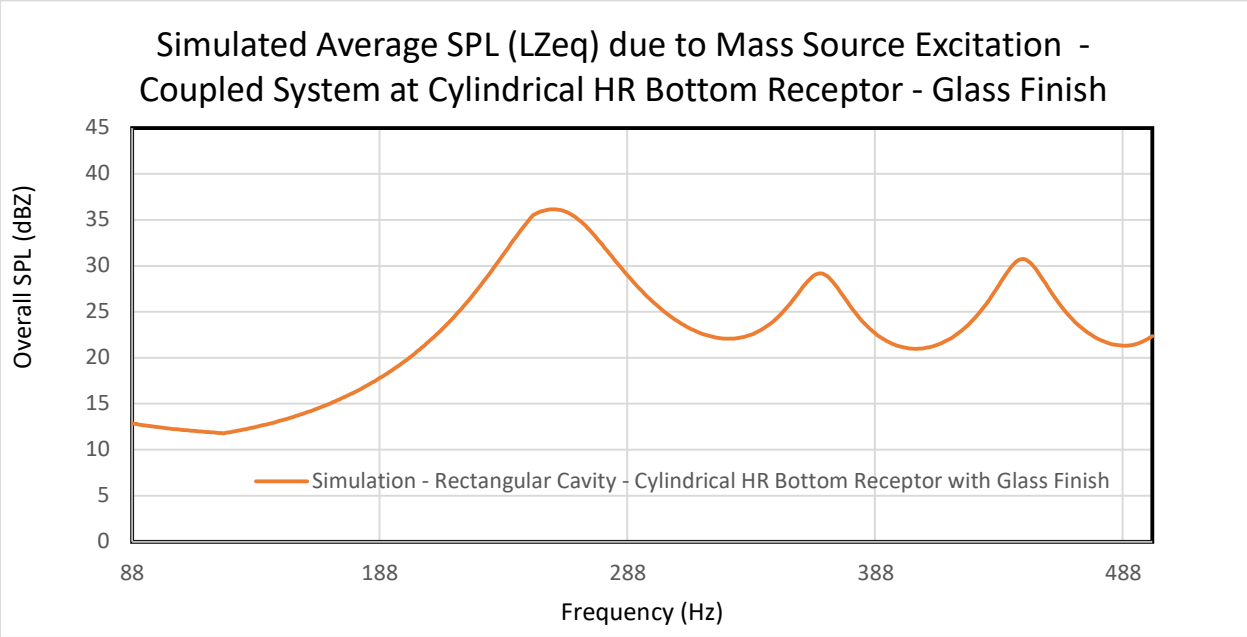

Figure 5.6. Simulated SPL results from mass source excitation at 0.19(10^{-6}) kg/s for the cylindrical HR bottom receptor within the coupled system for glass finish

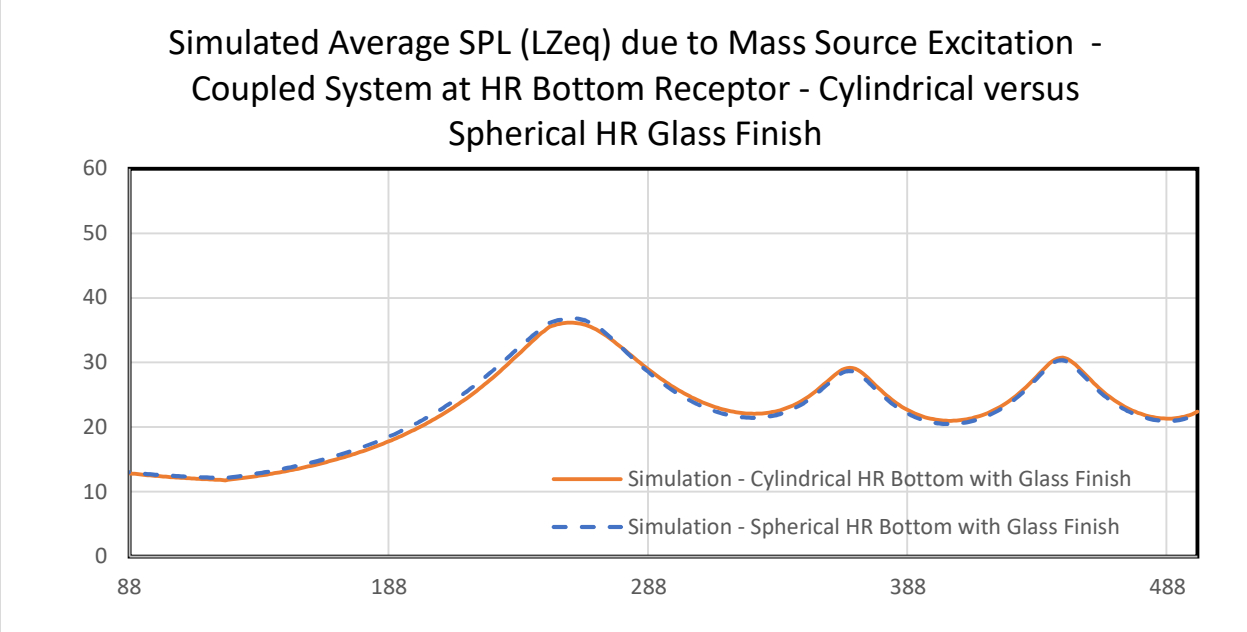

Figure 5.7. Simulated SPL results from mass source excitation at 0.19(10^{-6}) kg/s for the cylindrical HR bottom receptor within the coupled system versus the spherical HR with glass finish

5.3.2.2 Coupled System with Cylindrical HR and Concrete Finish

The setup is identical to the previous variant (Sec. 5.3.2.1) except for the use of a concrete finish instead of glass. Figure 5.8 presents the simulation results for the average SPL at the cylindrical HR's bottom receptor for the coupled system with a concrete finish. The figure also compares the SPLs at the bottom receptor of the spherical and cylindrical HRs, both of concrete finish. The cylindrical HR results exhibit a trend like that observed when the spherical HR was used. However, as can be seen from Figure 5.8, the frequencies which show a double-peak (or an M-shape) differ by 5 Hz. The spherical HR slightly outperforms the cylindrical counterpart in enhancing the SPL within the lower frequency range of 88 Hz to 278 Hz, with an average increase of 1 dB.

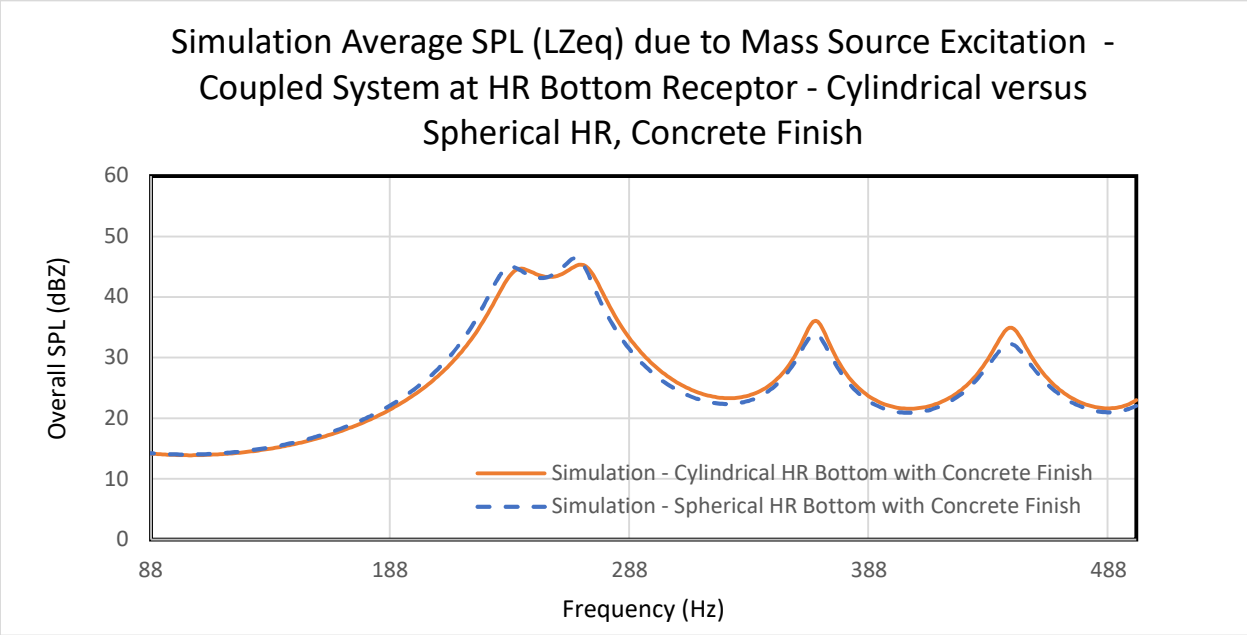

Figure 5.8. Simulated SPL results from mass source excitation at $0.19(10^{-6})$ kg/s for the cylindrical HR bottom receptor within the coupled system versus the spherical HR with concrete finish

5.4 Concluding Remarks for Optimization of Energy Harvesting Potential

This chapter examined the optimization of energy harvesting potential within the coupled system consisting of a Helmholtz resonator (HR) and a rectangular cavity, by the means of trial-and-error and using ANSYS® Student Version, regardless of the limitations of the Student Version. The study focused on optimization to enhance the SPL at the HR bottom receptor, which serves as a proxy for energy-harvesting potential. Key findings and inferences can be drawn as follows:

1. Variations in surface finishes and HR geometry directly influenced SPL trends, demonstrating the sensitivity of the system to design parameters.

2. Concrete Finish: The concrete finishes outperformed glass and steel in increasing the SPL within the HR. The highly reflective nature of concrete reinforced standing waves and resonant peaks, contributing to a significant SPL increase (13 dB and 10 dB at 237 and 268 Hz, respectively). Concrete is a common material in building construction. Concrete mix is readily available from venders such as Canadian Tire and Home Depot. Making HR with concrete finish is viable. Concrete is an optimal choice for enhancing SPL, particularly in low-frequency ranges.

3. Glass Finish: The glass finish demonstrated moderate reflectivity, with SPL levels sitting between those of steel finish and those of concrete finish. The small flexural vibrations may have absorbed a fraction of the acoustic energy, making it less efficient than concrete in boosting SPL.

4. Steel Finish: The steel finish showed the lowest SPL levels among the three finishes, particularly at frequencies greater than 278 Hz (3-8 dB lower than glass and concrete). The high density and damping properties of steel dissipated vibrational energy, reducing resonance effects and overall SPL.

5. Spherical HR: The spherical HR marginally outperformed the cylindrical HR in the lower frequency range (88 Hz to 278 Hz), with an average SPL increase of 1 dB. This advantage could be attributed to its geometry, which promotes a more uniform distribution of acoustic energy.

6. Cylindrical HR: The cylindrical HR demonstrated better performance in higher frequencies (above 278 Hz), increasing the SPL by approximately 0.5 dB compared to the

spherical variant. This suggests that the cylindrical geometry might be better suited for applications focusing on higher-frequency energy harvesting.

7. Across all configurations, the coupled HR and rectangular cavity system exhibited increased SPL compared to standalone components, underscoring the necessity of acoustic coupling in enhancing energy-harvesting potential.

Based on the presented results, the coupled system with a spherical HR and a concrete finish is the most effective configuration for maximizing SPL, especially in the critical low-frequency range where energy harvesting potential is highest. While cylindrical HR exhibited better performance at higher frequencies, the overall contribution of the spherical HR to SPL enhancement, combined with low sound absorption of concrete, makes this system the most promising for energy-harvesting applications.

These findings lay a strong foundation for future research, which would integrate piezoelectric analysis to further optimize energy harvesting while leveraging the acoustic advantages identified in this study.

Chapter 6 - Key Findings and Recommendations for Future Work

This chapter summarizes the experimental and simulation results, highlighting key observations and contributions of this study. The research examined the behavior of the Helmholtz Resonator (HR) and its interaction with a rectangular cavity, focusing on resonance characteristics, noise attenuation, and energy harvesting potential.

6.1 Key Findings

6.1.1 Experimental and ANSYS® Simulation Results

The HR exhibited strong resonance at 307 Hz, increasing the sound pressure level (SPL) by 17-19 dB, independent of excitation levels. This behavior, demonstrated in Figures 3.10 and 3.11, confirms the HR's effectiveness in amplifying specific frequencies. Figures 3.5 through 3.9 further support this trend, showing consistent SPL increases when the HR is exposed to acoustical excitation.

The rectangular cavity demonstrated modal resonance at 285 Hz, 307 Hz, and higher harmonics, amplifying the SPL levels in these frequencies. Figures 3.13 and 3.14 illustrate this effect under pink noise excitation, while Figures 3.15 and 3.16 confirm it under tonal excitation at 307 Hz.

When the rectangular cavity was combined with the HR, the coupled system exhibited an SPL reduction of approximately 5 dB at 307 Hz, as shown in Figures 3.18 and 3.19 under pink noise excitation and Figures 3.20 and 3.21 under tonal excitation. This reduction highlights the system's potential for noise control applications.

The HR alone harvested 327 mV AC, while the coupled system harvested 200 mV AC under the same conditions. Figures 3.24 and 3.25 document these results, showing that the HR optimized energy harvesting; the coupled system balanced attenuation and energy conversion. The ability of the coupled system to simultaneously reduce noise and harvest energy underscores its unique applications.

Simulated results closely aligned with the experimental data, with peak frequency deviations of 7-9%, validating the computational model. Figures 4.5 and 4.6, along with Table 4.1, illustrate this agreement, ascertaining the ANSYS® model as a tool for analyzing acoustic behavior.

Further simulations revealed SPL reductions of up to 14 dB, reinforcing the coupled system's potential for targeted noise control. Figures 4.11 and 4.12 detail these findings, forming a basis for future optimization.

Material and geometric variations also influenced the performance of the system. Concrete finishes resulted in the highest SPL enhancements, increasing SPLs by 13 dB and 10 dB at 237 Hz and 268 Hz, respectively. Steel finishes reduced SPL by 3-8 dB at higher frequencies. The spherical HR outperformed the cylindrical counterpart in the lower frequency range by approximately 1 dB SPL. Figures 5.1 through 5.8 present these results, highlighting the importance of material selection and geometry in acoustic optimization.

6.1.2 Limitations

Several limitations were identified in this study. The use of the ANSYS® Student Version restricted parameter variation and automated optimization, requiring manual adjustments. The

absence of advanced modules such as DesignXplorer prevented systematic optimization, and the lack of piezoelectric simulations within ANSYS® meant that voltage output had to be inferred from SPL rather than directly modeled. These constraints are discussed in Section 5.1.

Experimentally, the oscilloscope used in this study lacked sensitivity to detect voltage output at SPLs below 58 dB, limiting the ability to assess energy harvesting at lower sound levels. This limitation, as noted in Section 3.3, suggests the need for improved instrumentation in future research.

Additionally, approximations in the computational model may contribute to discrepancies between simulation and experimental results, particularly in the locations (in Hz) in the peak response spectra. These discrepancies are quantified in Table 4.1. While within reasonable margins to progress this research, improving on the model would enhance simulation accuracy.

6.2 Recommendations for Future Work

Acquiring a full ANSYS license would enable automated parametric optimization using tools such as DesignXplorer, streamlining design exploration. Implementing optimization algorithms could further optimize HR configurations.

Finite element modeling of piezoelectric response should be incorporated to allow direct voltage generation analysis, instead of having SPL as a proxy. Investigating alternative piezoelectric materials and placement strategies could improve energy harvesting efficiency and expand the range of practical applications.

Experimentally, conducting tests in a controlled laboratory setting would reduce external variables and improve result consistency. Upgrading to a more sensitive oscilloscope would enable energy harvesting measurements at lower SPLs, broadening the study's applicability to real-world conditions.

This study enhanced the understanding of the Helmholtz Resonator and rectangular cavity and demonstrated simultaneous noise attenuation and energy harvesting. By addressing identified limitations and incorporating advanced simulation and experimental methodologies, future research can refine and extend these findings, further optimizing acoustic system design and performance.

References

Chapter 1

[1] Volti R. Consuming Power: A Social History of American Energies. The Journal of American History. 1998;85(3):1050[1].

[2] AIP Publishing LLC. Small Scale Energy Harvesters Show Large-Scale Impact. Melville, NY: AIP Publishing LLC; 2017.

[3] Yang Z, Zhou S, Zu J, Inman D. High-Performance Piezoelectric Energy Harvesters and Their Applications. Joule. 2018;2(4):642-97[2].

[4] Covaci C, Gontean A. Piezoelectric Energy Harvesting Solutions: A Review. Sensors. 2020;20(12):3512.

[5] Sezer N, Koç M. A comprehensive review on the state-of-the-art of piezoelectric energy harvesting. Nano Energy. 2021;80:105567.

[6] Wakshume DG, Płaczek MŁ. Optimizing Piezoelectric Energy Harvesting from Mechanical Vibration for Electrical Efficiency: A Comprehensive Review. Electronics. 2024;13(5):987.

[7] Jaibhavani KS, Visalakshi S. Experimental study on the piezo-based energy harvester utilizing the ambient vibrations for smart applications. Automatika. 2024;65(3):1013-24.

[1] A single number indicates an article number.
[2] A range indicates page numbers.

[8] Zhou W, Du D, Cui Q, Lu C, Wang Y, He Q. Recent research progress in piezoelectric vibration energy harvesting technology. Energies. 2022;15(3):947.

[9] Li, Tao, Lee PS. Piezoelectric energy harvesting technology: from materials, structures, to applications. Small Structures. 2022;3(3):2100128.

[10] Yuan M, Cao Z, Luo J, Chou X. Recent developments of acoustic energy harvesting: A review. Micromachines. 2019;10(1):48.

[1] Ji G, Huber J. Recent progress in acoustic metamaterials and active piezoelectric acoustic metamaterials - A review. Applied Materials Today. 2022;26:101260.

[2] Kelle D, Demirkale Yilmaz S. Musicians' impressions of low frequency sound field in small music rooms. A|Z ITU Journal of the Faculty of Architecture. 2022;19(3):599-614.

[3] Araújo Alves J, Neto Paiva F, Torres Silva L, Remoaldo P. Low-frequency noise and its main effects on human health - A review of the literature between 2016 and 2019. Applied Sciences. 2020;10(15):5205.

[14] Crocker MJ, Arenas JP. Engineering Acoustics: Noise and Vibration Control. Hoboken, NJ: John Wiley & Sons Ltd, 2020. p. 308-309.

[15] Mahesh K, Ranjith SK, Mini RS. Recent Advancements in Helmholtz Resonator Based Low-Frequency Acoustic Absorbers: A Critical Review. Archives of Computational Methods in Engineering. 2024;31(4):2079-107.

[16] Peiffer A. Vibroacoustic Simulation: An Introduction to Statistical Energy Analysis and Hybrid Methods. Hoboken, NJ: John Wiley & Sons Ltd, 2022. p. 271-289.

[17] Haghighi M, Mirzaei R, Putra A, Taban E. A comprehensive review of advances and techniques in muffler acoustics and design. International Journal of Environmental Science and Technology. 2024. Available from: https://doi.org/10.1007/s13762-024-05686-6

[18] CM J, CP SK. General Design Principles of Reactive Mufflers: A Review. Proceedings of the International Conference on Systems, Energy and Environment 2022 (ICSEE 2022). Kerala, India, 2022. Available from: http://dx.doi.org/10.2139/ssrn.4296125

[19] Kumar A, Daniel S, Mishra J. A Review on Transmission Loss of the Silencer. Research Journal of Engineering Technology and Medical Sciences. 2023;6(1):157-62.

[20] Kumar KS, Kishore K, Sri PU. A Review on Enhancement of Developing Noise-less Suction Muffler for Reciprocating Compressor. International Journal of Mechanical Engineering. 2023;8:23-30.

[21] Huang L, Huang S, Shen C, Yves S, Pilipchuk AS, Ni X, Kim S, Chiang YK, Powell DA, Zhu J, Cheng Y, Li, Y, Sadreev AF, Alu A, Miroshnichenko AE. Acoustic resonances in non-Hermitian open systems. Nature Reviews Physics. 2024;6(1):11-27.

[22] Kaselouris E, Bakarezos M, Tatarakis M, Papadogiannis NA, Dimitriou V. A review of finite element studies in string musical instruments. Acoustics. 2022;4(1):183-202.

[23] Li Z, Zou H, Li J, Chen H. Research progress of cavity-based acoustic energy harvester. Journal of Vibroengineering. 2021;23(7):1680-93.

[24] Liao G, Luan C, Wang Z, Liu J, Yao X, Fu J. Acoustic metamaterials: A review of theories, structures, fabrication approaches, and applications. Advanced Materials Technologies. 2021;6(5):2000787.

[25] Wang H, Ma Y, Zheng Q, Cao K, Lu Y, Xie H. Review of recent development of MEMS speakers. Micromachines. 2021;12(10):1257.

[26] Zhao L, Zhou S. Compact acoustic rainbow trapping in a bioinspired spiral array of graded locally resonant metamaterials. Sensors. 2019;19(4):788.

[27] Bosia F, Dal Poggetto VF, Gliozzi AS, Greco G, Lott M, Miniaci M, Ongaro F, Onorato M, Seyyedizadeh SF, Tortello M, Pugno NM. Optimized structures for vibration attenuation and sound control in nature: A review. Matter. 2022;5(10):3311-40.

[28] Li J, Gea HC. Sound reduction of side-branch resonators: An energy-based theoretical perspective. AIP Advances. 2024;14(3):035248.

[29] Sandu C, Totu AG, Trifu AT, Deaconu M. Advances in Experimental Research on the Influence of Friction Powders on Acoustic Liners (Helmholtz Resonators). Aerospace. 2023;10(12):1000.

[30] Gautam A, Celik A, Azarpeyvand M. On the acoustic performance of double degree of freedom helmholtz resonator based acoustic liners. Applied Acoustics. 2022;191:108661.

[31] Guo J, Fang Y, Jiang Z, Zhang X. An investigation on noise attenuation by acoustic liner constructed by Helmholtz resonators with extended necks. The Journal of the Acoustical Society of America. 2021;149(1):70-81.

[32] Dannemann M, Kucher M, Kunze E, Modler N, Knobloch K, Enghardt L, Sarradj E, Hoschler K, Experimental Study of Advanced Helmholtz Resonator Liners with Increased Acoustic Performance by Utilising Material Damping Effects. Applied Sciences. 2018;8(10):1923.

[33] Li X, Peng Y, He Y, Zhang C, Zhang D, Liu Y. Research Progress on Sound Absorption of Electrospun Fibrous Composite Materials. Nanomaterials. 2022;12(7):1123.

[34] Yeang WY, Halim D, Yi X, Chen H. A compound microperforated panel backed by a panel-type resonator with a Helmholtz neck and multi-frequency resonators to improve bandwidth and low frequency sound absorption. Applied Acoustics. 2024;221:110030.

[35] Xie S, Wang D, Feng Z, Yang S. Sound absorption performance of microperforated honeycomb metasurface panels with a combination of multiple orifice diameters. Applied Acoustics. 2020;158:107046.

[36] Shao H, He J, Zhu J, Chen G, He H. Low-frequency sound absorption of a tunable multilayer composite structure. Journal of Vibration and Control. 2022;28(17-18):2279-87.

[37] Liu CR, Wu JH, Yang Z, Ma F. Ultra-broadband acoustic absorption of a thin microperforated panel metamaterial with multi-order resonance. Composite Structures. 2020;246:112366.

[38] Zhu Y, Assouar B. Multifunctional acoustic metasurface based on an array of Helmholtz resonators. Physical Review B. 2019;99:174109.

[39] Hedayati R, Lakshmanan SP. Active Acoustic Metamaterial Based on Helmholtz Resonators to Absorb Broadband Low-Frequency Noise. Materials. 2024;17(4):962.

[40] Peiró-Torres MP, Castiñeira-Ibáñez S, Redondo J, Sánchez-Pérez JV. Interferences in locally resonant sonic metamaterials formed from Helmholtz resonators. Applied Physics Letters. 2019;114:171901.

[41] Romero-Garcia V, Jimenez N, Theocharis G, Achilleos V, Merkel A, Richoux O, Tournat V, Groby J-P, Pagneux V. Design of acoustic metamaterials made of Helmholtz resonators for perfect absorption by using the complex frequency plane. Comptes Rendus Physique. 2021;21(7-8):713-49.

[42] Zhang L, Xin F. Perfect low-frequency sound absorption of rough neck embedded Helmholtz resonators. The Journal of the Acoustical Society of America. 2022;151(2):1191-9.

[43] Martins LR, Guimaraes GP, Fragassa C. Acoustical Performance of Helmholtz Resonators Used as Vehicular Silencers. FME Transactions. 2018;46(4):497-502.

[44] Crivoi A, Du L, Fan Z. Ventilated silencer based on layered Helmholtz resonators. Acoustical Society of America Proceedings of Meetings on Acoustics. 2024;52:022005.

[45] Gao C, Hu C, Hou B, Zhang X, Li S, Wen W. Ventilation duct silencer design for broad low-frequency sound absorption. Applied Acoustics. 2023;206:109324.

[46] Su YS, Chen YH, Feng QL, Shi WT. Optimal Design of Helmholtz Muffler for Air Compressor. Journal of Physics Conference Series. 2020;1605(1):012083.

[47] Cervenka M, Bednarik M. Optimized compact wideband reactive silencers with annular resonators. Journal of Sound and Vibration. 2020;484:115497.

[48] Shao HB, He H, Chen Y, Chen GP. A novel multi-cavity Helmholtz muffler. Chinese Physics B. 2019;28(5):54303.

[49] Bai C, Wu F, Wang J, Jiang J, Yang B. A broadband low-frequency muffler based on neural network method and Helmholtz resonator with helical neck. Journal of Vibration and Control. 2023;29(17-18):3942-51.

[50] Jatola R, Gupta AK. Enhancement of Low-Frequency Noise for Muffler by Optimizing the Space between Three 1-Degrees of Freedom Helmholtz Resonator. MATEC Web of Conferences. 2024;393:02007.

[51] Beck AB, Almeida G do N, Mikulski RZ, Vergara EF. Low-frequency acoustic attenuator based on a labyrinthine Helmholtz resonator. Journal of the Brazilian Society of Mechanical Sciences and Engineering. 2024;46(7):407.

[52] Gorazd Ł. Experimental Determination of a Reflective Muffler Scattering Matrix for Single-Mode Excitation. Archives of Acoustics. 2021;46(4):667-75.

[53] Dandsena J, Mohapatra K, Satapathy AK, Jena DP. Noise control of outdoor unit of split type air-conditioner using periodic scatterers made with array of Helmholtz resonators. Applied Acoustics. 2021;179:108054.

[54] Kanev N. Resonant Vessels in Russian Churches and Their Study in a Concert Hall. Acoustics. 2020;2(2):399-415.

[55] Moreira AM. Acoustic vases in the Portuguese synagogue of Tomar: Analogies with other coeval worship buildings. In: Mascarenhas-Mateus J, Pires, AP, editors. History of Construction Cultures Volume 2. Leiden, The Netherlands: CRC Press/Balkema, 2021. p. 240-246.

[56] Wang S, Tao J, Qiu X, Burnett IS. Broadband noise insulation of windows using coiled-up silencers consisting of coupled tubes. Scientific Reports. 2021;11(1):6292.

[57] Li DQ, Yang MZ, Lin TT, Zhong S, Yang P. Mitigation Effect of Helmholtz Resonator on the Micro-Pressure Wave Amplitude of a 600-km/h Maglev Train Tunnel. Applied Sciences. 2023;13(5):3124.

[58] Langfeldt F, Hoppen H, Gleine W. Broadband low-frequency sound transmission loss improvement of double walls with Helmholtz resonators. Journal of Sound and Vibration. 2020;476:115309.

[59] Kanev NG. Maximum Sound Absorption by a Helmholtz Resonator in a Room at Low Frequencies. Acoustical Physics. 2018;64(6):774-7.

[60] Pereira M., Carbajo J, Godinho L, Ramis J, Amado-Mendes P. Improving the sound absorption behaviour of porous concrete using embedded resonant structures. Journal of Building Engineering. 2021;35:102015.

[61] Kleinschmidt K. Cooperating with Miguel on improvements of the acoustical product - SOUNDBLOX. Acoustical Society of America Proceedings of Meetings on Acoustics. 2013;19:065033.

[62] Kim SK, Park WJ, Lee KH. Noise reduction capacity of a composite pavement system. KSCE Journal of Civil Engineering. 2014;18(6):1664-71.

[63] Zhou Y, Chen S, Fu H, Mohrmann S, Wang Z. Sound absorption performance of light-frame timber construction wall based on Helmholtz resonator. Bioresources. 2022;17(2):2652-66.

[64] Patil AT, Mandale MB. Recent acoustic energy harvesting methods and mechanisms: A review. Noise & Vibration Worldwide. 2021;52(11):397-410.

[65] Choi J, Jung I, Kang CY. A brief review of sound energy harvesting. Nano Energy. 2019;56:169-83.

[66] Ahmad MM, Khan FU. Review of vibration-based electromagnetic-piezoelectric hybrid energy harvesters. International Journal of Energy Research. 2021;45(4):5058-97.

[67] Smith GS. An experimental demonstration for a well-known example of Faraday's law of electromagnetic induction. European Journal of Physics. 2020;42(1):015203.

[68] Zhou S, Lallart M, Erturk A. Multistable vibration energy harvesters: Principle, progress, and perspectives. Journal of Sound and Vibration. 2022;528:116886.

[69] Rennie R, Law, J. editors. A Dictionary of Physics: Faraday's laws of electromagnetic induction. 8th ed. New York, NY: Oxford University Press; 2019.

[70] Joffe EB, Lock KS. Grounds for grounding: a handbook from circuits to systems. 2nd ed. Hoboken, NJ: John Wiley & Sons Ltd, 2023. p. 14-19.

[71] Gu C, Chen Y, Chen W, Zhao P. Acoustic Energy Harvester by Electromagnetic Mechanisms and Helmholtz Resonator. IOP Conference Series: Earth and Environmental Science. 2020;617(1):012038.

[72] Ahmad I, Hee LM, Abdelrhman AM, Imam SA, Leong MS. Development, characterization, and power management of electromagnetic-type hybrid vibro-acoustic energy harvester for wireless sensor nodes. Sensors and Actuators A: Physical. 2023;351:114154.

[73] Askari Farsangi MA, Zohoor H. A Tunable Helmholtz Resonator for Electromagnetic Energy Harvesting. 2018 6th RSI International Conference on Robotics and Mechatronics (IcRoM). Tehran, Iran, 2018. p. 322-5.

[74] Izhar, Khan FU. Three degree of freedom acoustic energy harvester using improved Helmholtz resonator. International Journal of Precision Engineering and Manufacturing. 2018;19(1):143-54.

[75] Kurdila AJ, Tarazaga PA. Vibrations of linear piezostructures. Hoboken, NJ: John Wiley & Sons Ltd, 2021. p. 1-11.

[76] Erturk A, Inman DJ. Piezoelectric energy harvesting. Chichester, West Sussex, UK: John Wiley & Sons Ltd, 2011. p. 9-10.

[77] Sekhar BC, Dhanalakshmi B, Rao BS, Ramesh S, Prasad KV, Rao PSVS, Rao BP. Piezo-electricity and its applications. In: Ranjan Sahu D, editor. Multifunctional Ferroelectric Materials. London, UK: IntechOpen Ltd, 2021. p. 1-3.

[78] Yan X, Li G, Wang Z, Yu Z, Wang K, Wu Y. Recent progress on piezoelectric materials for renewable energy conversion. Nano Energy. 2020;77:105180.

[79] Aguilar-Torres D, Jimenez-Ramirez O, Flores-Acoltzi O, Jimenez-Garcia JA, Luque-Zuniga G, Vazquez-Medina R. Environmental Noise Harvester Using a Helmholtz Resonator and Piezoelectric Transducer. International Journal of Acoustics and Vibration. 2022;27(3):301-14.

[80] Yuan TC, Chen F, Yang J, Song RG, Kong Y. A Novel Circular Plate Acoustic Energy Harvester for Urban Railway Noise. Shock and Vibration. 2021;2021:6647162.

[81] Cui X, Shi J, Liu X, Lai Y. A panel acoustic energy harvester based on the integration of acoustic metasurface and Helmholtz resonator. Applied Physics Letters. 2021;119(25):253903.

[82] Lai A. Design of an undamped Helmholtz resonator. M.Sc. thesis. Politecnico di Torino, 2024. Available from: http://webthesis.biblio.polito.it/id/eprint/30901 P. 57.

[83] Fan P, Wang S, Wang X. A high-performance conical-neck helmholtz resonator-based piezoelectric self-powered system for urban transportation. Applied Acoustics. 2024;220:109945.

[84] Mir F, Mandal D, Banerjee S. Metamaterials for Acoustic Noise Filtering and Energy Harvesting. Sensors. 2023;23(9):4227.

[85] Song C, Ma X, Zhao J, Zhang J, Yang F, Pan Y, Zhang, X. Broadband Sound Absorption and Energy Harvesting by a Graded Array of Helmholtz Resonators. IEEE Transactions on Dielectrics and Electrical Insulation. 2022;29(3):777-83.

[86] Mir F, Banerjee S. Performance of a Multifunctional Spiral Shaped Acoustic Metamaterial With Synchronized Low-Frequency Noise Filtering and Energy Harvesting Capability. ASME 2020 Conference on Smart Materials, Adaptive Structures and Intelligent Systems (SMASIS2020). Virtual, Online. 2020. Avilable from: https://doi.org/10.1115/SMASIS2020-2264

[87] Yuan M, Sheng X, Cao Z, Pang Z, Huang G. Joint acoustic energy harvesting and noise suppression using deep-subwavelength acoustic device. Smart Materials and Structures. 2020;29(3):035012.

[88] Zhang X, Zhang H, Chen Z, Wang G. Simultaneous realization of large sound insulation and efficient energy harvesting with acoustic metamaterial. Smart Materials and Structures. 2018;27(10):105018.

Chapter 2

[1] Crocker MJ, Arenas JP. Engineering Acoustics: Noise and Vibration Control. Hoboken, NJ: John Wiley & Sons Ltd, 2020. p. 52.

[2] Crocker MJ, Arenas JP. Engineering Acoustics: Noise and Vibration Control. Hoboken, NJ: John Wiley & Sons Ltd, 2020. p. 53.

[3] Raichel DR. The Science and Applications of Acoustics. 2nd edn. New York, NY: Springer, 2006. p. 147-148.

[4] Raichel DR. The Science and Applications of Acoustics. 2nd edn. New York, NY: Springer, 2006. p. 17.

[5] Crocker MJ, Arenas JP. Engineering Acoustics: Noise and Vibration Control. Hoboken, NJ: John Wiley & Sons Ltd, 2020. p. 24.

[6] Crocker MJ, Arenas JP. Engineering Acoustics: Noise and Vibration Control. Hoboken, NJ: John Wiley & Sons Ltd, 2020. p. 308.

[7] Pierce AD. Acoustics – An Introduction to Its Physical Principles and Applications. New York, NY: McGraw-Hill Inc., 1981. p. 18.

[8] Ver IL, Beranek LL. Noise and Vibration Control Engineering: Principles and Application. 2nd edn. New York, NY: Wiley Interscience, 2006. p. 150.

[9] Ver IL, Beranek LL. Noise and Vibration Control Engineering: Principles and Application. 2nd edn. New York, NY: Wiley Interscience, 2006. p. 152.

[10] Howard CQ, Cazzolato BS. Acoustic Analyses Using MATLAB® and ANSIS®. Boca Raton, FL: Taylor & Francis Group, 2015. p. 226.

[11] Reynolds DD. Engineering Principles of Acoustics – Noise and Vibration Control. Boston, MA: Allyn and Bacon, 1981. p. 387.

[12] Hambric SA, Sung SH, Nefske, DJ. Engineering Vibroacoustic Analysis – Methods and Applications. p. 55-57.

[13] Crocker MJ, Arenas JP. Engineering Acoustics: Noise and Vibration Control. Hoboken, NJ: John Wiley & Sons Ltd, 2020. p. 87-89.

[14] Pierce AD. Acoustics – An Introduction to Its Physical Principles and Applications. New York, NY: McGraw-Hill Inc., 1981. p. 320-321.

[15] Ver IL, Beranek LL. Noise and Vibration Control Engineering: Principles and Application. 2nd edn. New York, NY: Wiley Interscience, 2006. p.7.

[16] Ver IL, Beranek LL. Noise and Vibration Control Engineering: Principles and Application. 2nd edn. New York, NY: Wiley Interscience, 2006. p.9.

[17] Raichel DR. The Science and Applications of Acoustics. 2nd edn. New York, NY: Springer, 2006. p. 46.

[18] Barron RF. Industrial Noise Control and Acoustics. New York, NY: Marcel Dekker, 2003. p. 22.

[19] Barron RF. Industrial Noise Control and Acoustics. New York, NY: Marcel Dekker, 2003. p. 300.

[20] Barron RF. Industrial Noise Control and Acoustics. New York, NY: Marcel Dekker, 2003. p. 304.

[21] Crocker MJ, Arenas JP. Engineering Acoustics: Noise and Vibration Control. Hoboken, NJ: John Wiley & Sons Ltd, 2020. p. 92.

[22] Crocker MJ. Handbook of Acoustics. 1st edn. Hoboken, NJ: John Wiley & Sons, 1998. p. 144.

[23] Crocker MJ. Handbook of Acoustics. 1st edn. Hoboken, NJ: John Wiley & Sons, 1998. p. 153.

[24] Howard CQ, Cazzolato BS. Acoustic Analyses Using MATLAB® and ANSIS®. Boca Raton, FL: Taylor & Francis Group, 2015. p. 7.

[25] Howard CQ, Cazzolato BS. Acoustic Analyses Using MATLAB® and ANSIS®. Boca Raton, FL: Taylor & Francis Group, 2015. p. 13.

[26] Howard CQ, Cazzolato BS. Acoustic Analyses Using MATLAB® and ANSIS®. Boca Raton, FL: Taylor & Francis Group, 2015. p. 30.

[27] Crocker MJ. Handbook of Acoustics. 1st edn. Hoboken, NJ: John Wiley & Sons, 1998. p. 151.

[28] Howard CQ, Cazzolato BS. Acoustic Analyses Using MATLAB® and ANSIS®. Boca Raton, FL: Taylor & Francis Group, 2015. p. 31.

[29] Crocker MJ. Handbook of Acoustics. 1st edn. Hoboken, NJ: John Wiley & Sons, 1998. p. 155.

[30] Howard CQ, Cazzolato BS. Acoustic Analyses Using MATLAB® and ANSIS®. Boca Raton, FL: Taylor & Francis Group, 2015. p. 32.

Chapter 3

[1]. Crocker MJ, Arenas JP. Engineering Acoustics: Noise and Vibration Control. Hoboken, NJ: John Wiley & Sons Ltd, 2020. p. 308.

[2]. Crocker MJ, Arenas JP. Engineering Acoustics: Noise and Vibration Control. Hoboken, NJ: John Wiley & Sons Ltd, 2020. p. 52.

[3]. Crocker MJ, Arenas JP. Engineering Acoustics: Noise and Vibration Control. Hoboken, NJ: John Wiley & Sons Ltd, 2020. p. 317.

[4]. Howard CQ, Cazzolato BS. Acoustic Analyses Using MATLAB® and ANSIS®. Boca Raton, FL: Taylor & Francis Group, 2015. p. 226.

[5]. Hambric SA, Sung SH, Nefske, DJ. Engineering Vibroacoustic Analysis – Methods and Applications. p. 55-57.

[6]. Crocker MJ, Arenas JP. Engineering Acoustics: Noise and Vibration Control. Hoboken, NJ: John Wiley & Sons Ltd, 2020. p. 87-89.

[7]. Pierce AD. Acoustics – An Introduction to Its Physical Principles and Applications. New York, NY: McGraw-Hill Inc., 1981. p. 320-321.

Chapter 4

[1] Howard CQ, Cazzolato BS. Acoustic Analyses Using MATLAB® and ANSIS®. Boca Raton, FL: Taylor & Francis Group, 2015. p. 20.

[2] Woyak DB. Acoustics and Fluid-structure Interaction: A Revision 5.0 Tutorial. Swanson. Analysis Systems, Incorporated; 1992. p. 50.

[3] Crocker MJ, Arenas JP. Engineering Acoustics: Noise and Vibration Control. Hoboken, NJ: John Wiley & Sons Ltd, 2020. p. 53.

[4] Howard CQ, Cazzolato BS. Acoustic Analyses Using MATLAB® and ANSIS®. Boca Raton, FL: Taylor & Francis Group, 2015. p. 21.

[5] Howard CQ, Cazzolato BS. Acoustic Analyses Using MATLAB® and ANSIS®. Boca Raton, FL: Taylor & Francis Group, 2015. p. 48.

[6] Egan D. Architectural Acoustics. Fort Lauderdale, FL: J. Ross Publishing, 2007. p. 52.

[7] Egan D. Architectural Acoustics. Fort Lauderdale, FL: J. Ross Publishing, 2007. p. 66.

[8] Howard CQ, Cazzolato BS. Acoustic Analyses Using MATLAB® and ANSIS®. Boca Raton, FL: Taylor & Francis Group, 2015. p. 239.

Chapter 5

[1] Egan D. Architectural Acoustics. Fort Lauderdale, FL: J. Ross Publishing, 2007. p. 52.

Appendix

A mesh convergence study was conducted to determine the mesh size for simulations. The convergence criterion was based on the variation of the computed sound pressure level (SPL) at the target frequency of 307 Hz, and at a representative location referred to as the “Opposite Corner Receptor” as depicted in Figure 4.7, as the mesh was progressively refined.

The results are summarized in Table A.1, which shows the SPL values obtained for various mesh sizes ranging from 0.4 m to 0.05 m. As the mesh was refined, the SPL values stabilized, indicating convergence. The largest difference occurred between the coarsest mesh (0.4 m) and the next refinement (0.2 m), with a percentage change of approximately 1.69%. Further mesh refinement to 0.1, 0.07, and 0.055 m, respectively, yielded progressively smaller changes of 0.43%, 0.43%, and 0.00%, respectively. Mesh sizes of 0.07, 0.055 and 0.05 m, respectively, produced the same SPL value of 23.5 dB, confirming that mesh independence had been achieved.

These results demonstrate that a mesh size of 0.055 m or finer is sufficient for obtaining stable and accurate SPL values in the harmonic acoustics analysis of this system. The 0.05-m mesh size was selected as the baseline mesh size for all subsequent simulations to balance computational efficiency with numerical accuracy.

Table A.1. Mesh convergence study of SPL at 307 Hz in ANSYS® Harmonic Acoustics simulation for the base model

Mesh Size (m)	No. of Elements	Result (SPL at 307 HZ)	% Change from Previous Step
0.4	48	23.7	-
0.2	144	23.3	1.69
0.1	420	23.4	0.43
0.07	756	23.5	0.43
0.055	1188	23.5	0.0
0.05	1404	23.5	0.0